

**FORMATION, STRUCTURE, AND REPRODUCIBILITY OF
CERATO-ULMIN HYDROPHOBIN-COATED BUBBLES**

A Dissertation
Presented to
The Academic Faculty

By

Andrew Gorman

In Partial Fulfillment
of the Requirements for the Degree
Doctor of Philosophy in
Materials Science and Engineering

Georgia Institute of Technology

December 2019

COPYRIGHT © 2019 BY ANDREW GORMAN

FORMATION, STRUCTURE, AND REPRODUCIBILITY OF CERATO-ULMIN HYDROPHOBIN-COATED AIR BUBBLES

Approved by:

Dr. Paul S. Russo, Advisor
School of Materials Science and
Engineering
Georgia Institute of Technology

Dr. Hamid Garmestani
School of Materials Science and
Engineering
Georgia Institute of Technology

Dr. Karl I. Jacob
School of Materials Science and
Engineering
Georgia Institute of Technology

Dr. Jennifer Curtis
School of Physics
Georgia Institute of Technology

Dr. Meisha Shofner
School of Materials Science and
Engineering
Georgia Institute of Technology

Date Approved: September 27, 2019

ACKNOWLEDGEMENTS

I would like to thank my advisor, Dr. Paul Russo, for his support throughout my tenure in the Russo lab. His guidance and support have been instrumental to this work and it would not have been possible to complete this without his input. His lending of creative ideas as well as scientific input has prevented me from falling into many of the pitfalls that can bog down scientific research. I would also like to thank my committee members—Dr. Hamid Garmestani, Dr. Jennifer Curtis, Dr. Karl Jacob, and Dr. Meisha Shofner—for their feedback, advice, and time spent with me.

This work would not have been possible without the help of my colleagues in the Russo group, Georgia Tech staff, and beam line scientists at Oak Ridge National Laboratory and Stanford Synchrotron Radiation Light Source. I would especially like to thank Chris Tassone for his expertise on x-ray scattering and Nathan Maudlin on construction of experimental apparatus for the wave tank experiments.

I would also like to thank my friends and siblings for all their support and encouragement. Finally, I would like to thank my Mom and Dad for the constant encouragement and support to help me through this process by providing endless love and affirmation.

TABLE OF CONTENTS

Chapter 1.	Introduction.....	1
1.1	Hydrophobins	1
1.2	Biological role.....	2
1.3	Structure.....	5
1.4	Applications	13
1.4.1	Dispersants.....	14
1.4.2	Coatings	14
1.4.3	Foams and Emulsions	15
1.4.4	Biomedical	16
1.5	Cerato-ulmin	18
Chapter 2.	Examination of submicron structures in an aqueous agitated Cerato-ulmin Solution	21
2.1	Introduction	21
2.2	Dynamic Light Scattering.....	22
2.2.1	Cumulant Fitting.....	26
2.2.2	Multi-Exponential Fitting	28
2.2.3	Inverse Laplace Transforms	28
2.3	Effect of Time.....	30
2.3.1	Experimental Setup	30
2.3.2	Results	30
2.4	Static Pressure Effects.....	37
2.4.1	Experimental Setup	38
2.4.2	Results	38
2.5	Dynamic Pressure Effects	49
2.5.1	Experimental Setup	49
2.5.2	Results	50
2.6	Conclusions	63
Chapter 3.	Structural characteristics of cerato-ulmin in micro and submicron bubbles in an aqueous solution	64
3.1	Introduction	64
3.2	Optical Microscopy	65
3.2.1	Experimental Setup	65
3.3	Small-Angle Scattering	65
3.3.1	General Scattering	65

3.3.2	Small-angle Scattering Theory	66
3.3.3	Solution Scattering.....	70
3.3.4	Data Analysis	73
3.4	Small-angle Neutron Scattering	82
3.4.1	Neutron Production	82
3.4.2	Experimental Setup	84
3.5	Small-angle X-ray Scattering	84
3.5.1	X-ray Production	84
3.5.2	Experimental Setup	85
3.6	Atomic Force Microscopy.....	86
3.6.1	Basic Theory	86
3.6.2	Experimental Setup	87
3.7	Materials.....	88
3.7.1	Cerato-ulmin	88
3.8	Results and Discussion	89
3.8.1	Optical Microscopy	89
3.8.2	Small-angle Neutron Scattering.....	92
3.8.3	Small-Angle X-ray Scattering.....	98
3.8.4	Atomic Force Microscopy	114
3.9	Conclusions	118
Chapter 4.	Bubble creation through standardized agitation	120
4.1	Introduction	120
4.2	Bubble Formation.....	121
4.3	Wave Dynamics.....	123
4.4	Experimental Apparatus.....	132
4.4.1	Plunger-type Wave Tank	133
4.4.2	Acoustic Impulse Tank	137
4.4.3	Sloshing tank	138
4.5	Bubble Uniformity.....	144
4.6	Bubble Mechanics.....	149
4.7	Conclusions	153
Chapter 5.	Conclusions and Future work.....	154
5.1	Conclusions	154
5.2	Future Work.....	156
5.2.1	Effect of Time on CU Bubble Size	156
5.2.2	Submicron Bubble Size Gradient with Depth	157
5.2.3	Wave Tank Apparatus	157

5.2.4	Bubble Reptation through Optical Tweezing	158
5.2.5	Response Kinetics of Bubbles	163

LIST OF TABLES

Table 3.1. CU bubble thickness estimate from optical microscopy results	91
Table 3.2. Scattering length densities of components in the CU solutions.....	99
Table 3.3. Variables for the core-shell model form factor equation.	100
Table 4.1. Three versions of wave tank for paddle type wave tank.....	134

LIST OF FIGURES

Figure 1.1. Model of the biological role of hydrophobins during growth and development of filamentous fungi. Soluble hydrophobin is secreted at the tip of the growing, submerged hypha and diffuses into the aqueous environment (A). The water surface tension is lowered due to the assembly of hydrophobins into an amphipathic membrane at the medium-air interface (B), allowing the hypha to breach the medium-air interface and grow into the air. The hydrophobin protein molecules secreted by emerging aerial hyphae cannot diffuse into the environment and assemble at the cell wall-air interface (C). Aerial cavities in fruiting bodies are lined with an assembled hydrophobin layer preventing water from filling these cavities (D). Hydrophobins also play a role in the dispersal of spores by coating them with an amphipathic hydrophobin layer (E). Via assembly at the interface between the cell wall and a hydrophobic surface, hydrophobins mediate attachment to the surface, for example, during infection of host tissue (F). Take with permission from reference 26.	4
Figure 1.2. Chemical structure of the cysteine amino acid. The sulfur molecule and the resulting disulfide bonds in hydrophobins are crucial to their structure.....	5
Figure 1.3. Hydrophobins contain 8 cysteine residues with conserved spacing. These residues pair together to form disulfide bonds. Take with permission from reference 27.	6
Figure 1.4. Hydrophobins contain a mixture of α -helices and β -sheets beta sheet in their secondary structure. Every β -sheet is a mix of multiple β -strands that are connected laterally through hydrogen bonding. Take with permission from reference 34.	8
Figure 1.5. Topology and structure of HFBII. (A) topology of HFBII the <i>arrows</i> β -strands and the <i>rectangle</i> the α -helix. (B) three-dimensional structure of HFBII. The first β -hairpin is in <i>red</i> and the second in <i>purple</i> . The central β -barrel consists of two β -hairpins that interlock in the same way as the leather pieces of a baseball (C). Take with permission from reference 12.	9
Figure 1.6. The structure of HFBII in stereo showing β -barrel and four symmetrically arranged disulfide bridges in yellow. β -strands and Cys residues are labeled. Take with permission from reference 12.	9
Figure 1.7. Amino acid sequence comparison of class II hydrophobins. The secondary structure elements are given in the <i>first row</i> . The Cys residues are in <i>black</i> , and the residues found in the hydrophobic patch are in <i>red</i> . Protein identification related to the abbreviations used are: <i>HFBII</i> , <i>T. reesei</i> (accession P79073); <i>HFBI</i> , <i>T. reesei</i> (accession P52754); <i>SRHI</i> , <i>Trichoderma harzianum</i> (accession Y11841); <i>QID3</i> , <i>Trichoderma harzianum</i> (accession P52755); <i>TRII</i> , <i>TRI2</i> , and <i>TRI3</i> , the three segments of TH1 <i>Claviceps fusiformis</i> (accession Q9UVI4); <i>CPPHI_1</i> , <i>CPPHI_2</i> , <i>CPPH_3</i> , <i>CPPH_4</i> , and <i>CPPH_5</i> , the five segments of <i>cpph1 Claviceps purpurea</i> (accession AJ418045); <i>CRYPA</i> , Cryparin <i>Cryphonectria parasitica</i> (accession P52753); <i>CU</i> , Cerato-ulmin <i>Ophiostoma ulmi</i> (accession Q06153); <i>MAG</i> , Magnaporin <i>Magnaporthe grisea</i> (accession AF126872); <i>HCF5</i> , <i>Cladosporium fulvum</i> AJ133703; <i>HCF6</i> , <i>C. fulvum</i> (accession CAC27408). Take with permission from reference 12.....	10

Figure 1.8. Schematic representation of the 3D structure of class I (a, b) and class II (c) hydrophobins. Both types of hydrophobins contain a four stranded β -barrel core (a–c; in green) and either α -helical (b, c) or β -sheet (a) structure in loop 2 (L2). In class I hydrophobins (a, b), loops 1 and 3 (L1 and L3) are relatively large and are unstructured (a; EAS) or contain α -helical structure (b; DewA, RodA, and MPG1). Class II hydrophobins (c; HFBII, HFBII, and NC2) are relatively compact and have a small L1 and L3. Take with permission from reference 25.....	11
Figure 1.9. Assembly of class I and class II hydrophobins. Take with permission from reference 25.....	13
Figure 1.10. Hydrophobins encapsulating quantum dots for biomedical imaging.	17
Figure 1.11. Bright-field (A, B and E), dark-field (C) and negative-fluorescent (D) microscope images of toroidal microbubbles with wrinkles stabilized by CU. Take with permission from reference 90.	20
Figure 2.1. The speckle pattern from a DLS measurement is due to the constructive and destructive interference of light as the particles move.....	23
Figure 2.2. Dynamic light scattering setup. After the light is scattered from the sample it travels through a focusing lens, aperture and pinhole before reaching a detector.	23
Figure 2.3. The terminal velocity of a rising bubble in solution (red) and the velocity due to Brownian motion (black). Adapted from reference 105.....	33
Figure 2.4. Normalized, baseline-subtracted DLS correlation functions measured at a scattering angle of 90° for cerato-ulmin solution ($c = 0.07$ mg/mL) measured at different times after agitation.....	35
Figure 2.5. The apparent hydrodynamic radius of $c = 0.07$ mg/mL CU bubbles measured at 90° at different times with cumulant fitting. Inset are the normalized, baseline-subtracted DLS correlation functions at different times.	36
Figure 2.6. Cerato-ulmin bubbles created through gentle hand agitation of solution with a rocking motion (scale bar = 100 μ m). Taken with permission from reference 98.	39
Figure 2.7. Normalized, baseline-subtracted DLS correlation functions measured at a scattering angle of 90° for cerato-ulmin solution ($c = 0.1$ mg/mL) agitated by hand at different pressures. Decay rates are significantly decreased at higher pressures meaning the scatterers have a smaller hydrodynamic radius R_h . Inset: Semi-log plot of normalized, baseline-subtracted DLS correlation function.	40
Figure 2.8. Cumulant analysis of dynamic light scattering of $c=0.1$ mg/mL CU agitated by hand at various pressure.....	41
Figure 2.9. Dimensionless parameter $\mu 2\Gamma 2$ vs. angle for $c=0.1$ mg/mL CU bubbles at different pressures. $\mu 2\Gamma 2 \geq 0.3$ (red line) signifies a large distribution or multi-component system, above which cumulant analysis is not recommended as the sole method to determine size distribution.....	43
Figure 2.10. Multi-exponential analysis of dynamic light scattering of $c=0.1$ mg/mL CU agitated by hand at various pressures.....	45

Figure 2.11. Amplitude versus apparent radius for CONTIN analysis of dynamic light scattering of $c = 0.1$ mg/mL cerato-ulmin agitated by hand at various pressures.	46
Figure 2.12. CONTIN analysis of dynamic light scattering of $c=0.1$ mg/mL CU agitated by hand at various pressures.	47
Figure 2.13. Residual plots for cumulant, exponential, and CONTIN fits for $c = 0.1$ mg/mL CU solution at $\theta=60$ degrees with pressure at 1.3 bar.....	48
Figure 2.14. Radius versus pressure measurements with $c = 0.1$ mg/mL CU measured one hour after solution agitation. Each point is the zero-angle extrapolation from multiple DLS runs.	49
Figure 2.15. Measurement progression in dynamic pressure experiment. After each pressure change the sample equilibrated for 1 hour before measurements.	51
Figure 2.16. Normalized, baseline-subtracted DLS correlation functions in a semi-log plot measured at a scattering angle of 45° for cerato-ulmin solution ($c = 0.1$ mg/mL) at different pressures.	52
Figure 2.17. Normalized, baseline-subtracted DLS correlation functions measured at a scattering angle of 45° for cerato-ulmin solution ($c = 0.1$ mg/mL) during different points of the pressure cycle.....	52
Figure 2.18. Cumulant analysis for dynamic pressure experiment of $c = 0.1$ mg/mL CU agitated solution.	54
Figure 2.19. Zero-angle extrapolation of cumulant fitting for $c = 0.1$ mg/mL CU agitated solution during dynamic pressure cycle.....	55
Figure 2.20. Dimensionless parameter $\mu_2\Gamma^2$ vs. angle for $c = 0.1$ mg/mL CU bubbles at different points in the pressure cycle.	56
Figure 2.21. Zero-angle extrapolation of multi-exponential fitting for $c = 0.1$ mg/mL CU during dynamic pressure experiment.	57
Figure 2.22. Apparent hydrodynamic radius measurements using exponential fitting of the last two pressure steps in the dynamic pressure cycle for $c = 0.1$ mg/mL CU solution. The measurement at $P = 0.9$ bar gave higher values but the high-angle dependence results in $P = 1.0$ bar having a greater R_h when performing a zero-angle extrapolation.....	58
Figure 2.23. Multi-exponential fitting of cerato-ulmin bubbles shows a decrease in hydrodynamic radius as increased pressure is applied followed by an increase in radius as the pressure decreases and a partial vacuum is formed. The error bars are uncertainty in the fit, not a standard deviation of the measurement. Take with permission from reference 98.	59
Figure 2.24. CONTIN analysis of $c = 0.1$ mg/mL CU at 45 degrees during a dynamic pressure cycle. The error bars are the standard deviation of the continuum of bubbles in solution.....	60
Figure 2.25. Dynamic pressure experiment results using CONTIN, multi-exponential, and cumulant fitting of $c = 0.1$ mg/mL CU measured at 45°	62

Figure 3.1. Schematic of the scattering of a single particle. Adapted from reference 120.	67
Figure 3.2. The power law for various mass and surface fractals in the Porod region. Intensity decreases according to the sample morphology and the length scale being probed. The size of the red circle represents the characteristic length d where $q=2\pi/d$. Take with permission from reference 124.	72
Figure 3.3. The relationships between the electron density difference $\rho(r)$, amplitude $A(s)$, pair-distance distribution function $p(r)$, and intensity $I(s)$ is commonly presented as the magic square of scattering. Adapted from reference 130.	74
Figure 3.4. SAXS intensity (top) is converted to a PDDF (bottom) through an inverse Fourier transform. Taken with permission from reference 131.	76
Figure 3.5. DAMMIF model for <i>meso</i> -tetra(4-sulfonatophenyl)-porphyrin (H_2TPPS^4) from synchrotron beamline. Take with permission from reference 121.	77
Figure 3.6. The connectivity parameter in the DAMMIF program describes the compactness of a system.	80
Figure 3.7. Schematic of spallation neutron source. In this schematic, negative ions are accelerated down the 70 MeV linear particle accelerator (LINAC). At the end of the accelerator a foil strips off the electrons. The resulting protons travel around the synchrotron before being tightly focused and sent to the target. Adapted from reference 134.	83
Figure 3.8. In tapping mode AFM measures the changes in the laser deflection as the probe oscillates and interacts with the sample.	87
Figure 3.9. MALDI of cerato-ulmin shows a molecular weight of $7626 \text{ g}\cdot\text{mol}^{-1}$ which is expected from the 73 amino acid protein. Take with permission from reference 90.	89
Figure 3.10. CU forms cylindrical bubbles when a solution is agitated in a VitroCom glass cell (scale bar 100 μm).	90
Figure 3.11. Small-angle neutron scattering envelope of cerato-ulmin bubble dispersion. Bubbles were created by agitating a 2 mg/mL solution.	94
Figure 3.12. The pair distance distribution function of the CU protein measured at the EQ-SANS beamline.	95
Figure 3.13. DAMMIF models calculated from the pair distance distribution function of SANS data. Sample was an agitated $c = 2 \text{ mg/mL}$ cerato-ulmin solution of bubbles exposed to the beam for 6 hours. The magnification is not equal on each individual image.	96
Figure 3.14. DAMAVER model of CU suggests the protein exists in an elongated structure in the bubble film	97
Figure 3.15. Spherical core-shell fits with 16 nm thickness and varying radii: (A) 50 nm; (B) 100 nm; (C) 200 nm; (D) 400 nm.	101
Figure 3.16. The effect of standard deviation of the radius in a 200 nm bubble with 16 nm thickness: (A) No standard deviation; (B) $\pm 2 \text{ nm}$; (C) $\pm 10 \text{ nm}$; (D) $\pm 20 \text{ nm}$	102

Figure 3.17. Spherical core-shell models with a 200 nm radius but different thicknesses: (A) 4 nm; (B) 8 nm; (C) 12 nm; (D) 16 nm.	103
Figure 3.18. Schematic of a cylindrical core-shell model with accompanying variables.	104
Figure 3.19. Cylindrical core-shell models with a 20 nm radius, 16 nm thickness, and various lengths: (A) 50 nm; (B) 100 nm; (C) 200 nm; (D) 400 nm.	106
Figure 3.20. Cylindrical core-shell models with a 20 nm radius, 400 nm length, and various thicknesses: (A) 4 nm; (B) 8 nm; (C) 12 nm; (D) 16 nm.	107
Figure 3.21. SAXS pattern of $c = 2$ mg/mL cerato ulmin bubble dispersion. Uncertainties are comparable in size to data points. Inset: Guinier plot.	109
Figure 3.22. SAXS pattern of $c = 2$ mg/mL cerato-ulmin bubble dispersion with fit using different form factors: (A) Spherical core-shell model; (B) Cylindrical core-shell model.	110
Figure 3.23. SAXS pattern of $c = 2$ mg/mL cerato-ulmin bubble dispersion with fit two custom models: (A) Spherical bubbles with free CU proteins in solution; (B) Cylindrical bubbles with free CU proteins in solution.	111
Figure 3.24. SAXS pattern of $c = 2$ mg/mL cerato-ulmin bubble dispersion and fit with a combination of a core-shell cylinder model representing the assembled structure and Guinier regime mostly representing free protein in solution. Uncertainties are comparable in size to data points. Inset: Guinier plot.	112
Figure 3.25. Cerato-ulmin $c = 2$ mg/mL AFM images and height profiles for inflated and deflated bubbles: (A) single height profile across a collapsed bubble; (B) single height profile across an inflated bubble; (C) AFM image of collapsed bubbles (scale bar = 5 μm); (D) AFM of zoomed in on one bubble (scale bar = 1 μm).	117
Figure 3.26. Suggested shape of cerato-ulmin cylindrical bubbles. The bubble has an inner diameter of 40 nm and outer diameter of 70 nm with a five-protein thick film with alternating hydrophobic and hydrophilic patches from the CU proteins. Take with permission from reference 98.	118
Figure 4.1. A wave flume has a small width and large length which allows for fluid flow to be considered two-dimensional	124
Figure 4.2. Diagram of regular surface waves at the air-water interface with key variables. For a tank with a flat bottom and small width, fluid flow can be modeled with Airy wave theory	125
Figure 4.3. Orbital motion of particles in a wave with shallow, intermediate, and deep depths. Adapted from reference 155.	131
Figure 4.4. Wave Tank 1.1 was constructed of clear acrylic with internal dimensions of $152 \times 6 \times 76$ mm. When filled halfway, the tank holds 37 mL of CU solution.	134
Figure 4.5. Scotch yoke engine mechanism. The crank's rotational motion creates a linear motion in the horizontal bar.	135

Figure 4.6. Wave tank assembly 1.0 uses a scotch yoke engine driving a paddle vertically to create water waves.	136
Figure 4.7. The acoustic impulse wave tank uses a surface transducer to drive a paddle against the latex membrane.....	138
Figure 4.8. The scotch yoke mechanism for the sloshing tank used a gear and pulley system to drive rotation of the pin.	139
Figure 4.9. Scotch yoke engine connected to carriage plate connected to MakerSlides for slosh tank apparatus.	140
Figure 4.10. The full sloshing tank apparatus setup uses a scotch yoke engine connected to a carriage plate with a three-dimensional translation stage between a custom-built horizontal microscope.	141
Figure 4.11. Attractive forces between the CU solution and the glass walls create a meniscus with the vertex at the midpoint of the glass walls.....	142
Figure 4.12. Microscope imaging of wave tank: (A) Schematic of wave tank setup with real image plane located at the vertex of meniscus (B) Resulting image from this schematic (scale bar = 200 μm).	143
Figure 4.13. Microscope imaging of wave tank: (A) Schematic of wave tank setup with real image plane offset from the vertex of meniscus (B) Resulting image from this schematic (scale bar = 200 μm).	143
Figure 4.14. CU bubbles form in the wave tank with different agitation frequencies (scale bar = 200 μm): (A) No agitation; (B) 0.8 Hz; (C) 1.5 Hz; (D) 3.5 Hz.	145
Figure 4.15. Bubble number density with different agitation frequencies.	146
Figure 4.16. Bubble length distribution over time for $f = 1.5$ Hz agitation.	147
Figure 4.17. Bubble length distribution for $f = 3.5$ Hz agitation.	148
Figure 4.18. Cylindrical CU bubble reorienting parallel to the meniscus over time (scale bar 100 μm): (A) $t = 0$ sec; (B) $t = 1.81$ sec; (C) $t = 3.17$ sec.....	149
Figure 4.19. Bent CU bubble straightening over time (scale bar 200 μm): (A) $t = 0$ sec; (B) $t = 1.02$ sec; (C) $t = 1.47$ sec.....	150
Figure 4.20. The kinked CU bubble straightens as it encounters the meniscus (scale bar = 200 μm): (A) $t = 0$ sec; (B) $t = 0.890$ sec; (C) $t = 2.247$ sec.....	150
Figure 4.21. Diagram of CU bubble with three points of interest for video tracking (scale bar = 100 μm).	151
Figure 4.22. Vector diagram of bubble schematic showing ϕ and θ are complementary angles.	152
Figure 5.1. Ray diagram for a particle in an optical trap. Adapted from reference 168.	159
Figure 5.2. Seven silica bullets in a 3x3 optical tweezer trap using a 1064 nm laser.....	162

LIST OF SYMBOLS AND ABBREVIATIONS

AFM	Atomic Force Microscopy
CU	Cerato-ulmin
DAM	Dummy Atom Model
DC	Direct Current
DLS	Dynamic Light Scattering
LINAC	Linear Particle Accelerator
MAD	Multi-wavelength Anomalous Dispersion
MALDI	Matrix Assisted Laser Desorption Ionization
MAXS	Middle Angle X-ray Scattering
MIR	Multiple Isomorphous Replacement
MR	Molecular Replacement
ORNL	Oak Ridge National Laboratory
P3HT	Poly(3-hexylthiophene-2,5-diyl)
PDDF	Pair Distance Distribution Function
RPM	Revolutions Per Minute
SAD	Single-wavelength Anomalous Dispersion
SANS	Small-angle Neutron Scattering
SAXS	Small-angle X-ray Scattering
SEM	Scanning Electron Microscope
SLD	Scattering Length Density
SNS	Spallation Neutron Source
SSRL	Stanford Synchrotron Radiation Lightsource
STM	Scanning Tunneling Microscope
TCB	1,2,4-trichlorobenzene
TEM	Transmission Electron Microscope
TFA	Trifluoroacetic Acid
USAXS	Ultra-Small-angle X-ray Scattering
WAXS	Wide Angle X-ray Scattering

SUMMARY

Hydrophobins are a class of amphipathic fungal proteins with a high surface activity, high resistance to thermal and chemical degradation, and in some cases good availability at low cost. These properties make hydrophobins excellent candidates for a variety of applications for coatings, drug delivery, chemical separations, and encapsulations. Cerato-ulmin (CU) is a hydrophobin produced by the two fungal species, *Ophiostoma ulmi* and *O. novo-ulmi*, known for their connection to Dutch elm disease. When an aqueous sample of CU is gently agitated, the proteins assemble into a collection of aspherical bubbles, many of them cylindrical. These large bubbles rise out of a solution due to their buoyancy but dynamic light scattering (DLS) results show remaining submicron structures remain indefinitely. These structures respond to positive and negative pressure changes both before and after initial formation suggesting that the structures are bubbles. Agitating a CU solution creates a spectrum of bubbles ranging from $10^{-7} - 10^{-4}$ m. The physical characteristics of both the submicron and micron bubble films were investigated. For the submicron bubbles, small-angle x-ray scattering and small-angle neutron scattering show the bubbles are cylindrical with a ~ 70 nm cross-sectional diameter and film thickness of 15 nm, the equivalent of 5 CU proteins. Atomic force microscopy of collapsed microbubbles has the same film thickness suggesting that film thickness is independent of CU bubble size. To isolate singular bubble sizes during agitation, a new experimental apparatus was designed and built to agitate the CU solutions in a controlled, reproducible method. The apparatus houses a horizontal microscope for imaging CU bubbles directly after agitation and observing their motion as they rise through the solution.

Results show a positive correlation with agitation frequency and bubble size, with a steady number density for all sizes up to the maximum size at that frequency value.

CHAPTER 1. INTRODUCTION

1.1 Hydrophobins

Hydrophobins are a class of proteins from filamentous fungi in the Basidiomycota and Ascomycetes divisions of the fungi kingdom. These fungi have extending hyphae that consistently grow on moist substrates with multiple locations of air-water interfaces. The hydrophobins secreted by these fungi have unique characteristics that make them well suited to these situations. Hydrophobins are low molecular weight (7-9 kDa) proteins most well known for their amphipathic properties and ability to self-assemble at hydrophobic-hydrophilic interfaces.¹⁻⁴ Wessels et al.⁴ coined the term after investigating the basidiomycete species *Schizophyllum commune* and discovering cysteine-rich proteins with a high amount of hydrophobicity. They are one of the most surface-active proteins and are able to reduce surface tensions in aqueous solutions from 72.8 mN/m to values of 25-45 mN/m depending on concentration and type of hydrophobin.⁵⁻⁶ One protein of *Schizophyllum commune* in particular, Sc3, was extensively studied because of its ability to self-assemble into amphipathic films at a hydrophobic/hydrophilic interface (i.e. air/water, oil/water).^{3, 7-9}

Hydrophobins are divided into two categories: class I and class II. The class I hydrophobins assemble into an amphipathic film composed of 5-12 nm amyloid rodlets. They have a hydrophobic patch that is larger than that of class II hydrophobins, which may be responsible for the former's ability to form rodlets or display increased insolubility.¹⁰ These films are highly insoluble and only are disassociated by trifluoroacetic acid (TFA) or formic acid.^{4, 11} After dissociation and evaporation of the solvent, the hydrophobins'

ability to reassemble is unaffected. Both class I and class II hydrophobins have similar hydropathy patterns and contain eight conserved cysteine residues that provide four disulfide bonds. All hydrophobins can self-assemble into amphipathic films at a hydrophobic/hydrophilic interface. Most proteins in water fold in a manner to create a core of hydrophobic residues with the hydrophilic residues on the surface. Hakanpää et al.¹² found the class II hydrophobin HFBII to be globular with a central β barrel structure with two loop regions of aliphatic side chains. These chains create a “hydrophobic patch” resulting in a natural Janus particle containing a hydrophobic and hydrophilic surface. The key feature in allowing the hydrophobic patch to exist is the four disulfide bonds. They are not involved in the self-assembly but rather keep the protein folded and keep the monomer soluble in aqueous solutions.¹³ Similar work on the structure of class I hydrophobins yielded the same explanation for the existence of the hydrophobic patch.¹⁴

Hydrophobins often cause hydrophilic surfaces to become hydrophobic and hydrophobic substances to be hydrophilic. In nature, they have a variety of functions such as aiding the growth of aerial hyphae and fruit bodies^{4, 15}, attaching to hydrophobic surfaces¹⁶, and providing gas channels in hyphae¹⁷. Due to their surface-active properties they are useful materials in a variety of functions: stabilization of emulsions in the food industry¹⁸⁻²⁰, functionalizing surfaces²¹, aiding in drug delivery²², and increasing alignment of semiconducting polymers.²³

1.2 Biological role

Compared to the plant, animal, and bacteria kingdoms, fungi do not quite captivate the public’s attention in terms of press, research funding, or general interest. Despite this,

fungi are an important kingdom on the planet and have a direct impact on the entire human race. Each year, 300 million people are infected with fungal diseases with 1.6 million fatalities.

While fungi appear to closely related to plants from a visual perspective, they behave like animals in some ways. Instead of photosynthesis, fungi travel to a food source and consume the material. The primary method of movement for fungi is through the growth of hyphae. Hyphae are filamentous, branched, tube-like structures that combine into a network called the mycelium. The hyphae grow at their tips and frequently encounter air liquid interfaces. At this point hydrophobins are typically secreted. The hydrophobins act to lower the surface tension and ease the process of growth of the hypha across the interface (Figure 1.1).²⁴

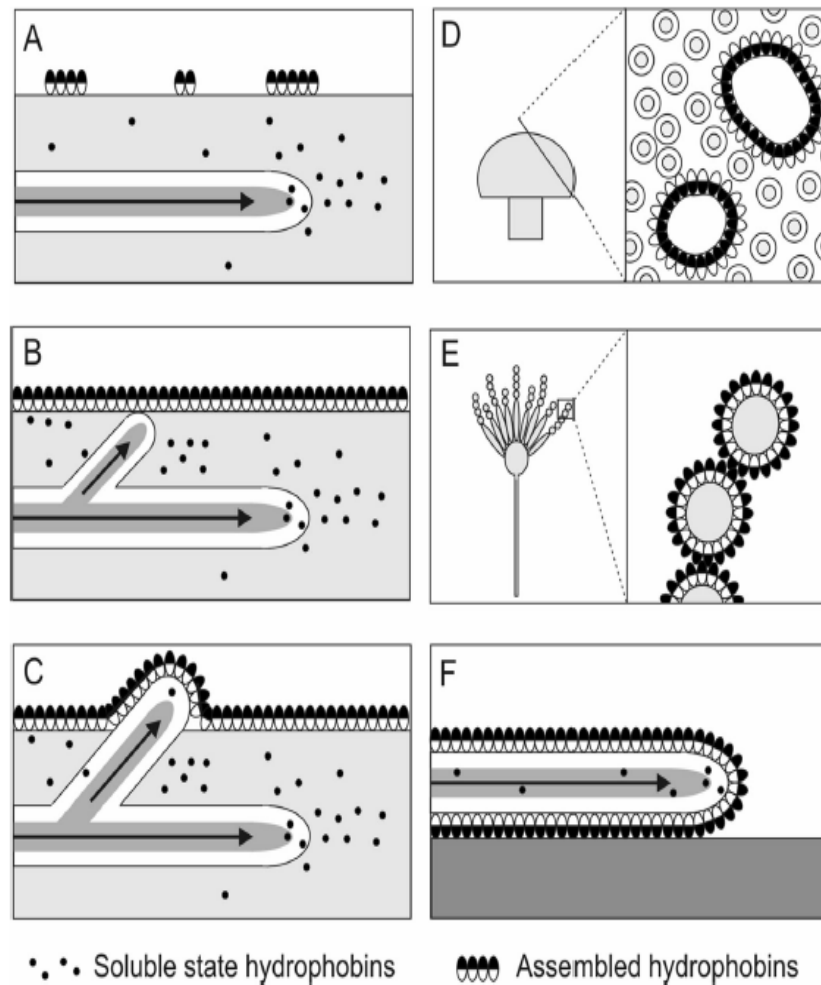


Figure 1.1. Model of the biological role of hydrophobins during growth and development of filamentous fungi. Soluble hydrophobin is secreted at the tip of the growing, submerged hypha and diffuses into the aqueous environment (A). The water surface tension is lowered due to the assembly of hydrophobins into an amphipathic membrane at the medium-air interface (B), allowing the hypha to breach the medium-air interface and grow into the air. The hydrophobin protein molecules secreted by emerging aerial hyphae cannot diffuse into the environment and assemble at the cell wall-air interface (C). Aerial cavities in fruiting bodies are lined with an assembled hydrophobin layer preventing water from filling these cavities (D). Hydrophobins also play a role in the dispersal of spores by coating them with an amphipathic hydrophobin layer (E). Via assembly at the interface between the cell wall and a hydrophobic surface, hydrophobins mediate attachment to the surface, for example, during infection of host tissue (F). Take with permission from reference 25.

1.3 Structure

Protein structure is generally broken up into 4 parts: primary, secondary, tertiary, and quaternary. The primary structure is the sequence of amino acids. The secondary structure is any local structure in segments such as α -helices, and β -sheets. The tertiary structure is the three-dimensional (3D) structure of the overall protein and location of α -helices, and β -sheets. The quaternary structure is beyond the individual protein and relates to the relative position and orientation of multiple proteins that align into a larger structure, typically with non-covalent bonding through the hydrophobic effect.

With respect to the primary structure, hydrophobins are not the most homologous group of proteins. For example, the hydrophobins *SC3* and *SC4* have less than 50% homology in their primary structure. The most defining structural characteristic of hydrophobins is their eight cysteine residues with conserved spacing that allows them to create four disulfide bonds (Figure 1.2 and Figure 1.3).²⁶

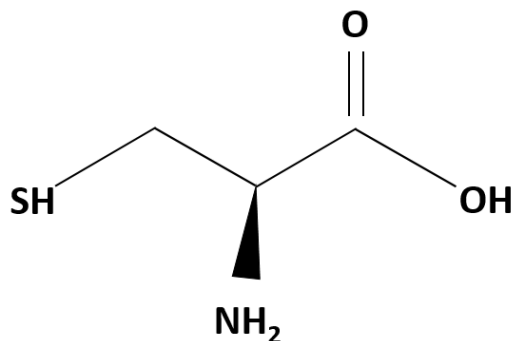


Figure 1.2. Chemical structure of the cysteine amino acid. The sulfur molecule and the resulting disulfide bonds in hydrophobins are crucial to their structure.

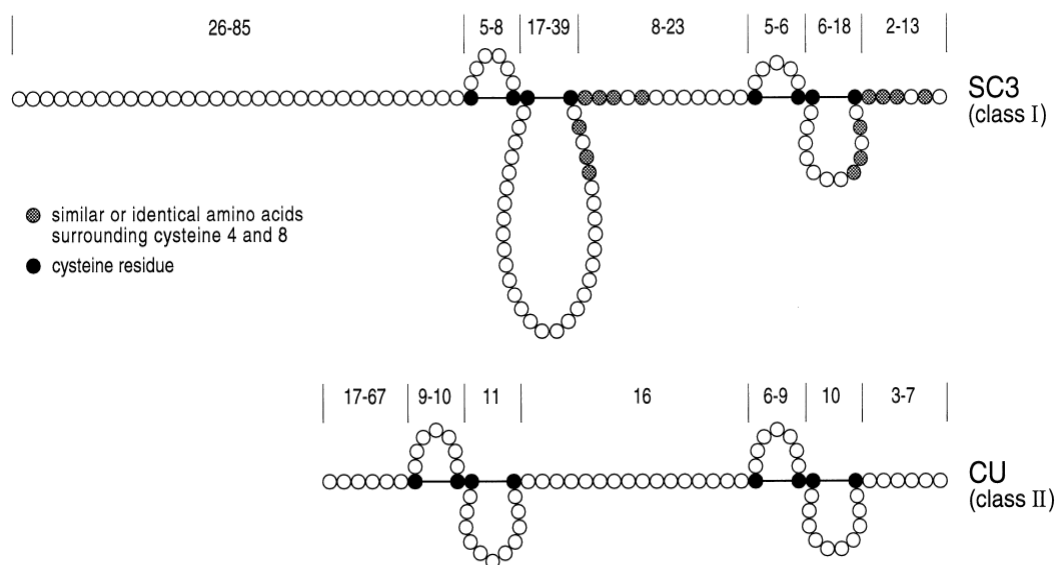


Figure 1.3. Hydrophobins contain 8 cysteine residues with conserved spacing. These residues pair together to form disulfide bonds. Take with permission from reference 26.

In the sequence below the X represent any amino acid besides tryptophan, the C is the cysteine amino acid, and the subscripts are the number of potential amino acids in the fragment.²⁷

$$X_{2-38} - C - X_{5-9} - C - C - X_{11-39} - C - X_{8-23} - C - X_{5-9} - C - C - X_{6-18} - C - X_{2-13} \quad (1)$$

The existence of cysteine residues does not make hydrophobins unique. Other small proteins contain a small number of cysteine residues such as certain snake toxins²⁸, chitin-binding lectins²⁸, and extracellular lipid transfer proteins.²⁹ These proteins, however, do not have the same amphipathic properties or engage in self-assembly. The disulfide bonds that are created stabilize the protein and prevent it from self-assembling in solution and only at hydrophobic-hydrophilic interfaces.¹³ In addition to the four disulfide bonds,

hydrophobins also contain α -helices and β -sheets in the protein secondary structure (Figure 1.4).

Crystallizing hydrophobins is a very difficult procedure due to their hydrophobic properties,³⁰ yet Hakanpää et al. were first able to form crystals of HFBII³¹ and characterize them with x-ray crystallography.^{12, 32} They found that the protein is globular with dimensions of 2.4×2.7×3.0 nm with a 0.10 nm resolution. The protein contains one β -barrel of four β -strands, one α -helix, and four disulfide bonds that function to hold the protein in its shape (Figure 1.5 and Figure 1.6). The hydrophobic patch that gives the amphipathic properties to the protein are in the one of the β -strands of each of the two β -hairpins (S1 and S4). The residues in these β -strands are aliphatic and create the hydrophobic surface patch. Because of the conserved spacing of hydrophobic residues in all hydrophobins (Figure 1.7), it is likely they have their hydrophobic surface patch because of the S1 and S4 β -strands.

While many proteins have aliphatic residues that are hydrophobic, they generally fold into the center of the molecule to escape the water. The four disulfide bonds in hydrophobins prevents this though because it gives rigidity to the protein and prevents the β -strands S1 and S4 from folding into the core of the protein.¹²

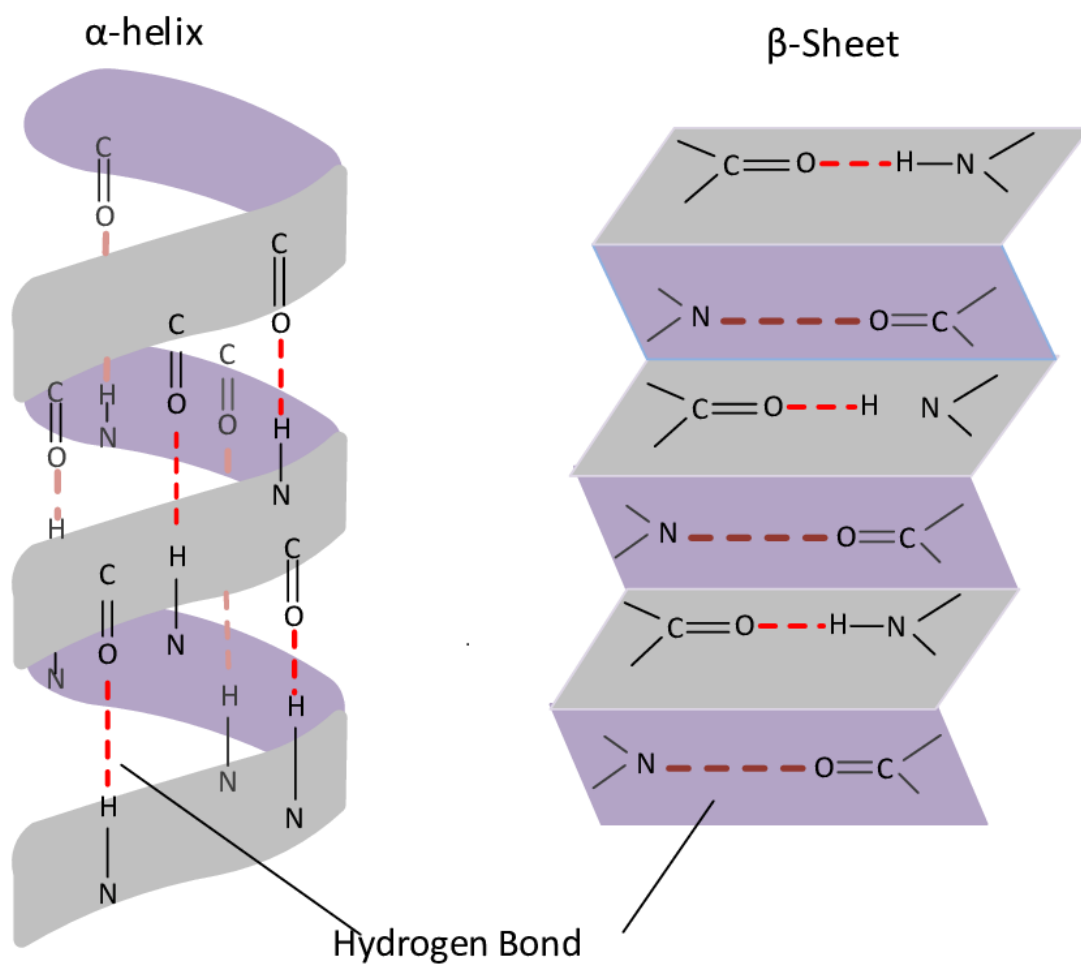


Figure 1.4. Hydrophobins contain a mixture of α -helices and β -sheets beta sheet in their secondary structure. Every β -sheet is a mix of multiple β -strands that are connected laterally through hydrogen bonding. Take with permission from reference 33.

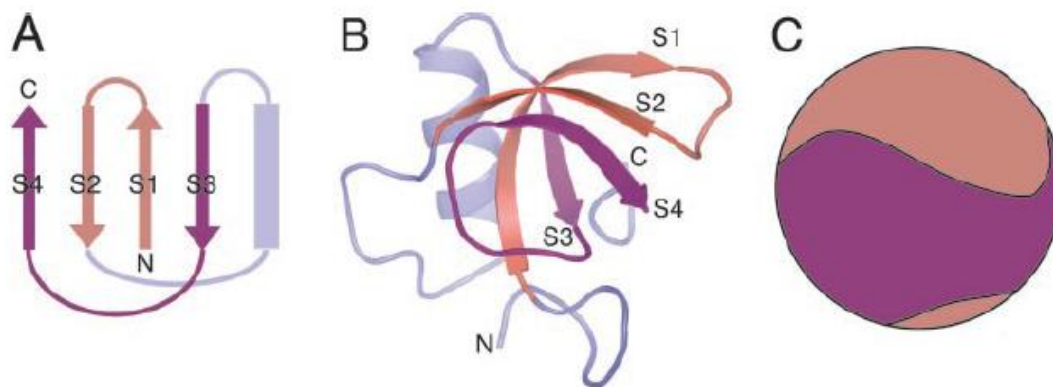


Figure 1.5. Topology and structure of HFBII. (A) topology of HFBII the *arrows* β - strands and the *rectangle* the α -helix. (B) three-dimensional structure of HFBII. The first β -hairpin is in *red* and the second in *purple*. The central β -barrel consists of two β -hairpins that interlock in the same way as the leather pieces of a baseball (C). Take with permission from reference 12.

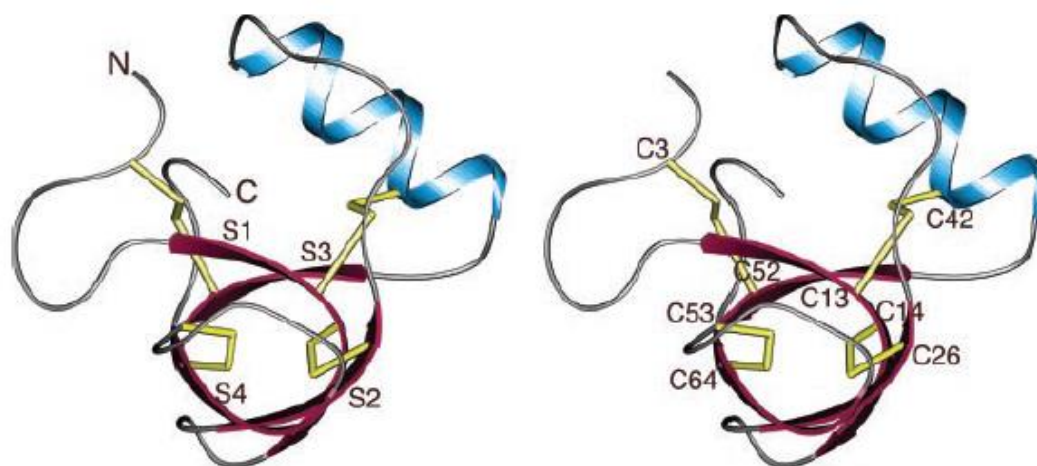


Figure 1.6. The structure of HFBII in stereo showing β -barrel and four symmetrically arranged disulfide bridges in yellow. β -strands and Cys residues are labeled. Take with permission from reference 12.

	1	10	20	30	40	50	60	70																																																																		
	—S1→		—S2→		====helix====		—S3→		—S4→																																																																	
HFBI1	A	V	C	P	T	G	L	F	S	N	P	L	C	C	A	T	N	V	L	D	L	I	G	V	D	C	K	T	P	T	I	A	V	D	T	G	A	I	F	Q	A	H	C	A	S	K	G	S	K	P	L	C	C	V	A	P	V	A	D	Q	A	L	L	C	Q	K	A	I	G	T	F	---		
HFBI	N	V	C	P	P	G	---	L	F	S	N	P	Q	C	C	A	T	Q	V	L	G	L	I	G	L	D	C	K	V	P	S	Q	N	V	Y	D	G	T	D	F	R	N	V	C	A	K	T	G	A	---	Q	P	L	C	C	V	A	P	V	A	G	Q	A	L	L	C	Q	T	A	V	G	A	---	
SRH1	S	V	C	P	N	G	---	L	Y	S	N	P	Q	C	C	G	A	N	V	L	G	V	A	A	L	D	C	H	T	P	R	V	D	L	T	G	P	I	F	Q	A	V	C	A	A	E	G	G	K	Q	P	L	C	C	V	V	P	V	A	G	Q	D	L	L	C	E	E	A	Q	G	T	F	---	
QID3	A	L	C	P	A	G	---	L	Y	S	N	P	Q	S	C	A	T	D	V	L	G	L	A	D	L	D	C	A	V	P	S	S	T	P	P	H	D	G	P	N	F	Q	S	I	C	V	A	N	G	G	K	R	A	R	C	C	V	L	P	V	L	G	L	V	L	C	Q	P	N	P	V	T	G	---
TRI1	Q	P	C	P	A	G	---	L	Y	S	N	P	Q	C	C	A	T	D	V	L	G	V	A	D	L	D	C	K	N	P	S	S	A	P	T	S	A	P	M	S	G	D	N	F	K	S	I	C	H	A	V	Q	---	Q	A	K	C	C	V	L	P	V	A	G	Q	A	V	L	C	D	---			
TRI2	O	A	C	P	A	G	L	---	L	Y	S	N	P	Q	C	C	S	T	G	V	L	G	V	A	D	L	D	C	K	N	P	S	S	A	P	T	S	G	D	D	F	O	K	I	C	A	N	G	G	Q	---	Q	A	O	C	C	S	I	P	V	A	G	Q	A	V	L	C	D	P	A	I	---		
CPPH1_2	S	A	C	P	S	G	---	L	Y	S	N	P	Q	C	C	A	T	D	V	L	G	V	A	S	L	D	C	V	N	P	S	S	K	P	R	S	G	D	D	F	K	S	T	C	G	A	E	G	---	H	A	S	C	C	A	I	P	V	A	G	Q	G	V	L	C	D	P	A	---					
CPPH1_4	S	A	C	P	S	G	---	L	Y	S	N	P	Q	C	C	S	T	D	V	L	G	V	A	S	L	D	C	V	N	P	S	S	K	P	R	S	G	D	N	F	K	S	T	C	A	A	A	G	K	---	H	A	S	C	C	V	I	P	V	A	G	Q	G	V	L	C	D	P	---					
CPPH1_3	---	A	C	P	S	G	---	L	Y	S	N	P	Q	C	C	S	T	D	V	L	G	V	A	S	L	D	C	V	N	P	S	S	K	P	R	S	G	D	N	F	K	S	T	C	A	A	A	E	K	---	H	A	S	C	C	V	I	P	V	A	G	Q	G	V	L	C	D	P	---					
TRI3	F	K	C	P	S	G	---	L	Y	S	V	P	Q	C	C	A	T	D	V	L	G	V	A	D	L	D	C	G	N	P	S	R	Q	P	T	D	S	S	D	F	A	S	V	C	A	A	K	G	Q	---	R	A	R	C	C	V	L	P	L	L	G	Q	A	V	L	C	T	G	A	---				
CPPH1_5	E	V	C	P	S	G	---	L	Y	S	V	P	Q	C	C	A	T	G	L	I	G	V	L	D	L	D	C	Q	S	P	S	R	T	S	F	S	S	D	F	K	S	T	C	R	S	E	G	---	K	A	R	C	C	V	L	P	V	A	G	Q	D	V	L	C	N	P	L	---						
CPPH1_1	K	P	C	P	S	G	---	L	Y	S	N	P	Q	C	C	S	T	N	V	L	G	V	A	A	L	N	C	K	T	P	S	F	A	P	T	S	F	Q	S	F	K	S	A	C	S	G	G	Q	---	Q	C	C	V	V	P	A	A	G	Q	G	V	L	C	D	P	A	I	---						
CRYPA	T	A	C	S	S	T	---	L	Y	S	E	A	Q	C	C	A	T	D	V	L	G	V	A	D	L	D	C	E	T	V	P	E	T	T	S	A	S	S	F	E	S	I	C	A	T	S	C	R	---	D	A	K	C	C	T	I	P	L	G	Q	A	L	L	C	D	P	V	G	L	---				
CU	D	P	C	T	G	L	---	L	Q	K	S	P	Q	C	C	N	T	D	I	L	G	V	A	N	L	D	C	H	G	P	P	S	V	F	T	S	P	S	Q	F	Q	A	S	C	V	A	D	G	G	R	S	A	R	C	C	T	L	S	L	L	G	L	A	L	V	C	T	D	P	V	G	I	---	
MAG	T	P	C	S	G	---	---	L	Y	G	S	A	Q	C	C	A	T	D	I	L	G	L	A	N	L	D	C	G	Q	S	P	D	A	P	V	D	A	N	F	S	E	I	C	A	A	I	G	Q	---	R	A	R	C	C	V	L	P	L	D	Q	G	I	L	C	N	T	P	A	G	V	T	P	---	
HCF5	D	V	C	P	A	---	---	L	D	T	P	L	C	C	Q	A	D	V	L	G	V	L	D	L	T	C	E	A	P	S	D	---	T	S	V	N	F	E	A	A	C	A	T	T	G	L	---	T	A	R	C	C	T	L	P	L	L	G	E	A	L	L	C	T	P	---								
HCF6	D	V	C	P	A	---	---	L	D	T	P	L	C	C	Q	A	D	V	L	G	V	L	D	L	T	C	E	A	P	S	D	---	T	S	V	N	F	E	A	A	C	A	T	T	G	L	---	T	A	R	C	C	T	L	P	L	L	G	E	A	L	L	C	T	P	---								

Figure 1.7. Amino acid sequence comparison of class II hydrophobins. The secondary structure elements are given in the first row. The Cys residues are in black, and the residues found in the hydrophobic patch are in red. Protein identification related to the abbreviations used are: HFBII, *T. reesei* (accession P79073); HFBI, *T. reesei* (accession P52754); SRH1, *Trichoderma harzianum* (accession Y11841); QID3, *Trichoderma harzianum* (accession P52755); TRI1, TRI2, and TRI3, the three segments of TH1 *Claviceps fusiformis* (accession Q9UVI4); CPPH1_1, CPPH1_2, CPPH1_3, CPPH1_4, and CPPH1_5, the five segments of cpph1 *Claviceps purpurea* (accession AJ418045); CRYPA, Cryparin *Cryphonectria parasitica* (accession P52753); CU, Cerato-ulmin *Ophiostoma ulmi* (accession Q06153); MAG, Magnaporin *Magnaporthe grisea* (accession AF126872); HCF5, *Cladosporium fulvum* AJ133703; HCF6, *C. fulvum* (accession CAC27408). Take with permission from reference 12.

In addition to HFBII, there are other proteins where the 3D structure is known (Figure 1.8). The class I hydrophobins EAS (*Neurospora crassa*)³⁴, DewA (*Aspergillus didulans*)³⁵⁻³⁶, MPG1 (*Magnaporthe grisea*)³⁷, and RodA (*Aspergillus fumigatus*)³⁸ all have known 3D structures. For the class II hydrophobins HFBI (*Trichoderma reesei*)¹⁰, HFBII (*Trichoderma reesei*)^{12,31}, and NC2 (*N. crassa*)³⁹ the 3D structures are also known. All these proteins share the four β -strands that make up the β -barrel with some hydrophobins having α -helices. While the four disulfide bonds keeping the core of the protein together are immutable, the α -helix and β -strands do experience conformational changes with different environments.

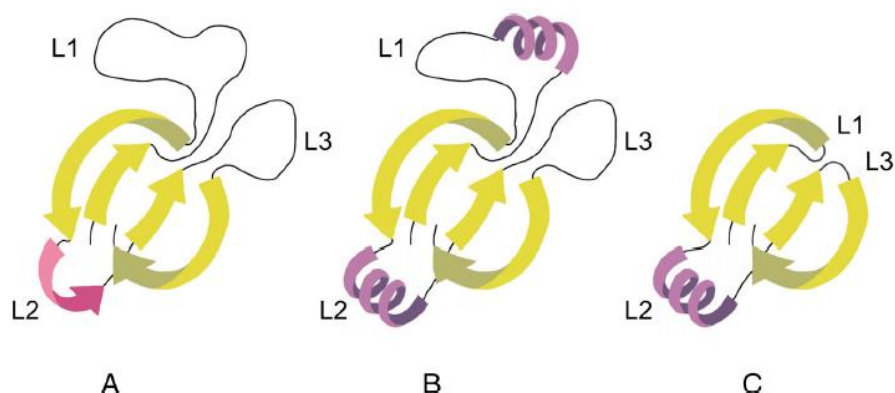


Figure 1.8. Schematic representation of the 3D structure of class I (a, b) and class II (c) hydrophobins. Both types of hydrophobins contain a four stranded β -barrel core (a–c; in green) and either α -helical (b, c) or β -sheet (a) structure in loop 2 (L2). In class I hydrophobins (a, b), loops 1 and 3 (L1 and L3) are relatively large and are unstructured (a; EAS) or contain α -helical structure (b; DewA, RodA, and MPG1). Class II hydrophobins (c; HFBI, HFBII, and NC2) are relatively compact and have a small L1 and L3. Take with permission from reference 24.

Conformational changes may happen when hydrophobins undergo assembly. At a hydrophobic/hydrophilic interface, the hydrophobin SC3 will undergo changes in its structure from α -helical to β -sheet 1 and finally to a more stable β -sheet 2.⁴⁰ For an air-water interface, the conversion process completes the first step in a matter of minutes but takes hours to arrive at the final β -sheet 2. The β -sheet 2 phase has a minimal water surface tension and is most stable. Removal of the coating at this stage requires detergent or low pH.⁴⁰ However, the conformational changes are not universal across all hydrophobins. For the class II hydrophobins HFBI and HFBII, there are no changes in conformational structure as they assemble and the air-water interface.^{5, 26}

Hydrophobins undergo β -sheet to alpha helix transformations during assembly (Figure 1.9). The class I hydrophobins feature some β -sheet structure in their monomeric form, which increases during self-assembly. The interfaces at the protein's site of self-

assembly also affects the hydrophobin structural evolution. For an air-water interface, the hydrophobin film has an increase in α -helix structures within seconds before arriving at a final state featuring β -sheet structures. In the case of a water/hydrophobic solid interface, the hydrophobins stay in the intermediate α -helix structure indefinitely unless further treated with heat or detergent.²⁶

The hydrophobin examined in this dissertation, cerato-ulmin, is a class II hydrophobin, which, like all class II hydrophobins, assembles into a film on the air-water interface and is much more soluble than class I hydrophobins. Compared with class I hydrophobins, class IIs are more conserved in the spacing of amino acids between the cysteine residues.⁴¹ Rather than needing a strong acid, class II hydrophobins such as CU, HFBI and HFBII are dissolved by ethanol or SDS.⁴²⁻⁴³ This makes them better candidates for applications needing reversible processes or for applying easily removable coatings.

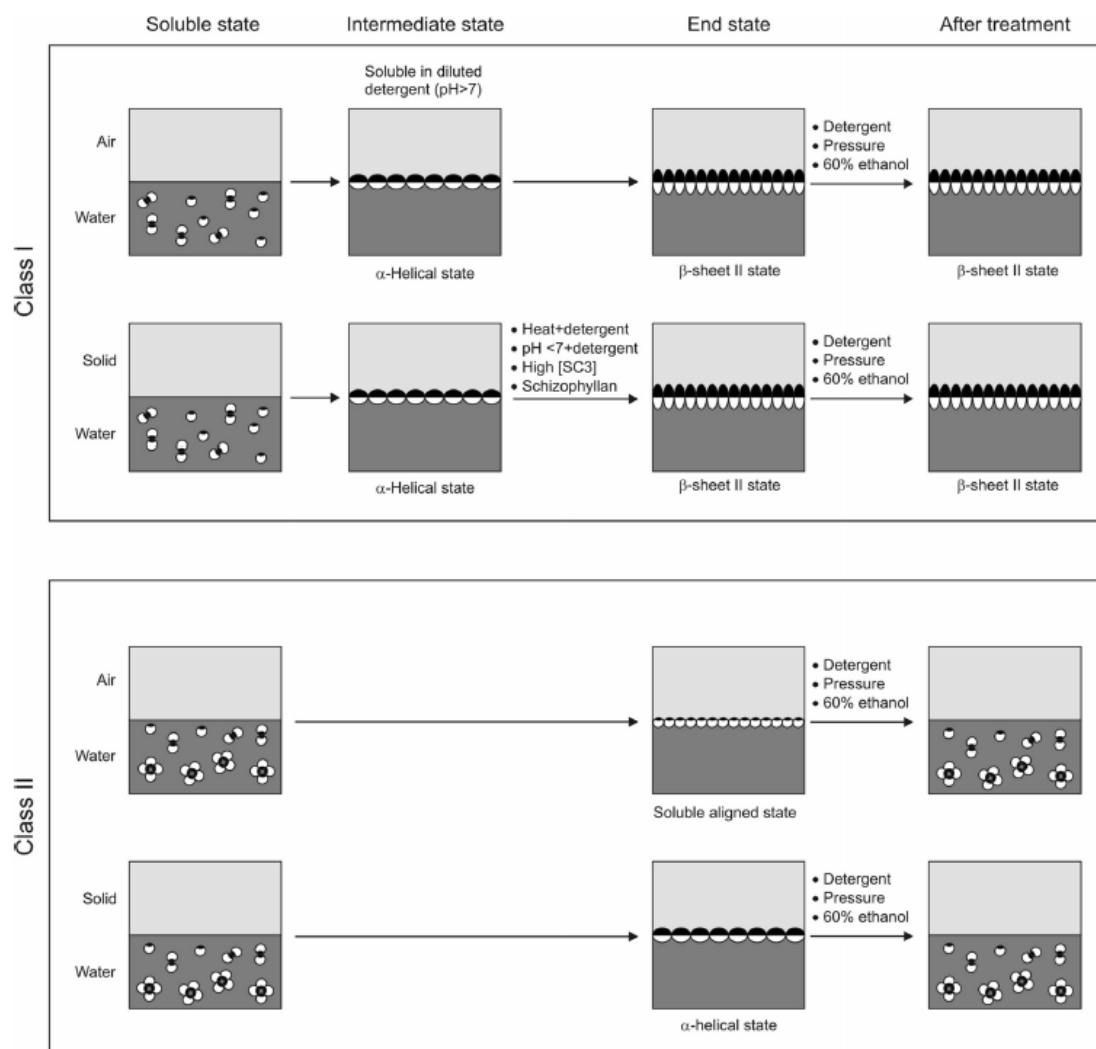


Figure 1.9. Assembly of class I and class II hydrophobins. Take with permission from reference 24.

1.4 Applications

The properties of hydrophobins create many potential material applications in a wide range of fields. The most appealing properties are hydrophobins' surface activity, behavior at interfaces, solubility modifications to other materials, and durability of their assembled films. Hydrophobins are also non-toxic for humans — the hydrophobin ABH1

is in the edible mushroom in the grocery store — so they are possible material candidates for many food and medical applications.⁴⁴⁻⁴⁶

1.4.1 Dispersants

Hydrophobins are used for materials with electrochemical properties. These materials commonly create problems with solution aggregation, as they do not disperse well. One material that is commonly known to have extreme potential in a wide variety of fields is carbon nanotubes. These aggregate in solution, which decreases their usefulness and can hamper their excellent properties. Both single and multi-wall carbon nanotubes were stabilized in solutions with the hydrophobins HFGI, EAS, and HYD3.⁴⁷⁻⁴⁸

Hydrophobins also assist in not only dispersing hydrophobic materials but can assist in alignment. Rosu et al. found that the addition of cerato-ulmin to a solution of Poly(3-hexylthiophene-2,5-diyl) (P3HT) in trichlorobenzene could help with the molecular alignment of the P3HT.²³ This effect was even produced with the concentration of cerato-ulmin being two orders of magnitude less than the P3HT. The consequences of this could lead to the development of crystalline, high-performance thin films for flexible electronics.

1.4.2 Coatings

Hydrophobins' excellent surface activity causes them to assemble onto surfaces and make them great candidates for coatings because they can switch the polarity of surfaces. The hydrophobin SC3, for example, can functionalize Teflon™ surfaces.²¹

Teflon™ is commonly used in medical devices and its functionalization by a hydrophobin could be of potential benefit. The addition of a hydrophobin to an implant has

aided in the growth of fibroblasts on its surface.⁴⁴ By coating a plastic stent with the hydrophobin yaaD-DewA-His6, the adsorption of human bile on the stent was reduced for an in vitro study.⁴⁹ While future work done with animal studies did not yield the same results additional modifications could lead to success.⁵⁰

Another potential use for hydrophobin coatings could be in the marine industry for application to the hull of boats. The hydrophobins' functionalization of surfaces prevents the growth of organisms on a ship's hull.⁵¹

1.4.3 Foams and Emulsions

Hydrophobins are also useful for applications in liquids as they are able to stabilize hydrophobic liquids, act as a foaming agent, and add stability to foams.^{5-6, 52-53} With the addition of an emulsion-stabilizing powder, a hydrophobin emulsion will have months of stability.⁵³ This stability helps increase the shelf life of food products. They even have an added potential benefit in nutrition. The hydrophobin HFBII can be used as an aerating agent to produce air-filled emulsions to replace fat-filled emulsions in a variety of foods. The foods taste the same but changing the emulsion will help decrease the caloric intake of the consumer.⁵⁴ The current problem in aerating food to replace the fat-filled emulsion is the slow escape of the air over time, which makes the food have an unacceptably low shelf life. The hydrophobins act as a "shell" around the air bubble to prevent the release of air and stabilize the air bubbles better than other proteins.⁵⁵⁻⁵⁶ With the addition of a thickening agent, the hydrophobin HFBII stabilized an aerated foam for 2.5 years with little or no air loss.⁵⁷

The excellent foaming ability of hydrophobins is not always beneficial though. The sudden foaming and gushing of beer is primarily due to hydrophobins.⁵⁸⁻⁶⁰ This not only can create spillage and subsequent sadness for the drinker but also be a problem in manufacturing. The gushing of beer during mass production can cause significant material loss and economic damage. Multiple studies aim to understand the process and to help inhibit gushing, thus helping beer drinkers around the world from spilling their beers.^{58, 60-}

64

1.4.4 Biomedical

Hydrophobins assist in biomedical applications and their non-toxicity allows them to be candidate materials for a variety of applications. As mentioned previously, hydrophobins have potential in medical implants.⁴⁴ They also can be used in drug delivery^{22, 65-68} and medical imaging.⁶⁹

Many drugs are insoluble in water. Coating a drug in hydrophobins creates the solubility in water that is needed for delivery. This method has been successfully used for oral, topical, and intravenous drugs. Besides coating the drugs hydrophobins can aid delivery by modifying the surface of a drug-loaded carrier such as porous silicon or cellulose.^{65, 70-71}

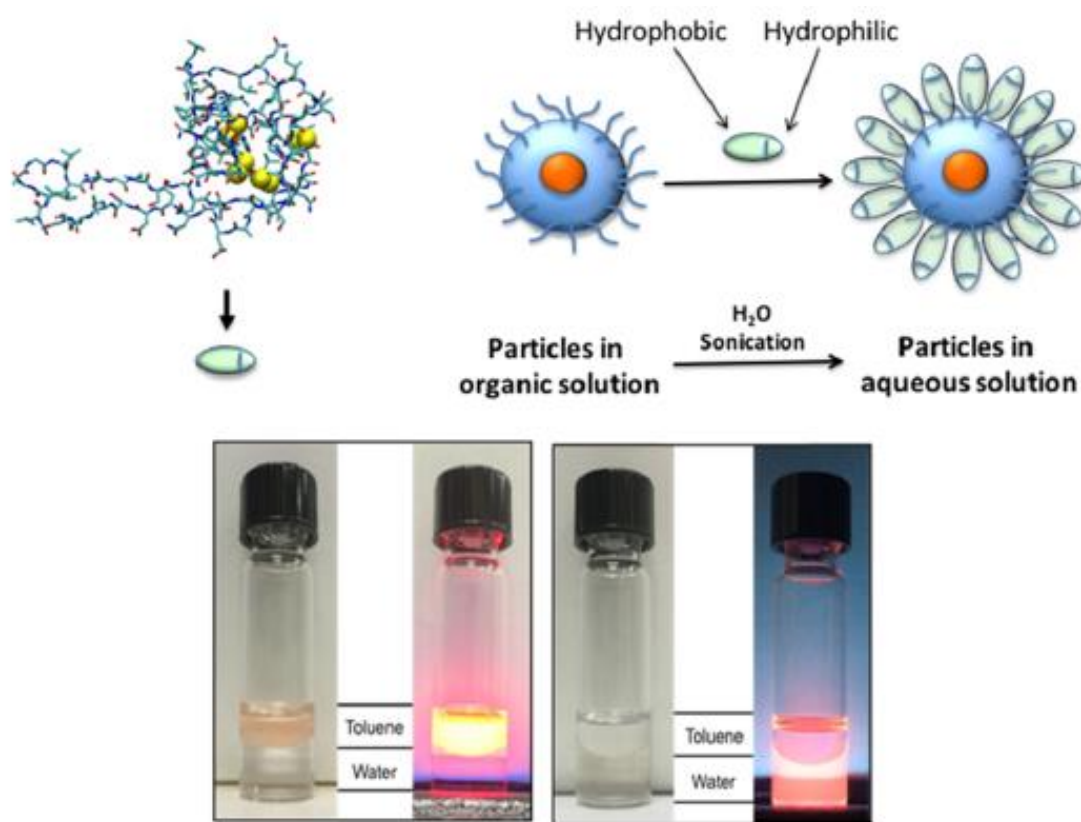


Figure 1.10. Hydrophobins encapsulating quantum dots for biomedical imaging.
Take with permission from reference 69.

Hydrophobins also have uses in medical imaging. Quantum dots are semiconductor nanoparticles with unique electrical and optical properties. Because their electrical and optical properties are based on size, the dots have size-tuneable emission wavelengths and narrow emission bands. This makes them a good candidate material for medical imaging in addition to the drug delivery and sensory applications (Figure 1.10).⁷² Quantum dots are not water soluble, however, and require either encapsulation or surfactant exchange to enable use. The amphipathic nature of hydrophobins allows for the encapsulation of the quantum dot to achieve the needed solubility for application.⁶⁹

1.5 Cerato-ulmin

Cerato-ulmin is closely linked to Dutch elm disease, one of the most destructive forestry diseases in history. By some estimates the disease has destroyed 28 million elm trees in the United Kingdom and over a billion trees worldwide since 1970.⁷³⁻⁷⁴ Elm bark beetles spread the disease as they feed on different trees. For a time, CU was suspected to be a toxin from the fungus *Ceratocystis ulmi* but more recent work shows that it merely helps spread the toxins by reducing surface tension thus enabling growth at the interface.⁷⁵

Cerato-ulmin was first isolated by Takai et al. after noting the formation of microstructures in the toxic metabolites.⁷⁶ They noted that the protein formed rods or fibrils but did not denote them as bubbles even though they recognized its sensitivity to pressure. Cerato-ulmin contains 73 amino acid residues and, like other class II hydrophobins, is highly conserved with the spacing of the eight cysteine amino acids. The secondary structure is comprised of 15% α -helix and 50% β -sheet with all cysteine residues creating four disulfide bonds.⁷⁷ It is a highly surface active protein and lowers the surface tension of water even at concentrations of 0.03 $\mu\text{g/mL}$.⁴³ At higher concentrations of 50 $\mu\text{g/mL}$, CU can reduce surface tension from 72 mN/m to 25 mN/m.⁷⁸

The properties of CU have not been studied as extensively as those of other class II hydrophobins such as HFBII.^{6, 12, 79-87} CU is not as easily obtainable and its association with Dutch elm disease may give pause to some researchers. As a class II hydrophobin, CU has many of the same properties of well-known proteins such as HFBII but also exhibits behavior not seen in other proteins. Russo et al.⁸⁸ noted that CU formed persistent

cylindrical bubbles on the microscopic scale and more recently, Zhang et al. demonstrated that with a specific pressure cycle, CU formed stable, toroidal bubbles (Figure 1.11).

Cerato-ulmin's propensity for elongation into cylinders may have application in aiding semiconducting polymer alignment in flexible electronics.²³ Rosu et al. combined a CU dispersion with a poly(3-hexylthiophene) (P3HT) solution in 1,2,4-trichlorobenzene (TCB). The cerato-ulmin encapsulated the P3HT in TCB solution forming a membrane between the water and solution. If drop cast onto a glass slide and allowed to evaporate, the shrinkage of the CU membrane during solvent evaporation exerted pressure on the P3HT molecules to align and improve conductivity.

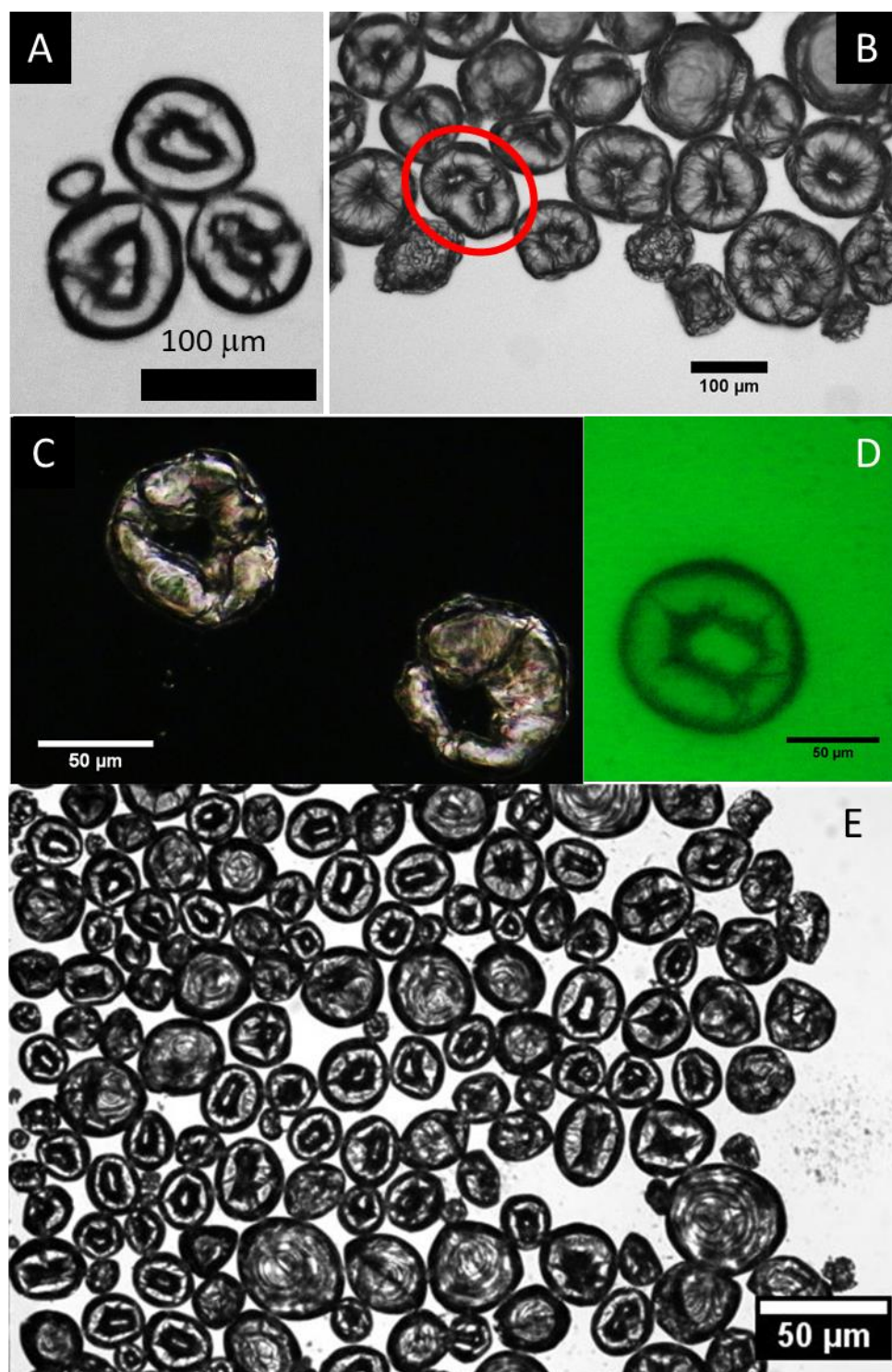


Figure 1.11. Bright-field (A, B and E), dark-field (C) and negative-fluorescent (D) microscope images of toroidal microbubbles with wrinkles stabilized by CU. Take with permission from reference 89.

CHAPTER 2. EXAMINATION OF SUBMICRON STRUCTURES IN AN AQUEOUS AGITATED CERATO-ULMIN SOLUTION

2.1 Introduction

Bubbles are defined as thin films of liquid surrounding a gas; they are such a common occurrence that they would not be considered to have a date of discovery. Our understanding of bubbles is not new; the physics of bubbles are described by the Young-Laplace equation for surface tension derived in 1830.⁹⁰ It may not appear there is much room for scientific discovery in bubbles, but in the last 50 years studies on bubbles with sizes on the micro and nano length scales has led to applications in medical imaging,⁹¹⁻⁹² drug delivery,⁹³ paints or coatings,⁹⁴ and food additives.^{20, 95-96} These smaller bubbles are categorized according to their sizes into microbubbles (1-100 μm), submicron ($<1 \mu\text{m}$), and nanobubbles ($<100 \text{ nm}$).

This chapter investigates the submicron particles in CU solutions after agitation. In the previous chapter, experimental fitting of SAXS curves suggest that these are not aggregations but actual cylindrical bubbles like the micron bubbles seen in an optical microscope. The results from one experimental technique should not be considered conclusive so a series of pressure experiments was designed to further buttress or refute the hypothesis of submicron bubbles.

The experiments undertaken provide further evidence that the particles are bubbles as their size is pressure dependent for both positive and negative pressure changes. These bubbles also exhibit hysteresis in cycling pressure experiments. The effect of time and pH

on bubble characteristics was explored in time-dependent experiments. These experiments showed a size decrease with time as the larger bubbles rise out of the solution but with the small bubbles remaining in the solution indefinitely. The pressure experiments are published results in the *Journal of Physical Chemistry B*.⁹⁷

2.2 Dynamic Light Scattering

Dynamic light scattering (DLS) is a particle sizing technique for sizes between a few nanometers up to a micron. The foundation of DLS is built upon the Brownian motion of particles. When photons interact with a sample, the particles will scatter some of the light. The intensity of the scattered light is dependent on the measurement angle, photon wavelength, and particle characteristics. In static light scattering experiments the average intensity at a specific angle is recorded and plotted as a function of the scattering vector q . This intensity is not completely static because the particles in the solution are constantly in Brownian motion and their relative distance between one another causes destructive and constructive interference patterns in the light (Figure 2.1).

As the particles move the inter-particle distances change as do the interference patterns. With a lens/aperture/pinhole arrangement (Figure 2.2) it is possible to observe these constructive and destructive interference patterns. The fluctuating intensity of the light in the speckle pattern is directly correlated to the motion of the particles in the solution.

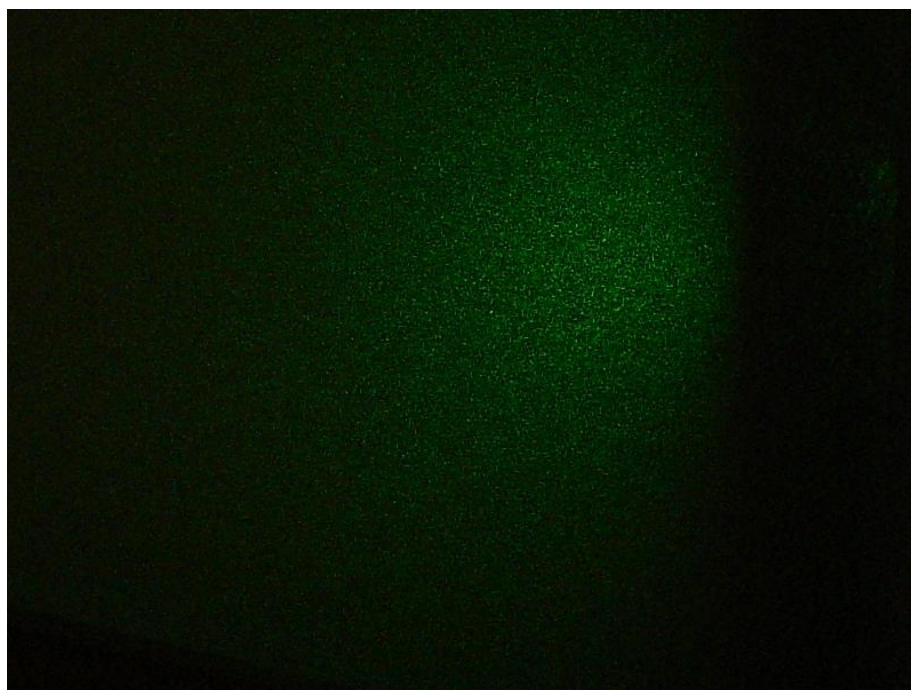


Figure 2.1. The speckle pattern from a DLS measurement is due to the constructive and destructive interference of light as the particles move.

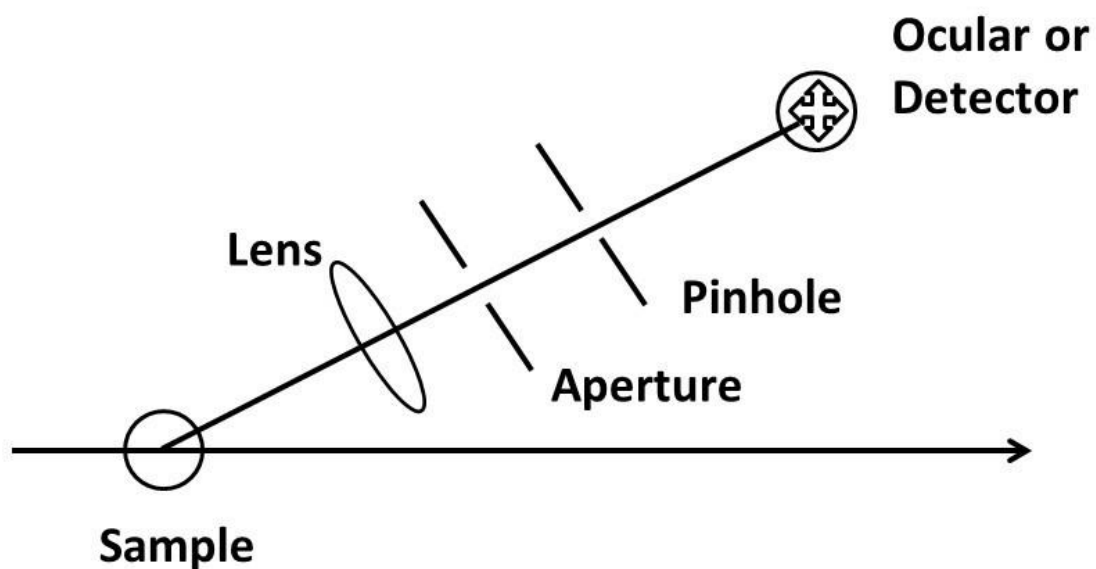


Figure 2.2. Dynamic light scattering setup. After the light is scattered from the sample it travels through a focusing lens, aperture and pinhole before reaching a detector.

Using an autocorrelation function, it is possible to relate the intensity fluctuations and diffusion of the scattering particles.

$$G^{(2)}(t) = \langle I(0)I(t) \rangle = \lim_{T \rightarrow \infty} \frac{1}{2T} \int_{-T}^T I(t') \cdot I(t' + t) dt' \quad (2)$$

$G^{(2)}(t)$ is a second-order autocorrelation function that describes how long the signal intensity is correlated. In this expression, T is the overall time of the measurement, I is the intensity, and t is an independent variable describing the lag time between the independent variable and the controlling variable that constructs the correlation function. The integral limits for the time T span over all time, but in practice it is only necessary to use a large enough T to fully capture the decay. Choosing a T value that is four orders of magnitude greater than the exponential time constant τ is enough to capture most of the autocorrelation function.

At small lag times the particles have not moved a significant amount of distance so the speckle pattern from constructive and destructive interference will be similar as the intensities are correlated. As the lag time increases the particles have moved and are in a completely new arrangement, which causes an unrelated speckle pattern and uncorrelated intensities. The second order autocorrelation function is approximated with the Siegert relationship

$$G^{(2)}(t) = B(1 + f|g^{(1)}(t)|^2) \quad (3)$$

where B is a baseline, f is an instrumental parameter, and $g^{(1)}(t)$ is the electric field autocorrelation function. In most cases this is described as a single exponential or a sum of exponentials of the form $g^{(1)}(t) = Ae^{-\Gamma t}$ where Γ is the decay rate

$$\Gamma = \tau^{-1} = q^2 D_m \quad (4)$$

The decay rate is the inverse of exponential time constant and is related to the mutual diffusion coefficient D_m and scattering vector q . This relationship follows Fick's second law of diffusion $\frac{\delta C}{\delta t} = D \frac{\delta^2 C}{\delta x^2}$ where the first derivative of concentration with time equals the diffusion times the second derivative of concentration with distance. This results in the calculation of the particle hydrodynamic radius through the Stokes-Einstein equation

$$R_h = \frac{kT}{6\pi\eta_0 D_0} \quad (5)$$

where R_h is the hydrodynamic radius, k is the Boltzmann constant, T is the temperature, η_0 is the viscosity, and D_0 is the diffusion extrapolated to infinite diffusion. For the case of dilute samples used in this work it is appropriate to assume $D_m \approx D_0$.

At this juncture, it is worthwhile to provide an explanation of the hydrodynamic radius R_h because it is commonly misunderstood and confused with other measurements. When describing the size of objects, especially for sizes below the macroscale, the radius is described as a hydrodynamic radius R_h , radius of gyration R_g , or physical radius R . The hydrodynamic radius, sometimes referred to as the Stokes radius, relates to its diffusion through the Stokes-Einstein equation and is the radius of a hard sphere diffusing through the same solvent. It is not a direct physical measurement as it depends on the

sample/solvent interactions and shape. The radius of gyration R_g is the root mean square of the distance between all the subunits and its center of mass. In the general case for any particle the radius of gyration R_g is defined as

$$R_g^2 = \frac{\sum_i^n m_i r_i^2}{\sum_i^n m_i} \quad (6)$$

where m_i is the mass of each subunit and r_i is the distance between the subunit and the center of mass. The final description for radii is the physical radius. This is generally used to describe objects measured through direct means such as optical microscopy, scanning electron microscopy (SEM), or transmission electron microscopy (TEM). All three of these measurements are correlated and there are analytical expressions for their relationship with common shapes such as hollow and solid spheres, cylinders, and polymer chains.

There are three common methods to fitting DLS results and calculating R_h : cumulant fitting, multi-exponential fitting, and Laplace inversions. For well-behaving monodisperse particles cumulant fitting is enough, but for polydisperse or multi-component systems multi-exponential and Laplace inversions are recommended.

2.2.1 Cumulant Fitting

Cumulant analysis was first introduced by Koppel⁹⁸ as a way to simplify computing decay rates by fitting the natural log of the electric field autocorrelation function $g^{(1)}(t)$ with a polynomial instead of fitting $g^{(1)}(t)$ directly with Laplace inversions. The polynomials are typically first, second, or third order cumulants based off the Taylor expansion of $\ln(x)$

$$\ln[g^{(1)}(t)] = K_0 - \Gamma t \quad (7)$$

$$\ln[g^{(1)}(t)] = K_0 - \Gamma t + \frac{\mu_2}{2} t^2 \quad (8)$$

$$\ln[g^{(1)}(t)] = K_0 - \Gamma t + \frac{\mu_2}{2} t^2 - \frac{\mu_3}{6} t^3 \quad (9)$$

The decay rate Γ is called the first cumulant for all order fits and represents the average value for all the scatterers in the viewing volume. For monodisperse samples the cumulant fits provide correct results as all the particles will diffuse at the same rate. As a sample increases in polydispersity or if there is a mix of different particles in a solution the cumulant fitting will begin to fail. For example, in a solution with two different sized particles the cumulant fit will yield the average decay rate and predict an incorrect size. Therefore, using cumulant fits for polydisperse or multi-component samples is an incomplete analysis and different fitting procedures become useful.

For a perfectly monodisperse solution, the correlation function will be fully described by a single exponential so $\mu_2 = 0$ and the parameter $\frac{\mu_2}{\Gamma^2} = 0$. All solutions will have some slight size or shape differences that create small differences in diffusion rates for individual particles, so the single exponential is never a perfect fit. A monodisperse standard such as silica or latex will have a value of $\frac{\mu_2}{\Gamma^2} \sim 0.03$. If $\frac{\mu_2}{\Gamma^2} \geq 0.3$ there is a large size distribution or there are multiple components in the sample of different sizes. The resulting R_h is derived from the average cumulant $\bar{\Gamma}$ and it is impossible to determine if there are any particles in the solution of that size or if the R_h is just a weighted average

between two multiple components. At this point multi-exponential fitting or Laplacian inversions must be employed to make this determination.

2.2.2 *Multi-Exponential Fitting*

When cumulant fitting does not yield complete results, multi-exponential fitting is typically the next choice. Multi-exponential fitting assumes the solution is a mix of two or more individually monodisperse particles and fits the normalized second-order autocorrelation function

$$g^{(2)}(t) = B + \beta(A_1 e^{-\Gamma_1 t} + A_2 e^{-\Gamma_2 t} + \dots A_n e^{-\Gamma_n t})^2 \quad (10)$$

where B is a baseline factor, A is the amplitude, Γ is the decay rate, β is an instrumental parameter, and n denotes separate scattering populations. As more exponentials are used the number of variables increases and it becomes difficult to make meaningful conclusions because there are so many potential solutions. The multi-exponential fit also assumes that each component in the sample is monodisperse. As polydispersity increases it becomes helpful to use more advanced fitting procedures to measure particle sizes.

2.2.3 *Inverse Laplace Transforms*

For all DLS samples there is a continuum of scattering particles with individual decay rates representing how they diffuse throughout the solution. Most samples will have individual particles with different decay rates due to size or shape discrepancies. Therefore, the most accurate representation of the electric field autocorrelation function is the summation of scatterers in the scattering volume.

$$g^{(1)}(t) = \sum_i A_i e^{-\Gamma_i t} \quad (11)$$

This can be rewritten as the integral

$$g^{(1)}(t) = \int_0^\infty d\Gamma A(\Gamma) e^{-\Gamma t} \quad (12)$$

which shows that $g^{(1)}(t)$ is a Laplace transform pair with $A(\Gamma)$. The Laplace inversion fitting routine CONTIN⁹⁹ chooses a number of decay rates Γ or grid points over a large range and fits $g^{(1)}(t)$ by calculating a fit for $A(\Gamma)$ at each grid point. Nonlinear least-squares fits typically minimize the squared residual χ^2 , which is the difference between the experimental data and the fitted function.

CONTIN works differently to minimize a modified χ^2 that contains a side constraint:

$$\chi^2 = \|e\|^2 + \alpha^2 \|\omega - \Omega x\|^2 \quad (13)$$

where $\|e\|^2$ is the residual norm, α is the regularizer, ω is a term for prior knowledge about the function, Ω is a restraining matrix, and x is the experimental data. The purpose of the side constraint is to prevent large perturbations in $A(\Gamma)$ over small $d\Gamma$. In actual samples there will not be a large population difference between scatterers with near identical decay rates. The side constraint functions in a similar manner to the looseness penalty in the ATSAS suite of programs for SAXS analysis (see Chapter 3). As α increases the fitting

program will be more predisposed to small changes in amplitudes over $d\Gamma$ at a cost of higher residuals.

2.3 Effect of Time

2.3.1 *Experimental Setup*

The DLS experiments were conducted on a custom-built apparatus with a rotating arm detector at scattering angles between 30-120 degrees and a Coherent OBIS 660 coherent laser with $\lambda_o = 660$ nm. Light intensity was measured with a Pacific Precision Instruments (Irvine, California) wide-range photometer/preamplifier/discriminator driving an ALV-5000 digital autocorrelator. Acquisition times were between 30-300 seconds to ensure a smooth correlation function. The ALV software fit experimental data using both cumulant fitting and the Laplace transform algorithm CONTIN.

Samples were prepared by mixing the purified sample with water through Barnstead Nanopure™ or Millipore Milli-Q purification systems into clean, dust-free glass vials and gently agitated by hand through a rocking motion to create the bubble dispersion. The clean, dust-free glass vials were treated by cleaning with soap and rinsing continuously with Nanopure® water for 1 hour before being wrapped in aluminum and placed in an oven to dry. To prevent particulates from entering, the glass vials remained wrapped in aluminum until solutions were introduced.

2.3.2 *Results*

In a solution, there are two main forces acting on a bubble in opposite directions. The buoyancy force $F_B = \rho_0 g V_{\text{displaced}}$ is determined by the density of the object ρ_0 ,

acceleration of gravity g , and $V_{\text{displaced}}$, which is the volume of the bubble. This force is directed upward to the surface of the liquid. The second force is the drag that acts opposite to the direction of motion. The drag force $F_D = \frac{1}{2}\rho_f v^2 C_D A$ is governed by the density of the fluid ρ_f , speed of the object v , drag coefficient C_D , and cross-sectional area A . Since this force scales with the square of velocity, the drag force becomes increasingly strong as speed increases. If an object's motion is due to a constant force such as gravity or buoyancy, there is a terminal velocity where the drag force becomes equal to the gravity or buoyancy and $F_{\text{net}} = 0$. At this point there is no further acceleration and velocity is constant. For large bubbles in water (>6 mm), the terminal velocity is $\sim 0.3 \text{ m}\cdot\text{s}^{-1}$.¹⁰⁰

The interesting consequences of these forces on bubbles begin when considering small bubbles. These bubbles displace a small amount of volume so there is a smaller buoyant force. Using the Navier-Stokes equation and considering only the buoyancy and drag forces, the terminal velocity of a bubble rising in a fluid is expressed by the Hadamard-Rybczynski equation:

$$v_t = \frac{2}{3} \frac{R^2 g (\Delta\rho)}{\mu_w} \frac{\mu_w + \mu_b}{2\mu_w + 3\mu_b} \quad (14)$$

where v_t is the terminal velocity, R is the radius, g is the gravitational acceleration, $\Delta\rho$ is the difference in density between bubble and water, μ_b is the viscosity of the bubble, and μ_w is the viscosity of the water.¹⁰¹ For an air bubble in water this reduces to

$$v_t = \frac{R^2 g \Delta\rho}{3\mu_w} \quad (15)$$

because $\mu_b \ll \mu_w$. This expression is only valid for a range of bubble sizes between 1-200 microns. For bubbles smaller than 1 micron the effect of Brownian motion has an equal or larger influence on the bubble's motion. The Brownian motion velocity of particles in a liquid is

$$v_{rms} = \sqrt{\frac{k_b T}{m^*}} \quad (16)$$

where k_b is the Boltzmann constant, T is temperature, and m^* is the effective mass which is the sum of the mass of the particle and half the mass of displaced fluid.¹⁰²⁻¹⁰³

At larger sizes, the terminal velocity begins to deviate from the Hadamard-Rybczynski equation around $d = 0.2$ mm as frictional forces begin to create oscillations at the bubble surface. The terminal velocity does not increase with the square of the radius and eventually becomes a constant $v = 0.3 \text{ m}\cdot\text{s}^{-1}$. A summary of the velocity behavior in bubbles is shown in Figure 2.3.

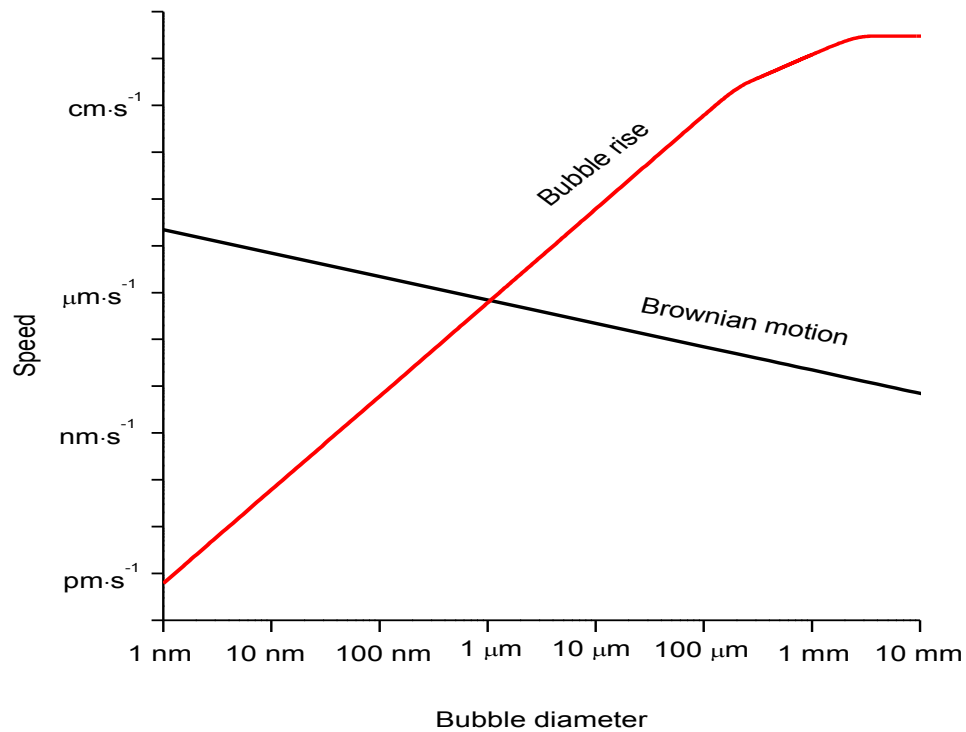


Figure 2.3. The terminal velocity of a rising bubble in solution (red) and the velocity due to Brownian motion (black). Adapted from reference 104.

For a 2.5 μm diameter bubble the terminal velocity is $3.8 \mu\text{m}\cdot\text{s}^{-1}$, more than five orders of magnitude slower than a visible bubble. For the smallest CU bubbles with $R_h \sim 100 \text{ nm}$, the terminal velocity is $24 \text{ nm}\cdot\text{s}^{-1}$. If one of these bubbles was an inch below the surface it would take more than 12 days to reach the surface in the absence of convection. This assumes the bubble is at terminal velocity, but this will not be the case because of Brownian motion. For a $\sim 1 \mu\text{m}$ diameter bubble, the velocity from Brownian motion is equal to the terminal velocity of the bubble rising (Figure 2.3). Once sizes become $< 1 \mu\text{m}$, the Brownian motion becomes the dominant factor in the bubble's trajectory. At these

smaller sizes it is not known how quickly the bubbles rise out of solution if they do at all. For CU bubbles, DLS shows the submicron bubbles are stable for at least 35 days.⁸⁹

When an undisturbed solution of CU is placed in a beam path there is a minimal amount of scattering. After agitating the solution, it becomes turbid as light is scattered from the bubbles in solution. The bubbles have a wide range of sizes and over time the large bubbles rise out of the solution leaving only small submicron bubbles. Figure 2.4 shows the evolution of correlation functions at different times post-agitation.

For the 10- and 20-minute measurements the correlation function does not fully decay. This is because there are still large bubbles rising through the solution and causing large intensity spikes as they pass through the scattering volume. These intensity fluctuations obscure the intensity fluctuations from the diffusion. After 30 minutes the functions are better behaved with only some long decay time, possibly from large bubbles. Within one hour, the large bubbles have risen out of the solution and scattering spectra shows a more singular decay.

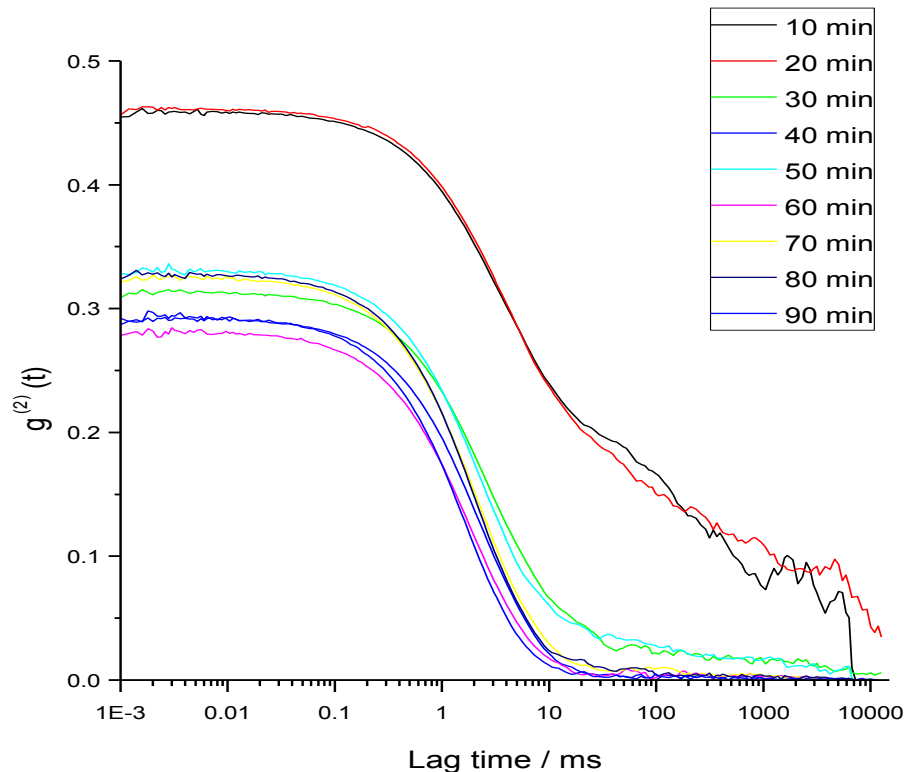


Figure 2.4. Normalized, baseline-subtracted DLS correlation functions measured at a scattering angle of 90° for cerato-ulmin solution ($c = 0.07$ mg/mL) measured at different times after agitation.

In Figure 2.5 the apparent hydrodynamic radius using cumulant fitting is plotted against the time after agitation. Beginning with the first two measurements of $R_{h,app} \approx 1600$ and 1000 nm it is inadvisable to claim that this is the average bubble size in the sample. The correlation functions are not well behaved, and it is known that the fluctuations are not only due to diffusion but also large bubbles passing through the scattering volume as they rise to the top of the solution. After 20 minutes the largest bubbles have passed through the scattering volume and correlation functions are more typical and yield more trustworthy size measurements. Examining the overall trend, the measurements show a sharp decrease

in measured radius as the larger bubbles rise out of the solution before plateauing at a consistent size after 1 hour. After leveling out, the apparent hydrodynamic radius $R_{h,app} = 160 \pm 19$ nm and this size is consistent at least 35 days.

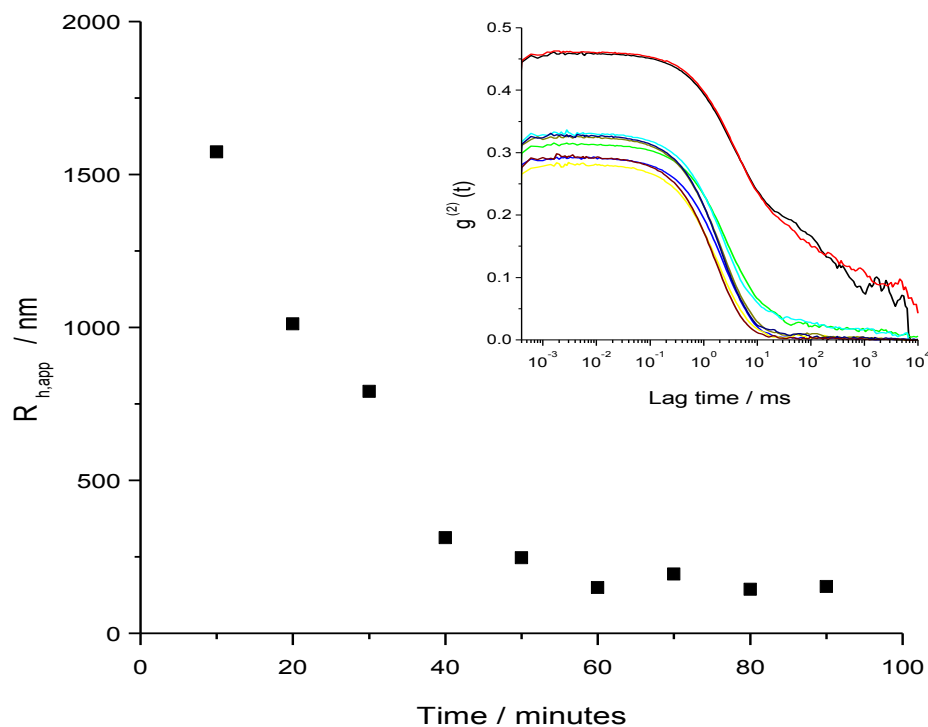


Figure 2.5. The apparent hydrodynamic radius of $c = 0.07$ mg/mL CU bubbles measured at 90° at different times with cumulant fitting. Inset are the normalized, baseline-subtracted DLS correlation functions at different times.

While this general trend is consistent, the plateau of $R_{h,app}$ is not constant as values range from 150-450 nm. The two likely factors that cause this inconsistency are the lack of reproducibility in sample agitation and sample volume. Agitating the solution by hand to

create the bubbles makes it impossible to replicate the exact motion every time. The second factor is the unknown effect of the sample volume.

In the DLS measurements, the CU samples are held in glass vials placed in the scattering instrument. The vials are agitated by hand and the fluid is “rocked” back and forth in the vial. For this type of agitation, most of the motion is at the surface and decreases with depth. If a glass vial contains too much sample, the agitation may not create enough bubbles or have the circulation to disperse bubbles across the entire depth. Even with attempting to use consistent volumes it is not known how sensitive the bubble formation is to sample volume. Both factors will be examined further in later chapters. The lack of reproducibility is covered in Chapter 4 with the design and construction of a wave tank. The sample volume is discussed in Chapter 5 as an avenue for potential future research.

2.4 Static Pressure Effects

Showing that an agitated CU solution creates microbubbles is an easy task because the bubbles are observable under a microscope. This allows the bubbles’ existence to be confirmed by tracking them rising through the solution using a horizontal microscope or inducing size changes with varying pressure. Both these methods show that on the microscopic scale CU forms bubbles. For the submicron case it is more difficult to demonstrate this as optical microscopy is no longer possible. Thus, DLS experiments are conducted when a CU solution is both agitated and measured at a single pressure value. By repeating this at different pressures it is possible to determine the effect of pressure on the size of the CU bubbles.

2.4.1 *Experimental Setup*

The DLS experiments were conducted on the same apparatus described earlier with the same preparation and procedure. Samples were connected to a Harvard apparatus PHD 2000 syringe pump via Tygon[®] tubing to control the pressure. An Extech 407910 Manometer measured a relative pressure with respect to the surrounding atmosphere.

For each measurement, the sample was adjusted to an absolute pressure between 0.7 and 1.3 bar before a solution with $c = 0.1$ mg/mL CU was agitated by hand in a figure-eight motion and placed in the sample holder. After placement into the holder, the sample was left undisturbed for one hour to permit large bubbles to rise out of the scattering volume.

2.4.2 *Results*

When agitated by hand, aqueous dispersions of CU protein assemble into “rod” or “fibril” bubbles on the micron scale (Figure 2.6). Investigators⁴³ suggested the presence of a number of other structures in these suspensions, but they found it difficult to investigate by scattering methods in the presence of large bubbles. In a glass vial this will cause the solution to appear cloudy, but after approximately one hour the large bubbles will rise to the top and the solution will become clear (Figure 2.5).



Figure 2.6. Cerato-ulmin bubbles created through gentle hand agitation of solution with a rocking motion (scale bar = 100 μm). Taken with permission from reference 97.

To determine whether the structures are bubbles or solid particles, solutions were agitated by hand while held at various applied pressures. The solutions were held at those pressures for one hour prior to and during DLS measurement. The difference in the resulting structures can be appreciated even from the raw correlation functions (Figure 2.7). The submicron structures were smallest (correlation functions decayed fastest) when overpressure (1.2 bar) was applied during agitation, aging, and measurement. In contrast, when the solutions were prepared, aged, and measured under mild vacuum (0.8 bar) the correlation functions decayed more slowly and exhibited distinct non-exponential

character. The slow secondary decay at long lag times potentially represents even larger structures, but the apparent sizes associated with the slower mode are sufficiently high that artifacts such as number fluctuations may interfere.¹⁰⁵

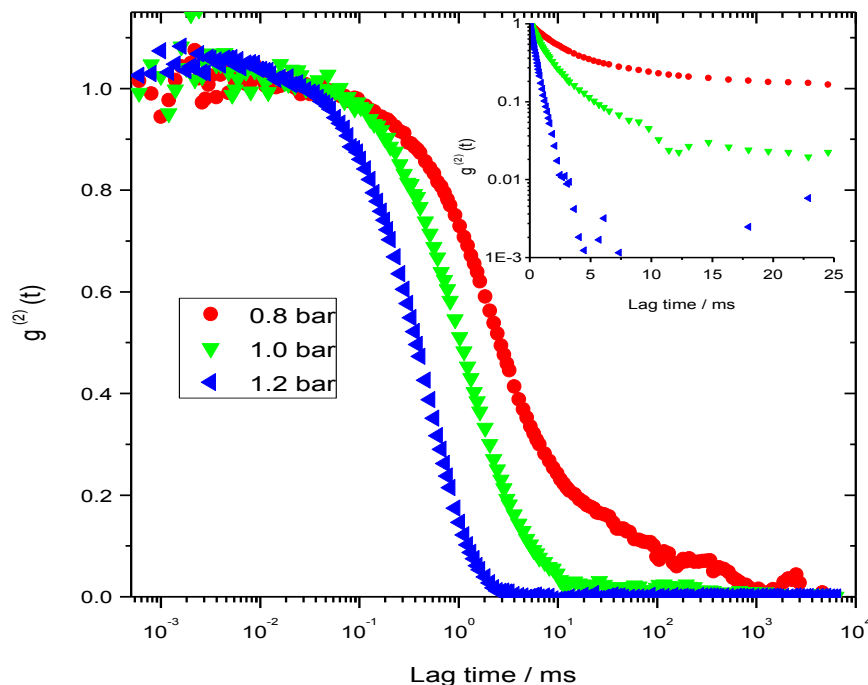


Figure 2.7. Normalized, baseline-subtracted DLS correlation functions measured at a scattering angle of 90° for cerato-ulmin solution ($c = 0.1$ mg/mL) agitated by hand at different pressures. Decay rates are significantly decreased at higher pressures meaning the scatterers have a smaller hydrodynamic radius R_h . Inset: Semi-log plot of normalized, baseline-subtracted DLS correlation function.

The cumulant method was used to calculate the bubble sizes in Figure 2.8 and provides some insights into the samples. Pressure clearly influences bubble formation as radii change from 100-700 nm at 90 degrees when the sample is set to different pressures. The effect is not well behaved though as the largest and smallest size measurements do not correspond with the lowest and highest pressure setting, respectively.

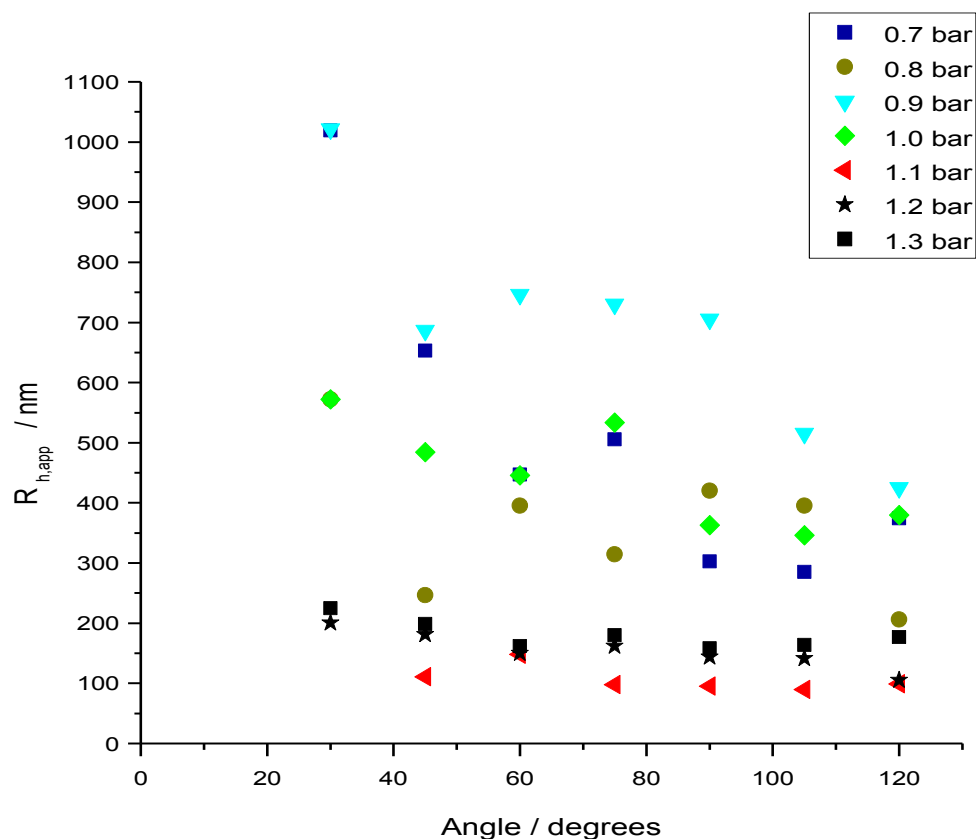


Figure 2.8. Cumulant analysis of dynamic light scattering of $c=0.1$ mg/mL CU agitated by hand at various pressure.

Another feature in Figure 2.8 is the hydrodynamic radius angle dependence. For monodisperse samples there is no angular dependence, but when there is a broad size distribution or multi-component system R_h changes with angle due to intensity differences from different sized particles. Even though cumulant analysis calculates the average $\bar{\Gamma}$ it is not based off the number of scatterers but the amplitude A of scattering power. The amplitude A_i is a weighted factor describing the contribution of each Γ_i to the average cumulant $\bar{\Gamma}$

$$\bar{\Gamma} = \frac{A_1\Gamma_1 + A_2\Gamma_2 \dots + A_n\Gamma_n}{A_1 + A_2 \dots + A_n} \quad (17)$$

The scattering power for particles in the Rayleigh regime will scale with the sixth power of diameter so larger particles dominate the overall amplitude. At low q the larger particles are measured due to the relation $q = \frac{2\pi}{d}$ where d is the scattering characteristic length. The slower diffusion of larger particles will shift the cumulant to a lower average value and increase R_h . As the scattering angle increases the smaller particles make a greater contribution to the scattering amplitudes, which will reduce the measured R_h . Therefore, a sample with a broad size distribution will have a decreasing R_h with increased angle while a monodisperse sample shows no angular dependence.

Keeping these relationships in mind, the CU bubble sizes at partial vacuum have a large angular dependence with high R_h at low q . The sharp decline with scattering angle suggests the presence of larger scatterers whose influence is muted at high q due to its reduced scattering. When CU solutions are agitated with an applied pressure the bubble size and angular dependence is reduced (Figure 2.8). The slight angular dependence is a result of a small size distribution while the smaller sizes suggest that increased pressures reduce the CU protein's ability to form large bubbles.

The polydispersity parameter $\frac{\mu_2}{\Gamma^2}$ is a dimensionless identity describing the size distribution. Values of $\frac{\mu_2}{\Gamma^2} \geq 0.3$ signify that the distribution is large around the average radius or the sample is a multi-component system. Figure 2.9 shows increased pressures prevent the CU from creating wide size distributions or multiple sized bubbles. At absolute

pressures between 0.7-1.0 bar the bubbles are not in a tight distribution; they are either polydisperse or multi-component. This supports the hypothesis that the CU forms bubbles on the submicron scale as well as the micron scale. If the submicron scatterers were not bubbles, only mere aggregates, there should be no pressure dependence.

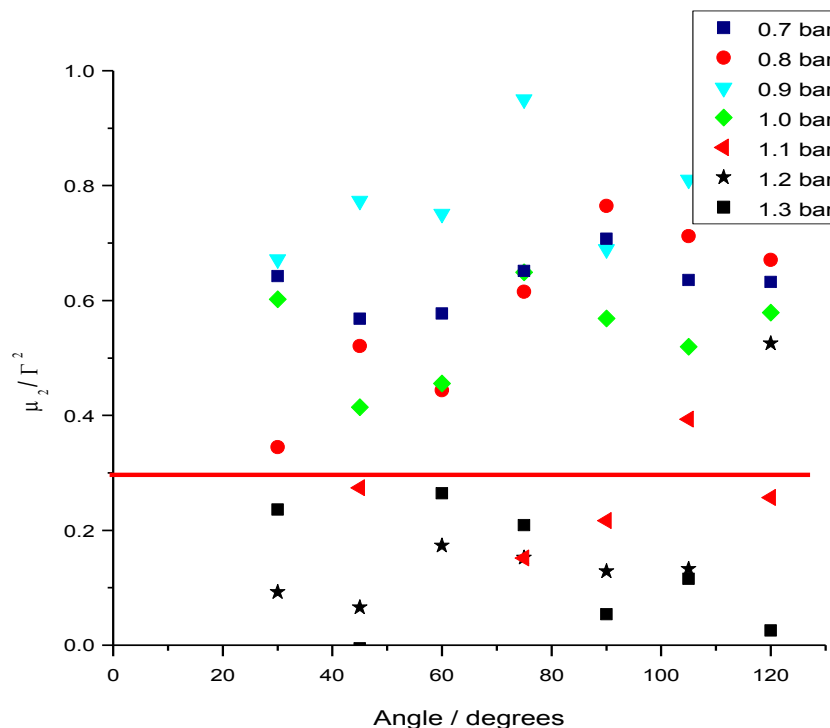


Figure 2.9. Dimensionless parameter $\frac{\mu_2}{\Gamma^2}$ vs. angle for $c=0.1$ mg/mL CU bubbles at different pressures. $\frac{\mu_2}{\Gamma^2} \geq 0.3$ (red line) signifies a large distribution or multi-component system, above which cumulant analysis is not recommended as the sole method to determine size distribution.

Because some of the measurements have high $\frac{\mu_2}{\Gamma^2}$ it is recommended to analyse the data with multi-exponential fitting and inverse Laplace transform methods. In the present fit, the multi-exponential fitting uses a two-exponential equation with five variables.

$$g^{(2)}(t) = B + \beta(A_1 e^{-\Gamma_1 t} + A_2 e^{-\Gamma_2 t})^2 \quad (18)$$

Multi-exponential fitting in Figure 2.10 shows the same trend of lower sizes at the increased pressures and higher radius at partial vacuums. The figure only shows the lower radius for each double exponential.

For solutions with increased pressures the second term in the two-exponential fit had negligible amplitude so the fit approximated to a single exponential. At atmospheric pressure and a partial vacuum, the second term was for a micron-sized scatterer. The solution has slow and fast decay modes representing the large micron bubbles and small submicron bubbles. According to the model from the SAXS fitting there is also a very fast decay from the free proteins in solution. This is not included because the scattering intensity of a single protein compared to a bubble is so large that it is masked out even after accounting for the number of free proteins in the solution. When a solution is agitated at increased pressures the large bubbles are not able to form and the system results in a single exponential decay for the submicron bubbles.

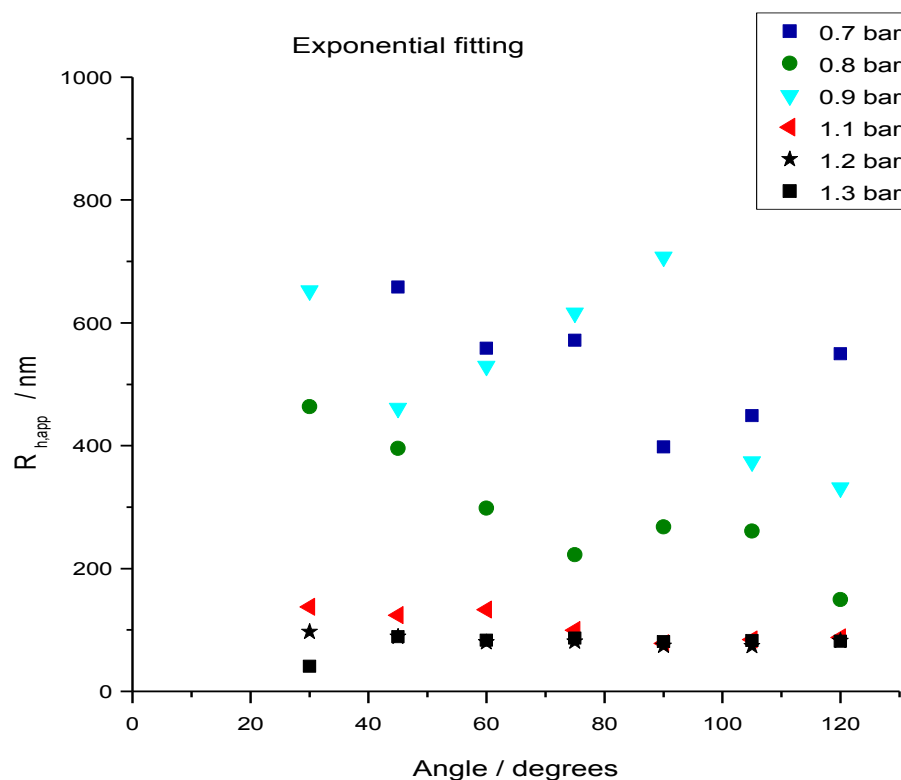


Figure 2.10. Multi-exponential analysis of dynamic light scattering of $c=0.1$ mg/mL CU agitated by hand at various pressures.

The CONTIN analysis (Figure 2.11 and Figure 2.12) shows the same overall trend as the cumulant and double exponential fitting, with higher radii at partial vacuums and smaller radii at increased pressures. The values are higher than cumulant and double exponential fitting. CONTIN use a Laplace inversion algorithm that use multiple grid points (may exceed a hundred) to estimate amplitudes for each decay rate Γ at each grid point. This creates an estimated size distribution of scatterers.

In the current system, exponential fitting supports the hypothesis that the solution contains a large amount of smaller bubbles with a small number of larger scattering bubbles

that skew the cumulant fit to a higher average value. An even larger number of individual proteins may yet be undetected. The residual plots in Figure 2.13. Residual plots for cumulant, exponential, and CONTIN fits for $c = 0.1$ mg/mL CU solution at $\theta=60$ degrees with pressure at 1.3 bar. show all three fits with random residuals.

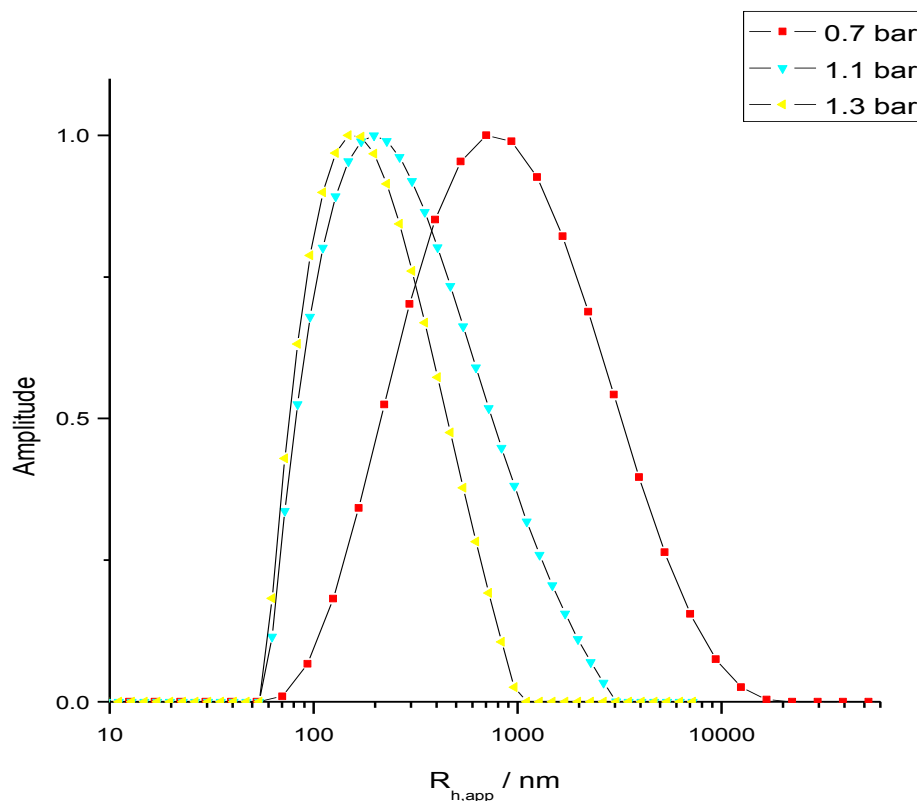


Figure 2.11. Amplitude versus apparent radius for CONTIN analysis of dynamic light scattering of $c = 0.1$ mg/mL cerato-ulmin agitated by hand at various pressures.

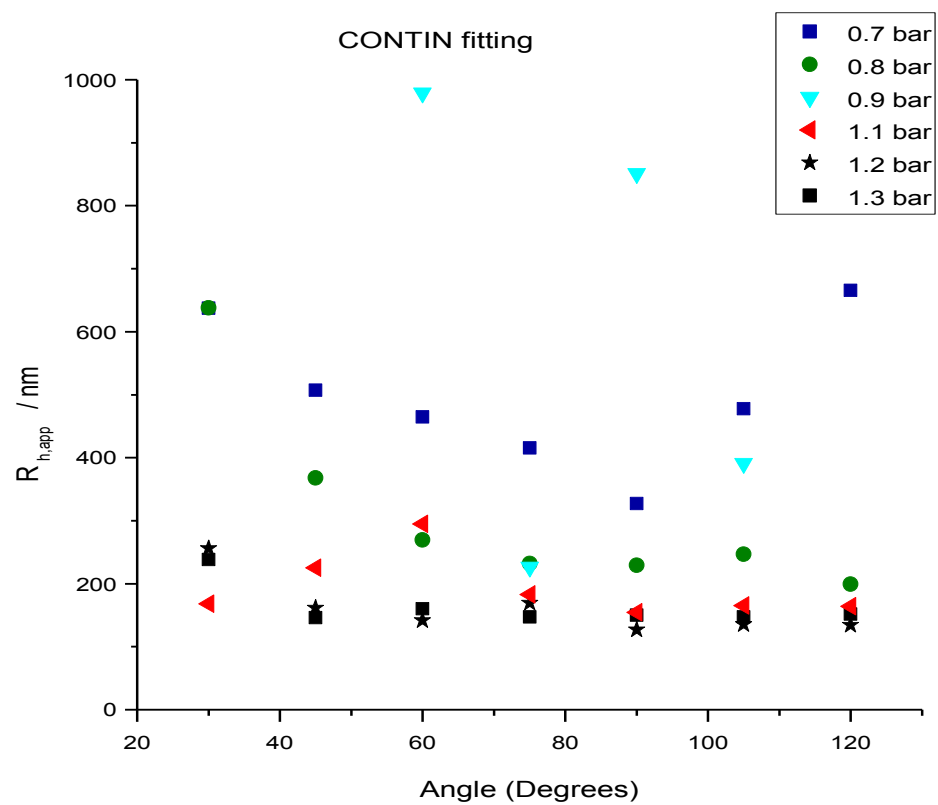


Figure 2.12. CONTIN analysis of dynamic light scattering of $c=0.1$ mg/mL CU agitated by hand at various pressures.

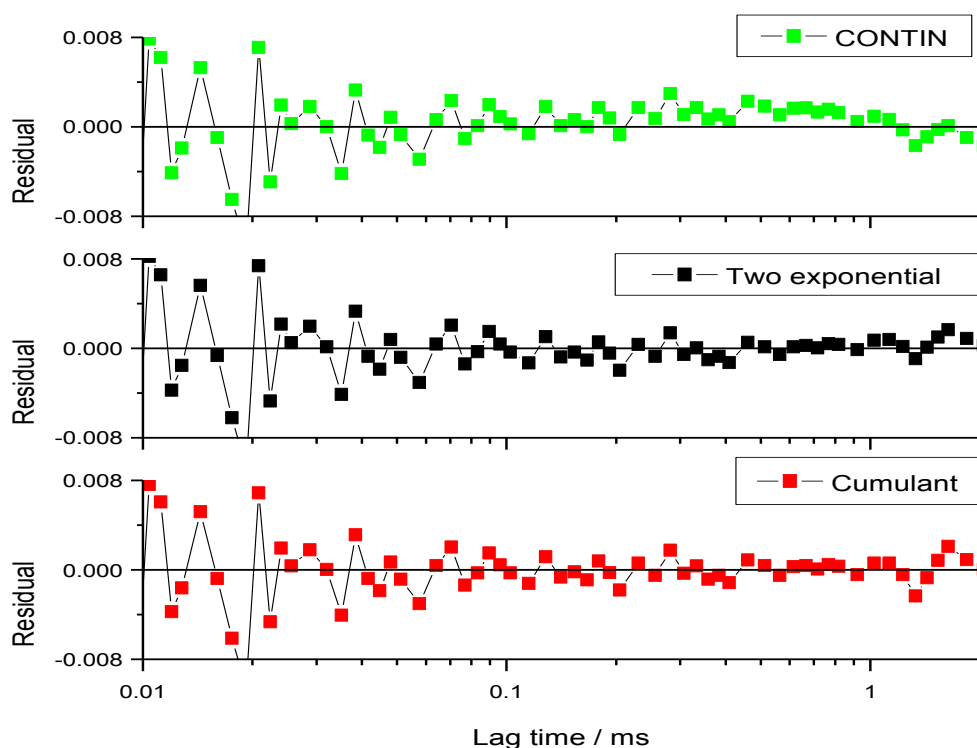


Figure 2.13. Residual plots for cumulant, exponential, and CONTIN fits for $c = 0.1$ mg/mL CU solution at $\theta=60$ degrees with pressure at 1.3 bar.

The results in Figure 2.14 are a summary of the pressure behavior of the CU bubbles. Each point is the zero-angle approximation of exponential fits at the seven angles for each pressure. When a solution is agitated at a partial vacuum, large bubbles form and are still in the scattering volume after one hour. The size distribution is much larger for partial vacuums because the decreased forces allow more sizes to develop as the solution is agitated by hand. For increased pressures the forces constrain the sizes and the bubbles are not only smaller but much more monodisperse.

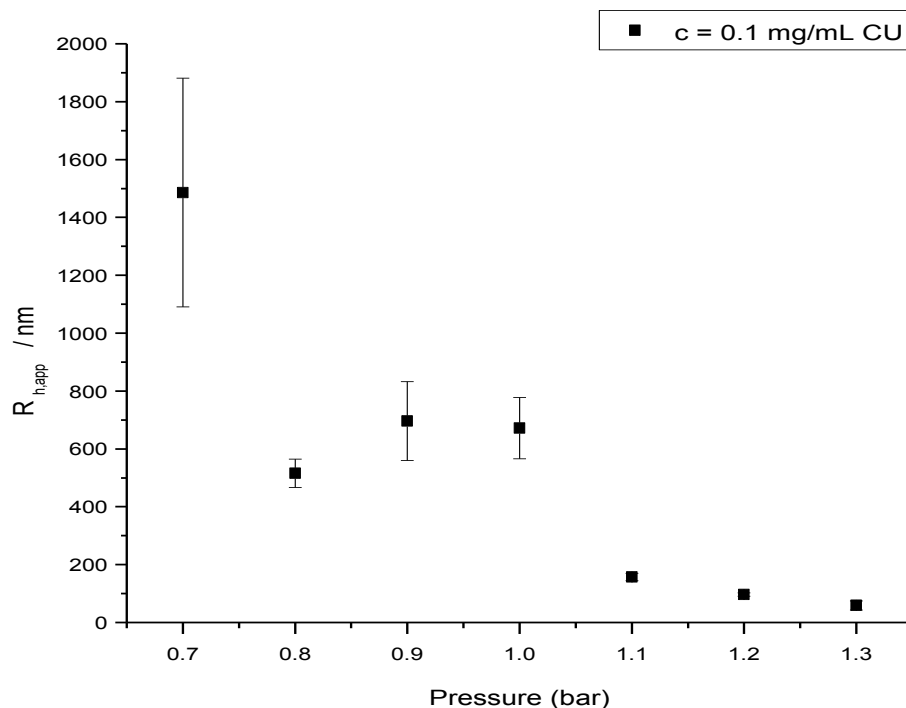


Figure 2.14. Radius versus pressure measurements with $c = 0.1$ mg/mL CU measured one hour after solution agitation. Each point is the zero-angle extrapolation from multiple DLS runs.

2.5 Dynamic Pressure Effects

2.5.1 Experimental Setup

DLS experiments were conducted on the same apparatus described earlier with the same preparation and procedure. Samples were connected to the syringe pump to create the desired pressure profiles. Between pressure change and measurement, a one-hour delay allowed the sample to equilibrate.

2.5.2 *Results*

While the static pressure experiment does support the hypothesis that the submicron scatterers are bubbles, it is not definitive. Other explanations could explain the experimental result. It is possible that the scattering particles are more likely to “clump” together when agitated at higher pressures and reduced pressures suppress the effect. For this reason, it is necessary to conduct additional experiments to test whether the submicron scatterers are also bubbles.

A dynamic pressure experiment will show if the scatterers change expand or contract with pressure changes once they are already formed. To further investigate, a cerato-ulmin solution was agitated by hand at atmospheric pressure and then subjected to overpressure and partial vacuum. After each pressure change the solution equilibrated for 1 hour. A syringe pump increased the pressure by 0.1 bar three times before returning to atmospheric conditions. Finally, a partial vacuum was created by the syringe pump and the pressure was decreased to 0.9 bar. The complete cycle is shown in Figure 2.15.

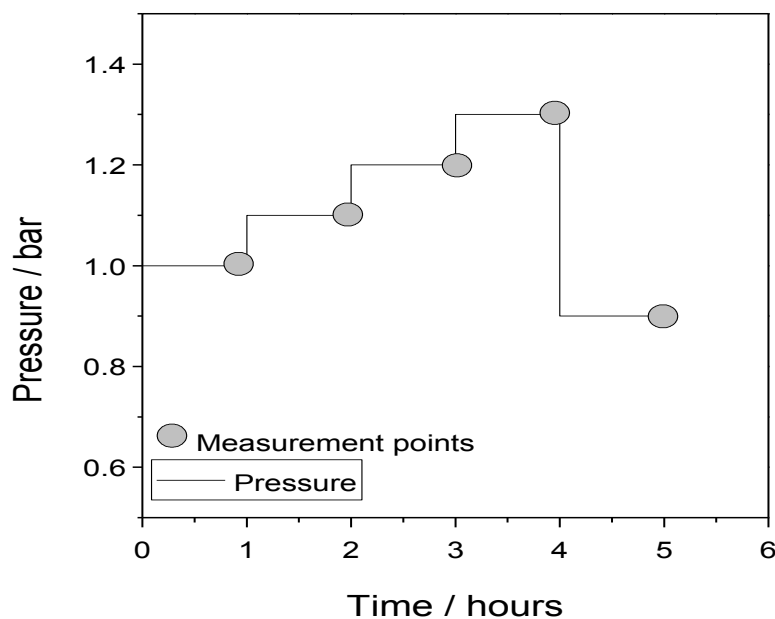


Figure 2.15. Measurement progression in dynamic pressure experiment. After each pressure change the sample equilibrated for 1 hour before measurements.

Each dataset was analyzed with cumulant, exponential, and CONTIN at scattering angles of 45, 60, 75, and 90 degrees. Spectra were collected at four angles and analyzed with cumulant, exponential, and CONTIN fitting. The log (Figure 2.16) and semi-log (Figure 2.17) normalized baseline-subtracted DLS correlation functions show clear changes at different pressures.

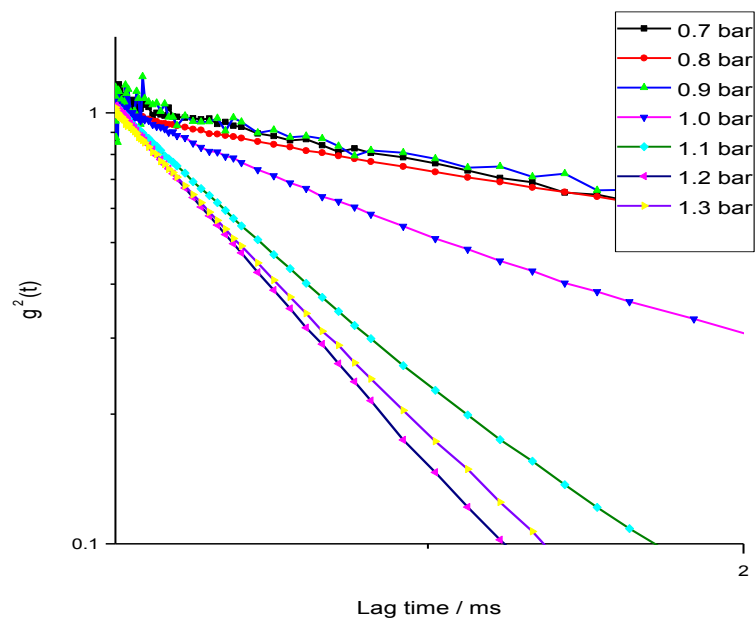


Figure 2.16. Normalized, baseline-subtracted DLS correlation functions in a semi-log plot measured at a scattering angle of 45° for cerato-ulmin solution ($c = 0.1$ mg/mL) at different pressures.

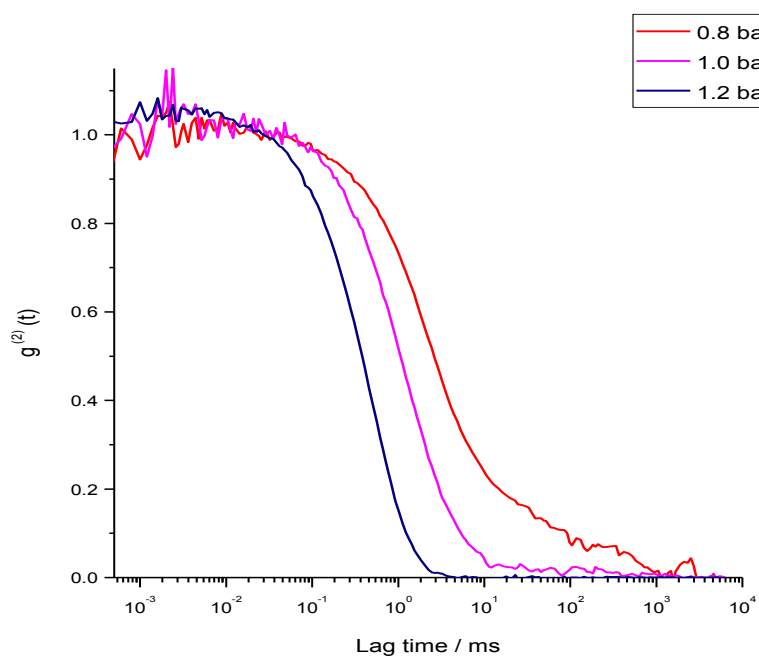


Figure 2.17. Normalized, baseline-subtracted DLS correlation functions measured at a scattering angle of 45° for cerato-ulmin solution ($c = 0.1$ mg/mL) during different points of the pressure cycle.

The calculated radii from cumulant analysis for all six runs are shown in Figure 2.18. It is arguably overwhelming to show this many data points on one plot when they are not well behaved, but it is worthwhile as there are broad insights available through a qualitative analysis.

First and foremost, there is a clear change in radii for bubbles at different points in the pressure cycle. The influence of pressure on radii is shown in the previous section but in that situation the pressure was set before bubble formation and was held constant. The static pressure experiment shows a pressure dependency during formation but does not yield any information on whether the bubbles continue to be pressure dependent or if dependency is only during formation. In this setup, bubbles are formed at ambient pressure before different pressures are applied. The change in size after pressure changes means that the bubble film is not a fully rigid film and has a dynamic response to pressure changes where increased pressures lead to smaller bubbles.

The effect of angle on measured radius also provides information about the bubble dispersion. For the lower pressures, there is a large degree of angle dependence suggesting that the dispersion is very polydisperse with a large range of bubble sizes. At higher pressures, this polydispersity is more muted as the pressure decreases the bubble size. Applying pressure does not shrink all bubbles equally though. It is likely that every pressure has a minimum bubble size where the forces reach equilibrium. Larger bubbles will shrink more and narrow the size distribution.

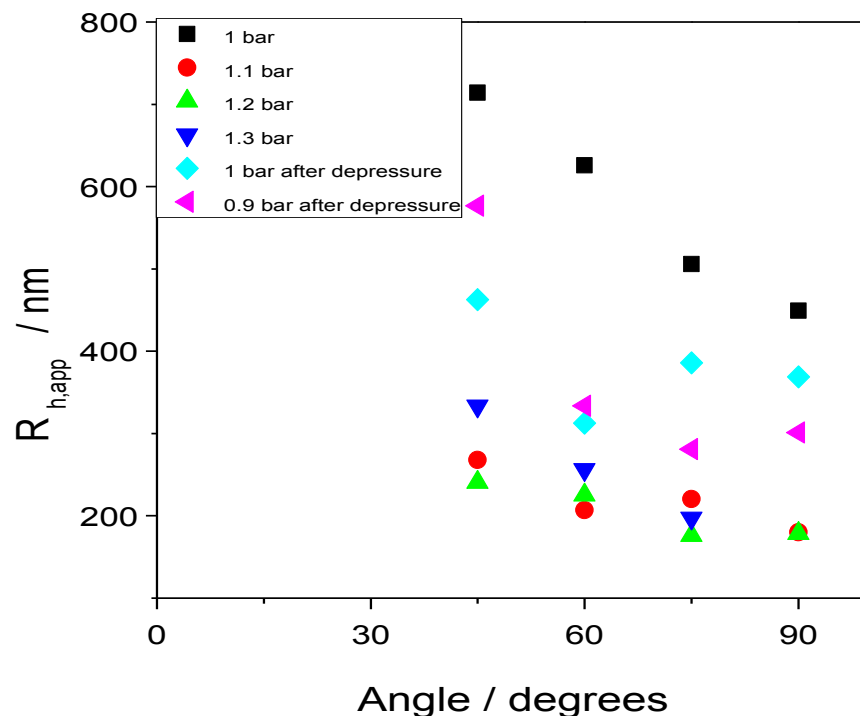


Figure 2.18. Cumulant analysis for dynamic pressure experiment of $c = 0.1$ mg/mL CU agitated solution.

As the cycle continues and the pressure returns to ambient or partial vacuum, the bubbles expand. At $P = 0.9$ bar, the bubbles have made a full recovery to their original size within error (Figure 2.19).

The zero-angle extrapolation of the cumulant fit results are displayed in Figure 2.19. The results show the decreasing size and polydispersity of the bubbles as pressure is increased to 1.1 and 1.2 bar. There is a possible unexpected bump in size at 1.3 bar but the uncertainty of the measurement was also high so it is unclear if it is real effect. As the pressure is reduced from 1.3 bar the bubbles increase in size and polydispersity.

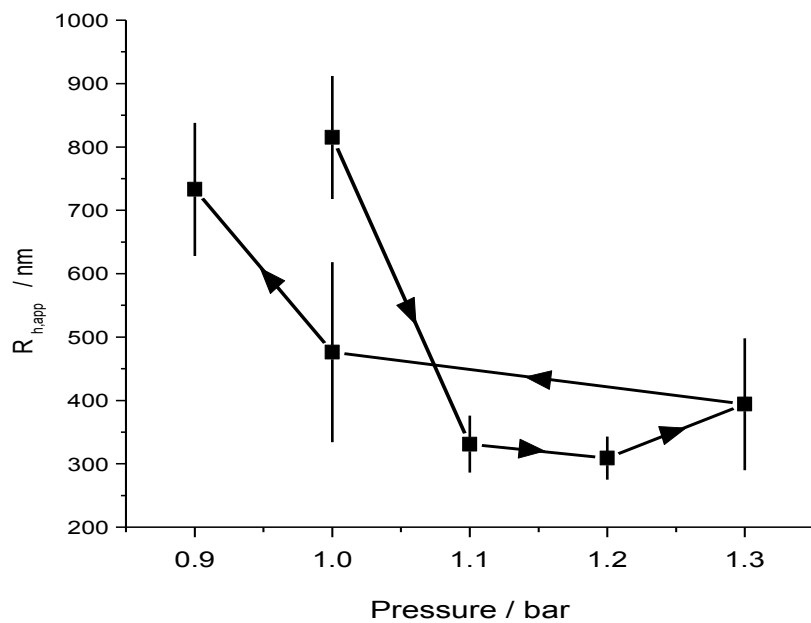


Figure 2.19. Zero-angle extrapolation of cumulant fitting for $c = 0.1 \text{ mg/mL}$ CU agitated solution during dynamic pressure cycle.

The dimensionless parameter $\frac{\mu_2}{r^2}$ is an indicator of the sample's suitability for cumulant analysis. As seen in Figure 2.20, the values are greater than $\frac{\mu_2}{r^2} > 0.3$ so multi-exponential fitting and CONTIN become feasible.

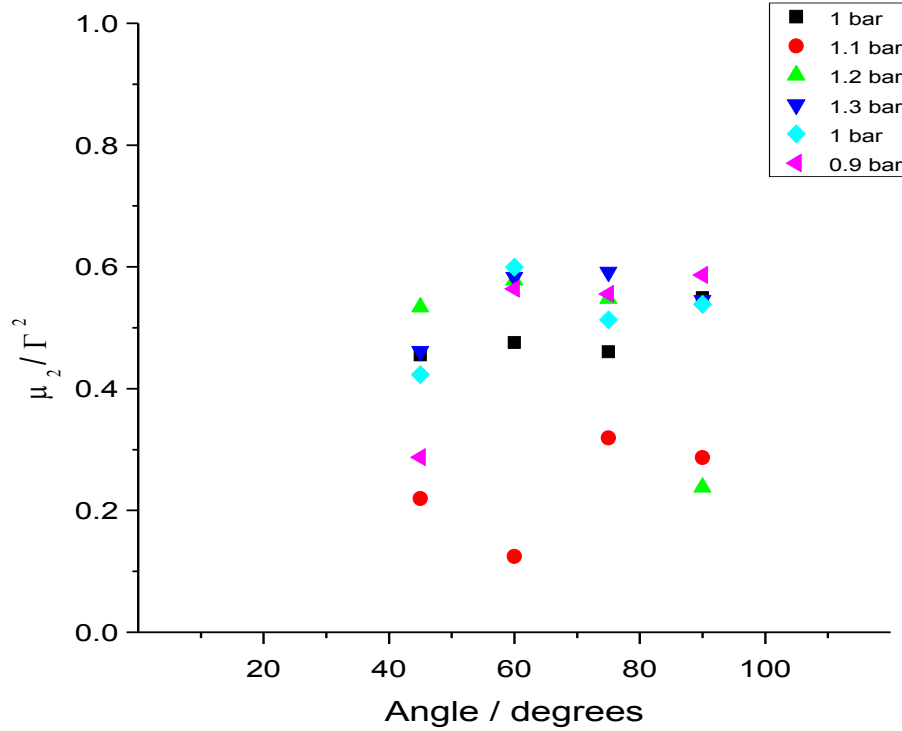


Figure 2.20. Dimensionless parameter $\frac{\mu_2}{\Gamma^2}$ vs. angle for $c = 0.1$ mg/mL CU bubbles at different points in the pressure cycle.

The next method to use is multi-exponential fitting. Functions were fit with a two-exponential fitting model for the same reasons as mentioned in the static pressure experiment section. After plotting all calculated radii in the same manner as Figure 2.18, the zero-angle extrapolation was calculated by linear fitting. The results in Figure 2.21 show the same general behavior suggested by the cumulant analysis. The bubbles size decreases with applied pressure before recovering as the pressure returns to atmosphere.

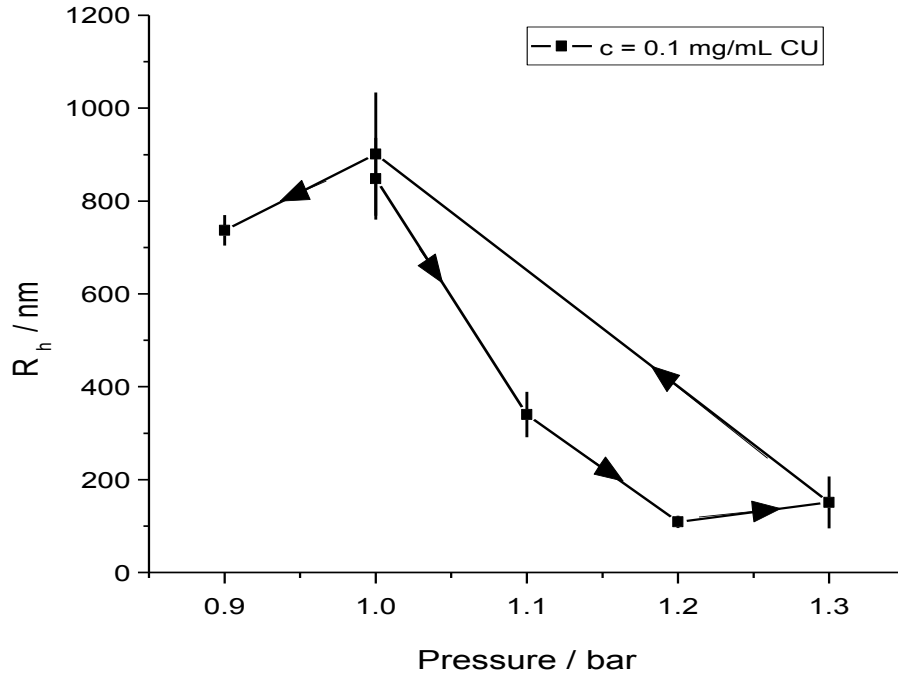


Figure 2.21. Zero-angle extrapolation of multi-exponential fitting for $c = 0.1$ mg/mL CU during dynamic pressure experiment.

Once again, there is an unexpected data point, this time at 0.9 bar. When a partial vacuum is applied the bubble size decreases which does not follow the current working hypothesis as bubbles increase in size with reduced pressures or partial vacuums. A closer look into the data of the individual exponential fits shows that the bubble sizes are larger at individual angles for 0.9 bar, but at $P = 1$ bar, data points have a much greater angle dependence which creates a larger radius for zero-angle extrapolation. As the pressure returns to 1 bar the solution has a large size polydispersity, but once a partial vacuum is applied the polydispersity shrinks. Most likely, this is due to a decreased population of smaller bubbles, either from dissolution or merging.

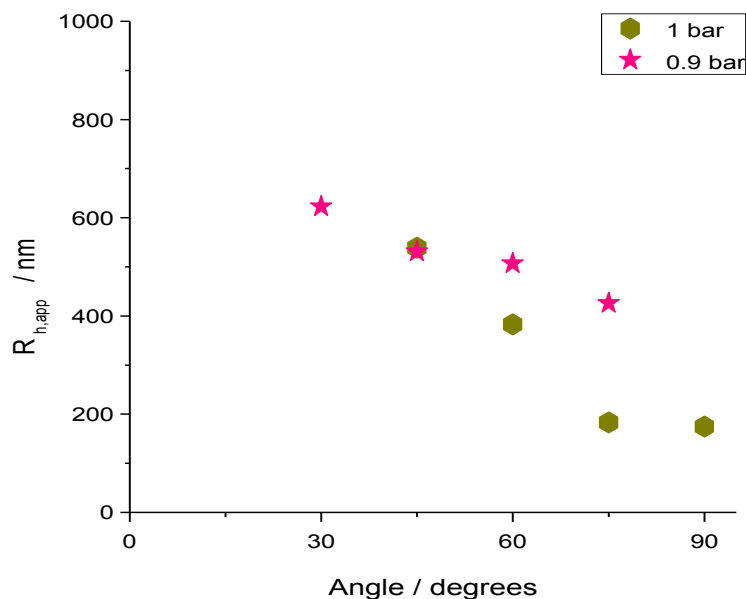


Figure 2.22. Apparent hydrodynamic radius measurements using exponential fitting of the last two pressure steps in the dynamic pressure cycle for $c = 0.1$ mg/mL CU solution. The measurement at $P = 0.9$ bar gave higher values but the high-angle dependence results in $P = 1.0$ bar having a greater R_h when performing a zero-angle extrapolation.

Because the changing pressures seem to have a large effect on polydispersity, it is easier to view the overall process by plotting the multi-exponential fitting results at one angle. Figure 2.23 shows the pressure experiment results at 45 degrees with the two-exponential fit. With increased pressure, the bubbles shrunk from 519 nm to 57 nm. Once the pressure was brought down to atmospheric pressure the bubbles partly recovered their size and increased to 229 nm before a further expansion to 531 nm in a partial vacuum of 0.9 bar.

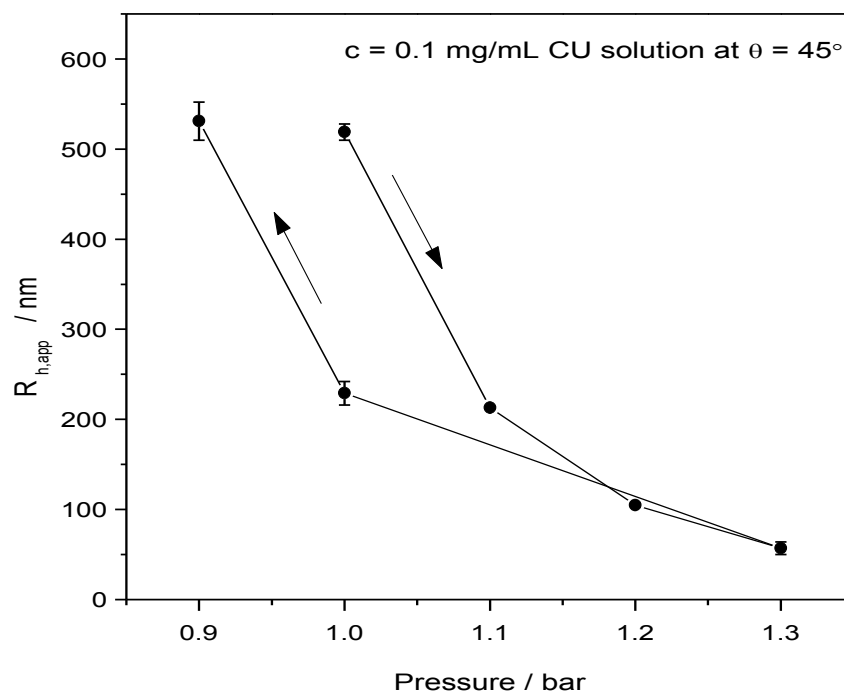


Figure 2.23. Multi-exponential fitting of cerato-ulmin bubbles shows a decrease in hydrodynamic radius as increased pressure is applied followed by an increase in radius as the pressure decreases and a partial vacuum is formed. The error bars are uncertainty in the fit, not a standard deviation of the measurement. Take with permission from reference 97.

CONTIN analysis is the most versatile fitting method compared to cumulant analysis and multi-exponential because the fit considers a continuum of scatterers, which is most accurate for the CU solution. Like the multi-exponential fitting, the best method to display the results is plotting the hydrodynamic radius against pressure at a single angle (Figure 2.24).

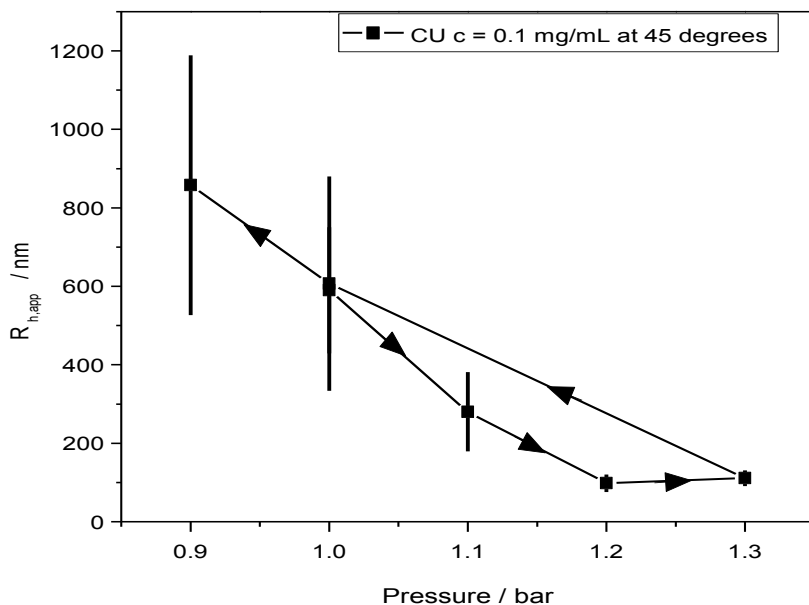


Figure 2.24. CONTIN analysis of $c = 0.1$ mg/mL CU at 45 degrees during a dynamic pressure cycle. The error bars are the standard deviation of the continuum of bubbles in solution.

As expected, the results show the same general behavior as suggested by the cumulant and multi-exponential analysis with the radius and polydispersity decreasing before recovering as pressure is returned to ambience and partial vacuum is applied. The hydrodynamic radius and standard deviation were calculated by fitting a Gaussian distribution to the amplitude versus radius curves seen in Figure 2.11 where the hydrodynamic radius R_h is the center of the peak and the standard deviation is the full width at half maximum (FWHM) divided by a factor of 2.355.

The measured size recovery with CONTIN follows the same pattern as the cumulant and multi-exponential results. All fits show a complete size recovery to this

degree with a partial vacuum. These results suggest a recovery behavior and expansion with partial vacuum that are consistent with the behavior of bubbles on all length scales.

As previously mentioned, cumulant analysis suffers from diminishing accuracy with polydispersity and the multi-exponential fit assumes multiple monodisperse scatterers. The CU solution is a bubble dispersion with both a high size and shape polydispersity resulting in a range of diffusion rates. For such a system CONTIN will be the most accurate as it fits a range of decay rates with different amplitudes.

Figure 2.25 shows the evolution of the hydrodynamic radius R_h as the solution pressure changes for all three fitting methods. For all methods the results show the same general behavior: a decreasing size as the pressure increases followed by recovery. These results strongly suggest the scatterers are submicron bubbles.

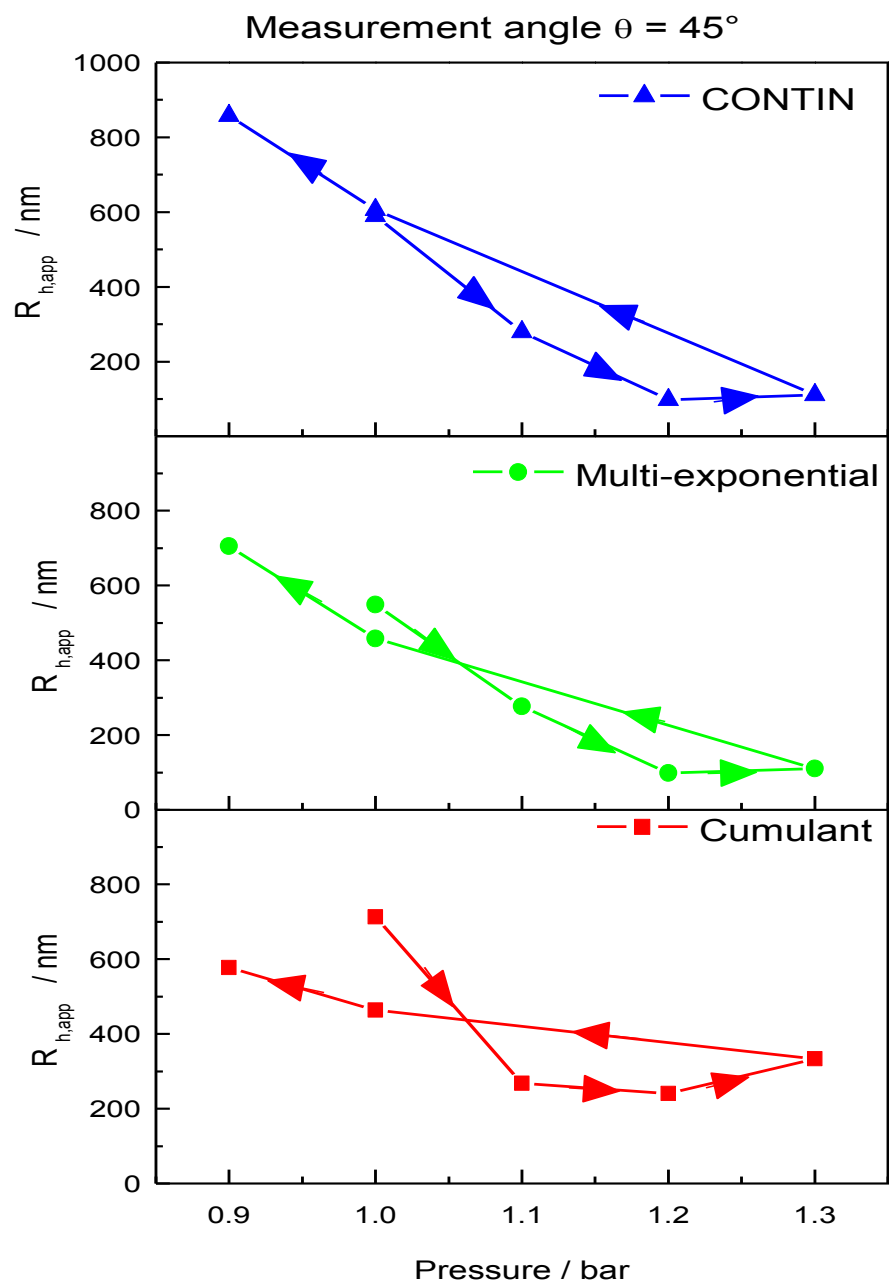


Figure 2.25. Dynamic pressure experiment results using CONTIN, multi-exponential, and cumulant fitting of $c = 0.1 \text{ mg/mL}$ CU measured at 45° .

2.6 Conclusions

When an aqueous solution of CU is gently agitated, it creates a spectrum of bubbles ranging from $10^{-7} - 10^{-3}$ m. The existence of the larger bubbles was previously known through optical microscopy, but the submicron bubbles were only suspected. Pressure experiments, both static and dynamic, show the structures to behave consistent with bubble response to pressure changes and inconsistent with other possible structures such as a solid or aggregate. Agitating a CU solution at different pressures created larger or smaller bubbles when a negative or positive pressure is applied. When the CU solution underwent a pressure cycle, the bubbles also changed in size, demonstrating their response behavior. As these results are incongruous with solid structures or aggregates, the conclusion is that the CU forms submicron as well as microbubbles.

CHAPTER 3. STRUCTURAL CHARACTERISTICS OF CERATO-ULMIN IN MICRO AND SUBMICRON BUBBLES IN AN AQUEOUS SOLUTION

3.1 Introduction

The strong amphipathic nature of CU creates interesting phenomena warranting further investigation. When an aqueous solution of CU is gently agitated, it forms nonspherical bubbles on a microscopic and submicron scale (Figure 2.6). These bubble films are both robust and are capable of forming at concentrations as low as the $\mu\text{g/mL}$ scale.¹⁰⁶ The reason for CU's preference for nonspherical bubbles is not fully understood. Probing the structure of the film may provide clues to the behavior of the bubbles.

Experiments were selected to gain a better understanding of the structure. Optical microscopy in conjunction with volumetric considerations provided a rough estimate of the bubble film thickness and number of proteins. Because this required a significant number of assumptions, more precise experiments became necessary to gain certainty.

Small-angle neutron scattering provided possible structures of the CU protein in the bubble film and free solution. The scattering data were fit with *ab-initio* modeling from the Svergun¹⁰⁷⁻¹¹⁷ suite of programs to create a visual recreation of the protein structure. Building on these results, solution small-angle x-ray scattering was completed to examine the overall structure of the bubble. Using particle form factors, it was confirmed that the submicron bubbles were also cylindrical, permitting estimation of their dimensions; then

the SANS results were used to estimate the number of protein molecules needed to create the bubble thickness. Finally, atomic force microscopy (AFM) verified these results by measuring collapsed bubbles. Assuming the collapsed bubbles were simply the two films resting upon each other, the height from AFM results would be twice the bubble thickness. The SAXS and AFM experiments are published results in the *Journal of Physical Chemistry B*.⁹⁷

3.2 Optical Microscopy

3.2.1 Experimental Setup

A sample of 0.1 mg/mL cerato-ulmin was gently agitated by hand through a rocking motion in a rectangular glass vial supplied by VitroCom Inc. The sample was observed with a Leica DMR optical microscope equipped with a Canon EOS6D digital camera (5472×3648 pixels).

3.3 Small-Angle Scattering

3.3.1 General Scattering

Scattering is the deflection of electromagnetic radiation or particles from their original trajectories due to inhomogeneity of a material in the incident path. The scattered radiation or particles can have the same energy as the incident beam (elastic) or a different amount (inelastic). Scattering is one of the most useful phenomena for materials scientists. Using the multiple scattering techniques available can provide scientists with the size, shape, and structure of materials. For light and X-ray scattering, incident photons interact with the electron cloud of an atom to create a dipole that emits a photon. Neutron scattering

is the result of neutrons interacting with the nucleus of atoms or the magnetic moment of electrons.

A typical scattering result consists of intensity as a function of the scattering vector $q = \frac{4\pi \sin \theta}{\lambda}$ where 2θ is the angle between the incident and scattered directions and λ is the incident wavelength. All elements have an x-ray and neutron scattering cross section that describes the relative likelihood of scattering an incident particle or wave. The cross section, b , of each element is combined to form the scattering length density of the material, $\rho = \frac{\sum_i^N b_i}{V_m}$ where V_m is the volume of the scattering material. The intensity is also affected by the angle, concentration, composition, size, and shape of the scattering objects.

X-ray instruments are identified by the angles they probe: wide (WAXS), middle (MAXS), small (SAXS), and ultra-small (USAXS). To detect a signal at small-angles without interference from the incident beam, instruments are constructed to have a large distance between the sample and detector. Neutron scattering typically uses small and ultra-small scattering.

3.3.2 *Small-angle Scattering Theory*

The derivation of total scattered intensity from the scattering amplitude of a single scattering center is found in Guinier's work.¹¹⁸ The scattering amplitude from a single atom is defined by

$$A_k = A_e f_k e^{-i\vec{q} \cdot \vec{r}_k} \quad (19)$$

where A_e is the amplitude scattered by one electron and f_k is the number of electrons in the k^{th} atom, \vec{q} is the scattering vector, and \vec{r}_k is the vector between the origin and point M_k (Figure 3.1). Commonly the scattering unit vector, \vec{q} , is defined $\vec{q} = \frac{2\pi}{\lambda}(\vec{k}_s - \vec{k}_i)$ with a magnitude of $q = \frac{4\pi \sin \theta}{\lambda}$. The vectors \vec{k}_s and \vec{k}_i are unit vectors in the direction of the scattering and incident radiation, respectively. The q -vector is also related to the distance scale being probed by the relation $q = \frac{2\pi}{d}$. This distance scale d is referred to as the characteristic length and is considered the size range that is being examined. For example, examining features that are on the order of 5-10 nm will be impossible to characterize if the scattering q -range relates to characteristic lengths of 50-100 nm. Choosing the correct q -range for experiments is crucial and experimental beam lines have only a limited flexibility to change it.

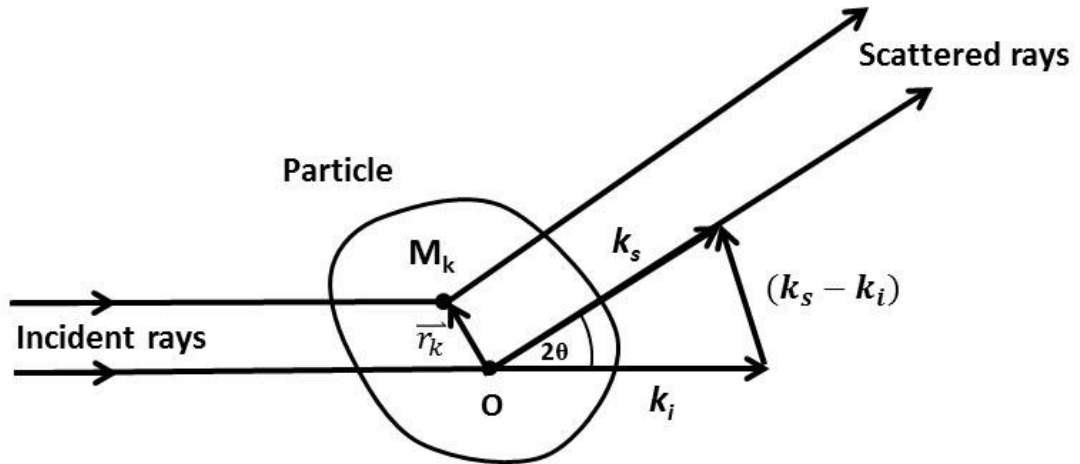


Figure 3.1. Schematic of the scattering of a single particle. Adapted from reference 118.

For a particle, the total scattered electric field will be the summation from all the contributing scattering centers

$$A(\vec{q}) = \sum_k A_k = A_e(q) \sum_k f_k e^{-i\vec{q} \cdot \vec{r}_k} \quad (20)$$

where \vec{r}_k is the vector between points O and M_k . By multiplying $A(\vec{q})$ by its complex conjugate $A(\vec{q})^*$, the intensity of the scattering is

$$I(q) = A_e^2(\vec{q}) \sum_k \sum_j f_k f_j \cos(\vec{q} \cdot \overrightarrow{r_{kj}}) \quad (21)$$

Defining the form factor as “the ratio of the total scattered amplitude to the amplitude of radiation scattered by one electron under the same conditions”¹¹⁸

$$F(\vec{q}) = \frac{\sum_k A_k(\vec{q})}{A_e(\vec{q})} = \sum_k \cos(\vec{q} \cdot \vec{r}_k) \quad (22)$$

the scattering intensity is

$$I(\vec{q}) = I_e(\vec{q})P(\vec{q}) \quad (23)$$

where $P(\vec{q})$ is the intensity form factor $P(\vec{q}) = F^2(q)$ and $I_e(\vec{q})$ is the scattering intensity of a single electron $I_e(\vec{q}) = A_e^2(\vec{q})$.

Samples in small-angle scattering are frequently in a solution, gel, or emulsion that allows free movement of the particles. To account for movement, a translation and rotation component needs to be added to the form factor. For translation described by vector V , a

factor of $e^{-iq \cdot \vec{r}}$ is cancelled when the amplitude is multiplied by its complex conjugate.

The rotation though is not cancelled out but if the particle is centrosymmetric and has equal probability of all orientations

$$\overline{F(\vec{q})} = \sum_k f_k \overline{\cos(\vec{q} \cdot \vec{r}_k)} \quad (24)$$

where \vec{r}_k is the distance from the origin to the scatterer or $\overrightarrow{OM_k}$. Calculating the average orientation of the particle

$$\overline{\cos(\vec{q} \cdot \vec{r})} = \int_0^\pi \cos(qr \cos \theta) \frac{\sin \theta}{2} d\theta = \frac{\sin qr}{qr} \quad (25)$$

The scattering factor f_k for a single atom is constant over the q -range of small-angle x-ray scattering; this allows for the scattering factor to be considered as the electronic density over a small volume area $f_k = \rho_k dv_k$.

The final identity is

$$\overline{P(\vec{q})} = \int \rho_k \frac{\sin qr}{qr} dv_k \quad (26)$$

and the overall scattering for a freely moving particle is

$$I(q) = I_e(q) \int_V \rho(r) \frac{\sin(qr)}{qr} dV \quad (27)$$

3.3.3 Solution Scattering

Solution scattering has been a valuable characterization tool for particle systems in solution.¹¹⁹ For an ensemble of particles, the scattering intensity is

$$I(q) = N_p V_p^2 \Delta\rho^2 S(q) P(q) + \text{Background} \quad (28)$$

where N_p is the number of particles, V_p is the volume of the scatterer, $\Delta\rho$ is the difference in scattering length density between the scatterer and solvent, $S(q)$ is the structure factor, and $P(q)$ is the particle form factor. The structure factor $S(q)$ relates to the inter-particle distance and for dilute systems $S(q) = 1$. Because N_p , V_p , $S(q)$, and $\Delta\rho$ are constants, the intensity in solution scattering is simplified to $I(q) \propto P(q)$. The form factor contains four scattering regions that describe the particle's size, shape, and surface. At low q the scattering is in the Guinier region and relates to the overall size of the particle. This region is sometimes isolated and graphed as the natural logarithm of intensity with the square of q in a Guinier plot. This plots the data according to the Guinier approximation

$$\ln(I(q)) = \ln(I_0) - \frac{q^2 R_g^2}{3} \quad (29)$$

where R_g is the particle's radius of gyration. This measurement is not related to a distance relating to the motion of the particle. It is the root mean square of the distance between all sub-units of the particle. If the plot is $\ln(q)$ versus q^2 , the data will be a straight line with a slope related R_g up to a certain q . The linearity begins to diverge at $qR_g > 1$ but depending on the scatterer the divergence progresses at different rates. The Guinier region is typically at low q and measures the R_g of the entire scatterer.

Strictly speaking, there is not just one Guinier region for a single scattering system. For example, a solution with multiple components or particles that aggregate into superstructures may contain multiple Guinier regions at different length scales.¹²⁰ A composite particle with subunits also may contain multiple Guinier regions.¹²¹ These systems pose a much greater challenge to model.

The second region of the form factor is the Fourier region. This part of the plot relates to the shape or cross section of the particle. For monodisperse, single-component samples the plots of the form factor can be easily modeled to determine the type of scatterer and its size. For polydisperse samples with varying size and/or shape, modeling becomes more difficult as features are completely or partially smoothed out as the pattern becomes the summation of multiple form factors.

The final part of the form factor is the Porod region at the high q . The intensity in the Porod region can be expressed as

$$I(q) = \frac{A}{q^n} + B \quad (30)$$

where A and B are constants, and n is the fractal dimension which gives some information about the shape of the scatterers (Figure 3.2).

Theoretically all scattering will eventually fall off at q^{-4} as the q range begins to probe the individual atoms that are best described as spherical. This may not always be the case because experimental constraints such as background contributions may obscure this behavior.

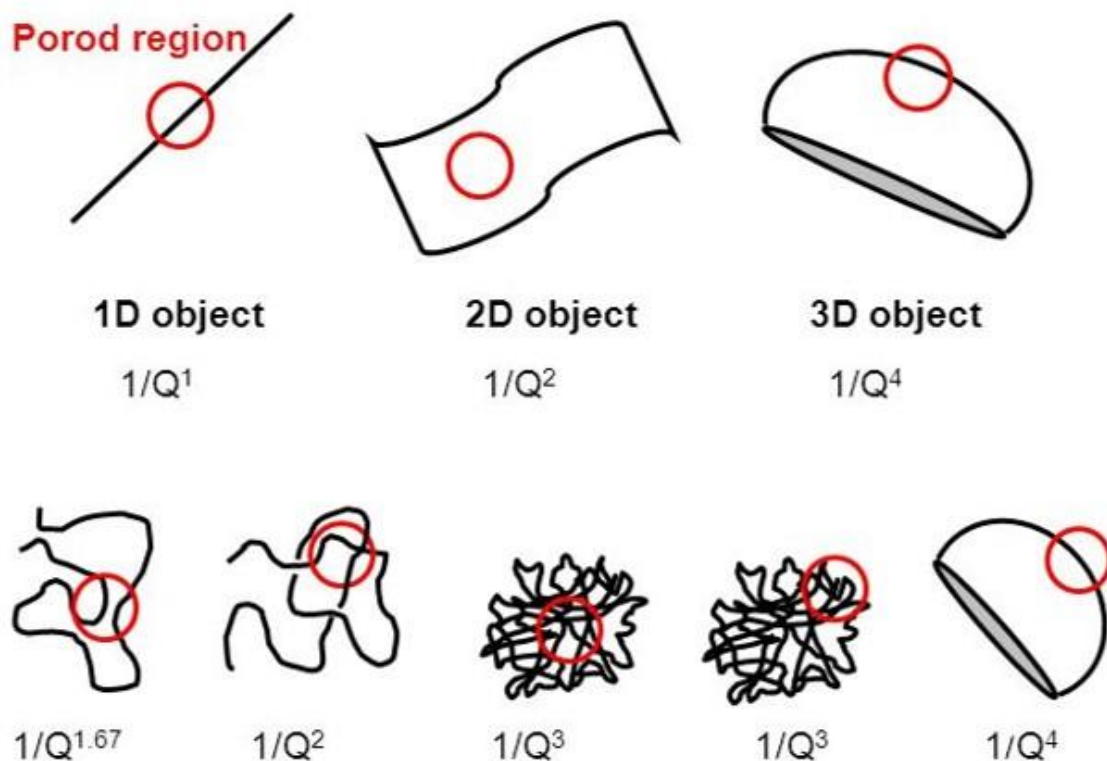


Figure 3.2. The power law for various mass and surface fractals in the Porod region. Intensity decreases according to the sample morphology and the length scale being probed. The size of the red circle represents the characteristic length d where $q=2\pi/d$. Take with permission from reference 122.

Even though samples contain Guinier, Fourier, and Porod regions the locations may not be clear-cut. In many samples, the Guinier, Fourier, and Porod regions are distinct. A sample may have components of different sizes. Therefore, the Guinier, Fourier, and Porod plots may overlap so the intensity at a given q value could be the combination of the Guinier behavior of one component and the Fourier behavior for another.

Even for single-component systems, the scattering may not be straightforward. For example, the CU bubbles form from smaller proteins self-assembling into the larger structure. The scattering pattern therefore could show multiple Guinier regions, and

corresponding apparent R_g values, as different length scales are probed. The radius of the bubbles, their cross-sectional radii, and the radius of the protein all contribute to the scattering signal, but the inverse problem of going from the measured signal to these parameters is not simple.

3.3.4 *Data Analysis*

One of the key challenges in scattering is the phase problem. The scattered radiation contains information about the particle or structure in the amplitude and phase of its electric field. Typically, experiments use detectors that only measure intensity, which is the multiplication of the amplitude and its conjugate. The multiplication cancels the phase and the information is lost. The main methods to recover the lost phase are multi-wavelength anomalous dispersion (MAD), single-wavelength anomalous dispersion (SAD), molecular replacement (MR), and multiple isomorphous replacement (MIR), but these techniques are not applicable in all cases and have limitations.¹²³⁻¹²⁶ MAD requires a tunable wavelength at a synchrotron, SAD requires “extremely high data quality”¹²⁷, MR only works for proteins and relies on a previously solved protein, and MIR adds ions to the protein cell structure.

The relations between the amplitude and intensity can be summarized in the magic square of scattering shown in Figure 3.3.

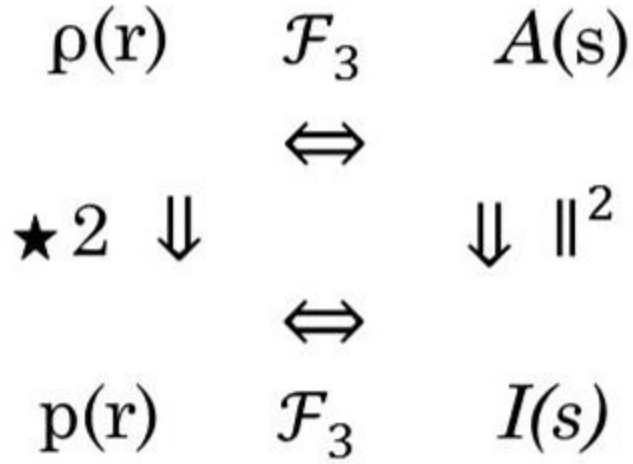


Figure 3.3. The relationships between the electron density difference $\rho(r)$, amplitude $A(s)$, pair-distance distribution function $p(r)$, and intensity $I(s)$ is commonly presented as the magic square of scattering. Adapted from reference 128.

The bottom right corner represents the scattering intensity that is measured during the experiment. Because the phase information is lost while squaring the amplitude (\parallel^2), it is not possible to use the intensity pattern to find $A(s)$. The only identity available is the PDDF, which is the 3D inverse Fourier transform of $I(s)$.

In the upper right is the amplitude of the scattered radiation in terms of the s -vector. The relationship between the q and s vectors, $q = 2\pi s$, is simply to make the relationship between $\rho(r)$ and $A(s)$ exact inverse Fourier transforms of one another. This allows for the direct conversion between the identities with a 3D Fourier transform \mathcal{F}_3 .

Moving to the bottom left, $p(r)$ is the pair distance distribution function (PDDF). This is a convolution ($\star 2$) of the electron density difference distribution with itself. The values of the PDDF are finite, positive values from $r = 0$ to the maximum diameter of the

particle, after which the values are all zero. Along with estimating the maximum diameter of the particle, the PDDF also sheds light on the particle shape as conformational changes in a particle create new PDDF patterns (Figure 3.4).

Finally at the top left is $\rho(r)$, the electron density difference distribution. Here, the formalism for SAXS is chosen, hence electron density. This represents the sample in real space and provides the size, shape, and content of the sample being probed. It is the most valuable corner as it allows for a complete reconstruction of sample in physical space.

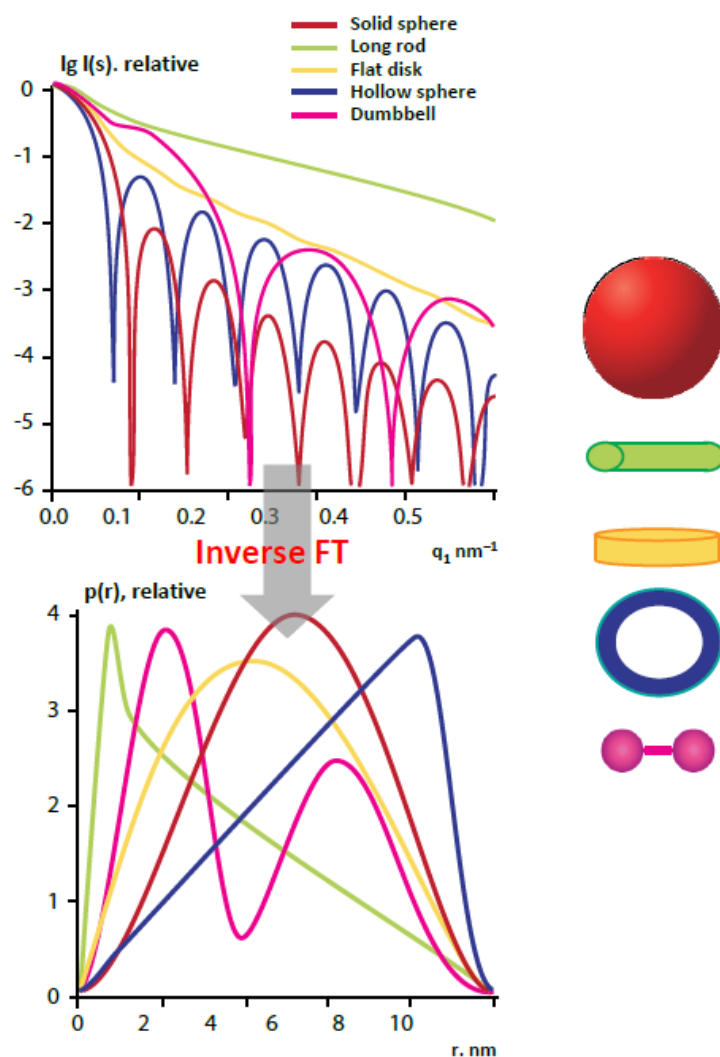


Figure 3.4. SAXS intensity (top) is converted to a PDDF (bottom) through an inverse Fourier transform. Taken with permission from reference 129.

One method for finding shape information from scattering data is *ab-initio* modeling. Beginning with the physical representation of a particle $\rho(r)$, one calculates its expected intensity and compares it to the experimental data. One common method is using the dummy atom model minimization routine DAMMIF from the ATSAS suite of programs developed by Svergun et. al.^{112, 130} The DAMMIF program matches the

experimental data with simulated intensity data from different shapes to find the best fit (Figure 3.5).

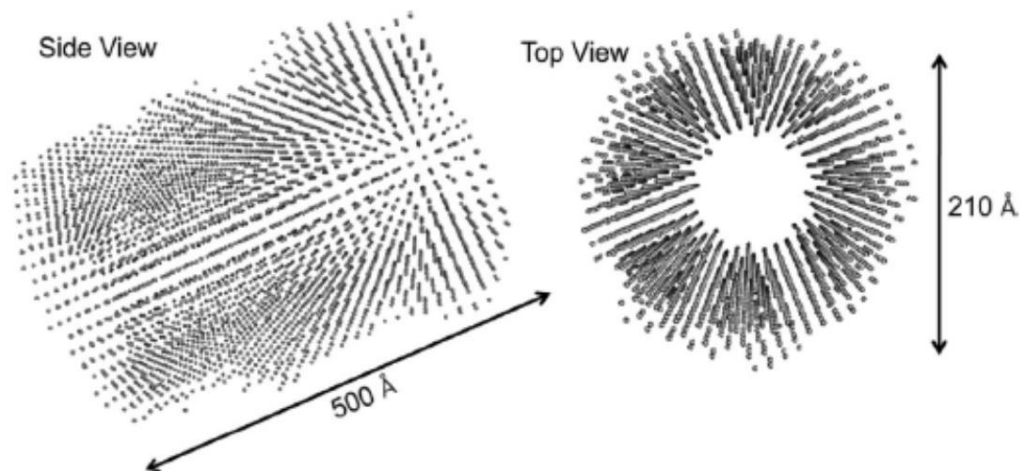


Figure 3.5. DAMMIF model for *meso*-tetra(4-sulfonatophenyl)-porphyrin (H₂TPPS⁴⁻) from synchrotron beamline. Take with permission from reference 119.

The intensity function for the dummy model is

$$I(s) = \left\langle \left[\sum_{k=1}^K \Delta\rho_k A_k(s) \right]^2 \right\rangle_{\Omega} \quad (31)$$

where $\Delta\rho_k$ is the phase difference between dummy atoms, $A_k(s)$ is the scattering electric field amplitude, and $\langle \dots \rangle_{\Omega}$ signifies the average over all orientations. For most calculations there is a binary of zero or one for the phase of the solvent or sample.

Comparing this to the experimental intensity we define a chi-square or goodness-of-fit parameter χ^2 as

$$\chi^2 = \frac{1}{M} \sum_{i=1}^M \sum_{j=1}^{N(i)} \left[\frac{I_{exp}^{(i)}(s_j) - I^{(i)}(s_j)}{\sigma(s_j)} \right]^2 \quad (32)$$

where M is the number of experimental curves, N is the number of points in the curve, $I_{exp}^{(i)}$ is the intensity of the experimental scatter data; $I^{(i)}$ is the simulated intensity, and $\sigma(s)$ is experimental uncertainty. By changing the dummy atom model to minimize χ^2 a likely shape of the particle will emerge.

The minimization procedure for χ^2 starts by computing χ^2 from a random configuration, changing one dummy atom and computing $\chi^{2'}$. If $\chi^{2'} < \chi^2$, the program will replace χ^2 and the process repeats. If not, χ^2 does not change and the model has one more dummy atom randomly change. By cycling through this process many times, a local minimum χ^2 is reached, and a possible shape of the particle is revealed.

Only minimizing χ^2 leads to subpar results because the minimization procedure does not consider that some dummy atom model (DAM) configurations are physically implausible, such as two sections separated by a single strand of atoms. DAMMIF also does not allow for a wide search area as all computed $\chi^{2'} > \chi^2$ are immediately thrown out. This means that if the program found a local minimum, there is no chance that it could move on to find the global minimum. DAMMIF addresses these issues by introducing a looseness penalty and simulated annealing.

The looseness penalty helps prevent the algorithm from resting in a minimum with a highly unlikely physical representation; i.e., two sections connected by a single strand of atoms.

The DAM model uses hexagonally packed atoms so the maximum number of connected atoms is $N_{e,max} = 12$. By defining N_e as the actual number of connected atoms of the same phase, we measure the extent of connectivity. For example, $N_e = 12$ means the dummy atom is inside the particle while $N_e = 0$ signifies that the dummy atom is surrounded by the solvent. Using the equation

$$C(N_e) = 1 - \left[e^{\frac{-N_e}{2}} - e^{\frac{-N_c}{2}} \right] \quad (33)$$

creates a decay as the number of connected atoms decreases. The exponential slowly decays down to $N_e = 6$ which could represent a dummy atom at the interface of the particle. For $N_e < 6$ the connectivity sharply decreases (Figure 3.6). At the lowest value of connected atoms, $C(0) = 0.002$ which shows that a dummy atom completely surrounded by solvent is a negligible event as it has no physical basis.

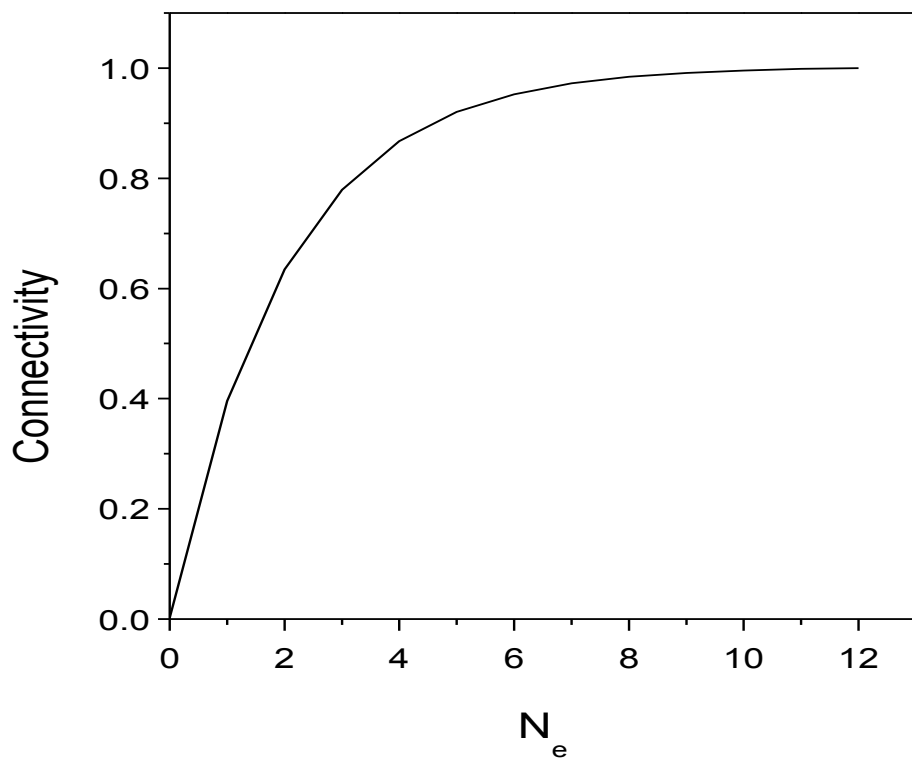


Figure 3.6. The connectivity parameter in the DAMMIF program describes the compactness of a system.

The overall compactness of the system can be expressed as the average connectivity of all the dummy atoms $\langle C(N_e) \rangle$. This allows for the average looseness of the configuration

$$P(X) = 1 - \langle C(N_e) \rangle \quad (34)$$

To help address the issue of getting stuck in a local minimum, DAMMIF also takes advantage of simulated annealing.¹³¹ This method to find the global minimum of $f(x)$ uses temperature as an energy concept of how willing the algorithm is to accept a configuration where $f(x) < f'(x)$. When the algorithm begins, the temperature is high so there is enough

energy to accept $f(x) < f'(x)$ and the configuration seems to move randomly. As the system is cooled, the algorithm is less likely to accept $f(x) < f'(x)$ so the system eventually finds the minimum. This method helps prevent the configuration from becoming trapped in a local minimum but still cannot fully guarantee that it arrives at the global minimum.

Combining these two concepts, the basic protocol of DAMMIF is to minimize the equation

$$f(X) = \chi^2 + \alpha P(X) \quad (35)$$

where α is the weight of the looseness penalty. The process is as follows:

1. Begin with a random configuration of dummy atoms X_0 and a high temperature T_0 .
2. Select an atom at random and change its phase to create configuration X' and compute $\Delta = f(X') - f(X)$.
3. If $\Delta < 0$, change the configuration to X' . If $\Delta > 0$, change the configuration with a probability of $e^{-\frac{\Delta}{T}}$.
4. Keep the simulation at a constant T for $100N$ reconfigurations or $10N$ successful reconfigurations, whichever comes first. After this, cool the system by $T' = 0.9T$.
5. Cool T until there is no further improvement in $f(X)$.

While the DAMMIF program is undoubtedly useful, there are two potential pitfalls. The algorithm will always find a minimum that will fit the data very close to perfectly even if an incorrect or nonsensical PDDF equation is input. This sometimes leads researchers

astray as they assume that such a good fit signifies a robust model. The second issue is the false minima. The program attempts to find the global minimum but even with the addition of the looseness penalty and simulated annealing there is no guarantee that the reported minimum is the true global minimum and not just a local one.

3.4 Small-angle Neutron Scattering

3.4.1 Neutron Production

Neutron production for scattering experiments is accomplished through either nuclear reactors or spallation sources. In nuclear reactors, a radioactive material, such as ^{235}U , acts as the nuclear fuel for the fission reactor. As the uranium decays, neutrons are emitted with high energy $E=2\text{ MeV}$ and need to be cooled or moderated to 1-50 meV to reach the desired wavelength and q range. Typical moderators are water and liquid hydrogen. The neutrons lose energy with each collision before exiting beam tubes and traveling to experimental beam lines.

The second method for neutron production is spallation (Figure 2.9). At sources such as the Spallation Neutron Source (SNS) at Oak Ridge National Laboratory (ORNL), high-energy collisions produce neutron beams. First, an ion source produces negatively charged ions and injects them into a linear accelerator. As the ions travel down the accelerator, they pass through a series of electrodes. A voltage is supplied to the electrodes which accelerates the ions and increases the energy up to 1 GeV. After acceleration the ions pass through a diamond stripper foil which strips off the electrons before entering the proton accumulator ring. The protons are focused into a tight beam and sent to a mercury liquid target. Each proton collision ejects 20-30 neutrons that are guided through

moderators to decrease their energy to thermal or cold neutrons that can be used for scattering experiments.

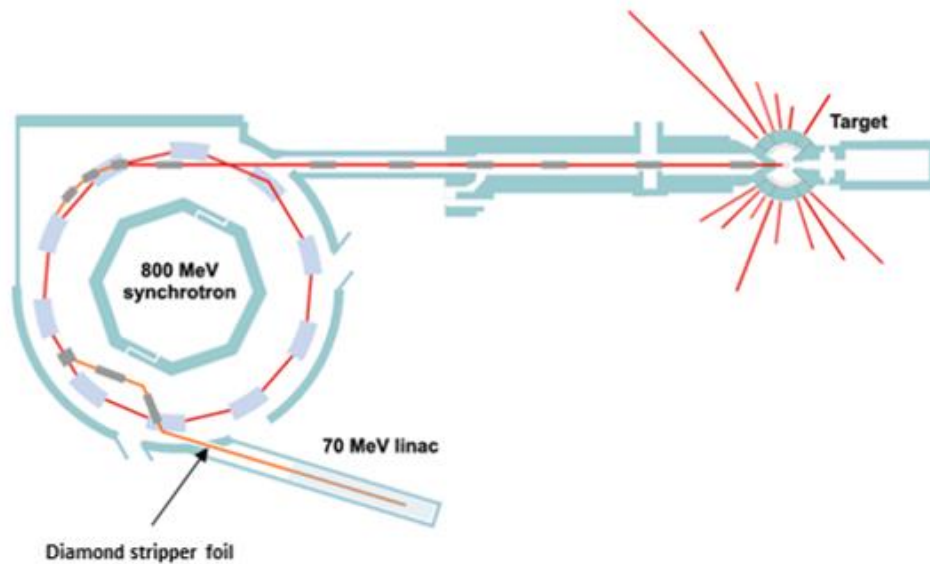


Figure 3.7. Schematic of spallation neutron source. In this schematic, negative ions are accelerated down the 70 MeV linear particle accelerator (LINAC). At the end of the accelerator a foil strips off the electrons. The resulting protons travel around the synchrotron before being tightly focused and sent to the target. Adapted from reference 132.

There are benefits and drawbacks to spallation and reactor sources. The reactors emit neutrons continuously, but the neutron energies are more varied. Scattering experiments require known neutron energies so in many cases the neutrons will be filtered out and the overall flux is decreased. Nuclear reactors also require nuclear fuel and add to the growing amount of nuclear waste requiring proper disposal. Spallation sources do not create nuclear waste and provide a greater amount of control over neutron energies by using a particle accelerator.

3.4.2 *Experimental Setup*

Experiments were performed at the Extended Q-range Small-angle Neutron scattering instrument at ORNL's SNS facility.¹³³ Cerato-ulmin with a concentration of 2.0 mg/mL was placed in 0.5 mL banjo cells with a 1 mm path length and exposed to the beam for 6 hours at a flux of $\sim 108 \frac{\text{neutrons}}{\text{cm}^2 \cdot \text{sec}}$. Banjo cells are circular flat glass cells named for their overall shape. Spectra were reduced to absolute intensity and plotted against q in inverse nanometers.

3.5 **Small-angle X-ray Scattering**

3.5.1 *X-ray Production*

Synchrotron X-ray sources provide high-energy and high-flux beams that are useful for a wide variety of experiments. In solution scattering, synchrotrons are often preferable as the scattering is so weak that a sample in a lab-based source requires hours of exposure to equal seconds at a synchrotron. This allows for measuring dynamics in a system and results in a greater possible number of experimental runs. Synchrotrons do have some disadvantages such as costs to build and maintain. There are only twelve synchrotrons in the United States so experimental time is strictly regulated.

The production of X-rays begins with the emission of electrons from an electron gun's cathode. The electrons are accelerated with oscillating electric fields to >99.999% of the speed of light or ~450 MeV. These electrons are injected into a booster synchrotron that accelerates the electrons to 7 billion electron volts or 7 GeV before entering the

electron storage ring. When charged particles experience centripetal acceleration, they emit photons with power

$$P = \frac{q^2 v^4 \gamma^4}{6\pi \epsilon_0 c^3 r^2} \quad (36)$$

where q is the elementary charge, v is the velocity of the electron, γ is the Lorentz factor, ϵ_0 is the permittivity of free space, c is the speed of light, and r is the radius of the storage ring. These photons are focused with sub-millimeter precision and create the X-ray beamline used in experiments.

3.5.2 *Experimental Setup*

SAXS experiments were carried out at the Stanford Synchrotron Radiation Light source (SSRL), beam line 1–5. The beam is highly collimated with a spot size of 300×300 μm and an approximate flux of 10^{11} photon $\cdot\text{sec}^{-1}$. The sample to detector distance was 869 mm and a Rayonix 165 CCD camera was used as the detector. The incident energy was 15 keV. Samples were placed in a custom-built flow cell with Kapton® films separated by 1 mm. The spectrum is the summation of 20 runs of 60 second exposure. For transmission correction and background subtraction Nanopure® water was exposed in the same manner as the sample. Samples and the solvent were centered in the beam by seeking the minimum transmittance. Data reduction was performed using the Nika package for Igor Pro (version 6.37) and fitting was done using SasView and the Irena package for Igor Pro. An absolute data correction was applied using a glassy carbon standard supplied by Jan Ilvasky at Argonne National Laboratory.¹³⁴

3.6 Atomic Force Microscopy

3.6.1 Basic Theory

AFM was developed by Binnig et al. in 1986 shortly after his discovery of the scanning tunnelling microscope (STM) in 1982, for which he received the Nobel Prize in Physics in 1986 with Ernst Ruska and Heinrich Rohrer.¹³⁵⁻¹³⁶ The scanning tunnelling microscope works off the quantum tunnelling effect, one of the many counterintuitive phenomena of quantum mechanics. Quantum tunnelling occurs when a particle passes through a potential barrier instead of overcoming it. The effect is only seen for particles small enough to exhibit wave-particle duality such as electrons. If a voltage is applied between two surfaces in a vacuum that are very close together there is a probability that an electron will tunnel through the potential barrier of the vacuum to the other surface. This probability is dependent on the voltage applied, distance between the surfaces, and energy of the electron. By using a small cantilever tip with a constant voltage, the resulting current changes are recorded as the tip is moved up and down to change the distance between it and the surface. As the tip moves across the surface of the sample, the surface morphology is imaged.

AFM uses a similar experimental setup of a cantilever tip close to the surface but relies on different phenomena. Depending on the material, different electric forces such as Van der Waals, dipole-dipole interactions, and electrostatic are present on the surface of a sample. In a tapping mode AFM, the cantilever is vertically oscillated up and down near its resonant frequency. As the cantilever is moved to different heights above the sample the forces interact with varying strength and affect its oscillation amplitude. This

amplitude is measured by the deflection of a laser beam (Figure 3.8) to determine the distance to the surface.

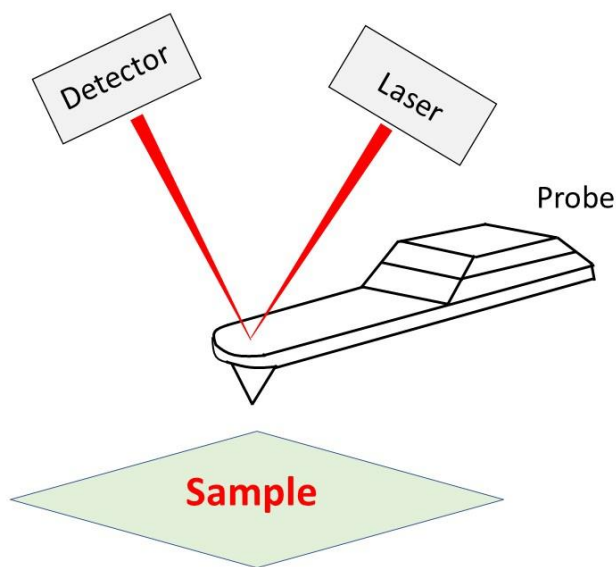


Figure 3.8. In tapping mode AFM measures the changes in the laser deflection as the probe oscillates and interacts with the sample.

The experiments in this chapter use the tapping mode on the AFM as it decreases the direct contact with the surface and does not have any potential issues of lateral forces seen in contact mode AFM. This makes it a good choice for soft materials such as the bubble layers created by cerato-ulmin.

3.6.2 Experimental Setup

An ICON Dimension (Bruker) scanning probe microscope operating in tapping mode with a silicon tip (RTESP, Bruker) analyzed the surface morphology of the collapsed bubbles. An agitated solution (created in same manner as previously mentioned) of 0.02 mg/mL CU was drop cast on to a silicon wafer and allowed to dry overnight. An AFM

probe MPP-11100-10 was selected (cantilever length, 125 μm ; nominal force constant, 40 N/M, and resonance frequency, 300 kHz). Height, phase, and amplitude images were collected simultaneously. The image resolution was held constant at 512×512 pixels.

3.7 Materials

3.7.1 *Cerato-ulmin*

The cerato-ulmin used was a gift from Wayne Richards of the Canadian Forest Service. It was produced by a strain of *C. ulmi* (TDT2) and purified using the methods of Takai and Richards¹³⁷ and Stevenson et al.¹³⁸ Stock solutions were prepared in scintillation vials pre-cleaned with Type I water from Barnstead Nanopure or Millipore Milli-Q purification systems. To ascertain the absence of particulates, the water itself can be viewed optically and by photometric measurement in the light scattering instrument (see below). The purified CU is added to these pre-cleaned vials, along with the requisite amount of clean water. Cerato-ulmin has 73 amino acid residues with a molecular weight of 7626 $\text{g}\cdot\text{mol}^{-1}$. The sample integrity was verified through matrix assisted laser desorption/ionization (MALDI) as shown in Figure 3.9.

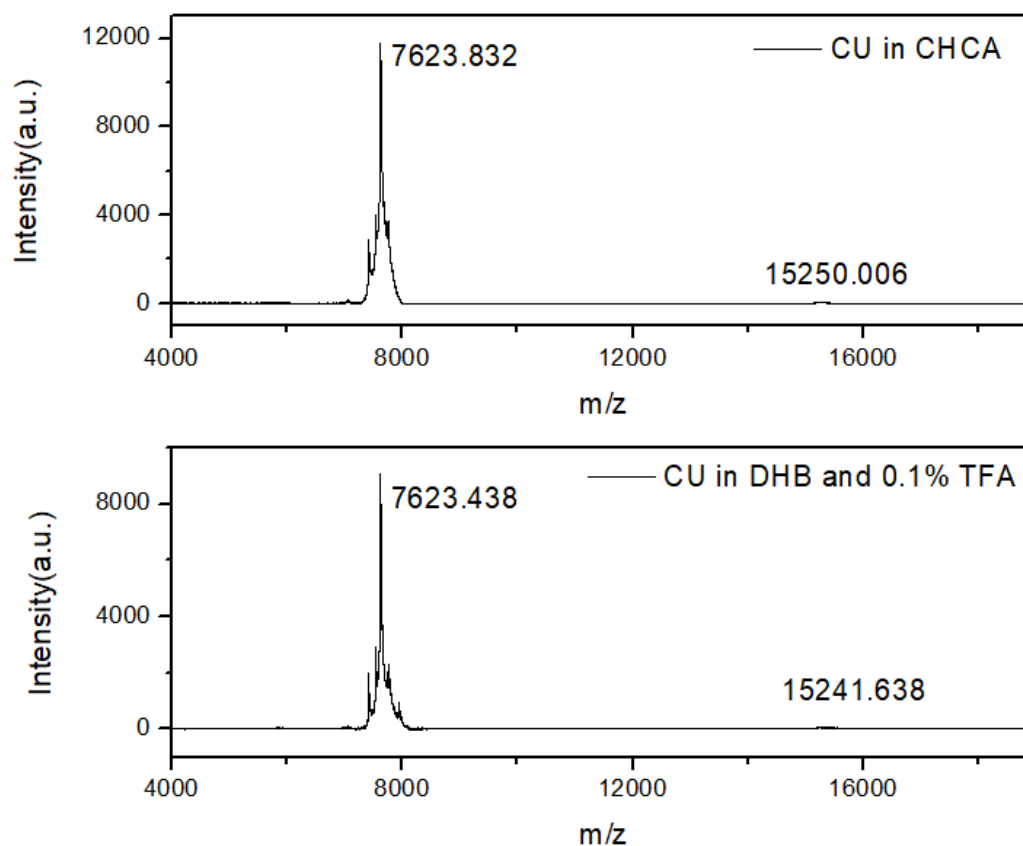


Figure 3.9. MALDI of cerato-ulmin shows a molecular weight of 7626 g·mol⁻¹ which is expected from the 73 amino acid protein. Take with permission from reference 89.

3.8 Results and Discussion

3.8.1 Optical Microscopy

Microscope images allow for an elementary estimate of the CU thickness in bubbles by a simple volumetric calculation. A $c = 0.02$ mg/mL aqueous solution of CU was gently shaken in a rocking motion to produce bubbles. There were 309 bubbles in a viewing area of $1.24 \times 10^5 \mu\text{m}^2$ as shown in Figure 3.10.

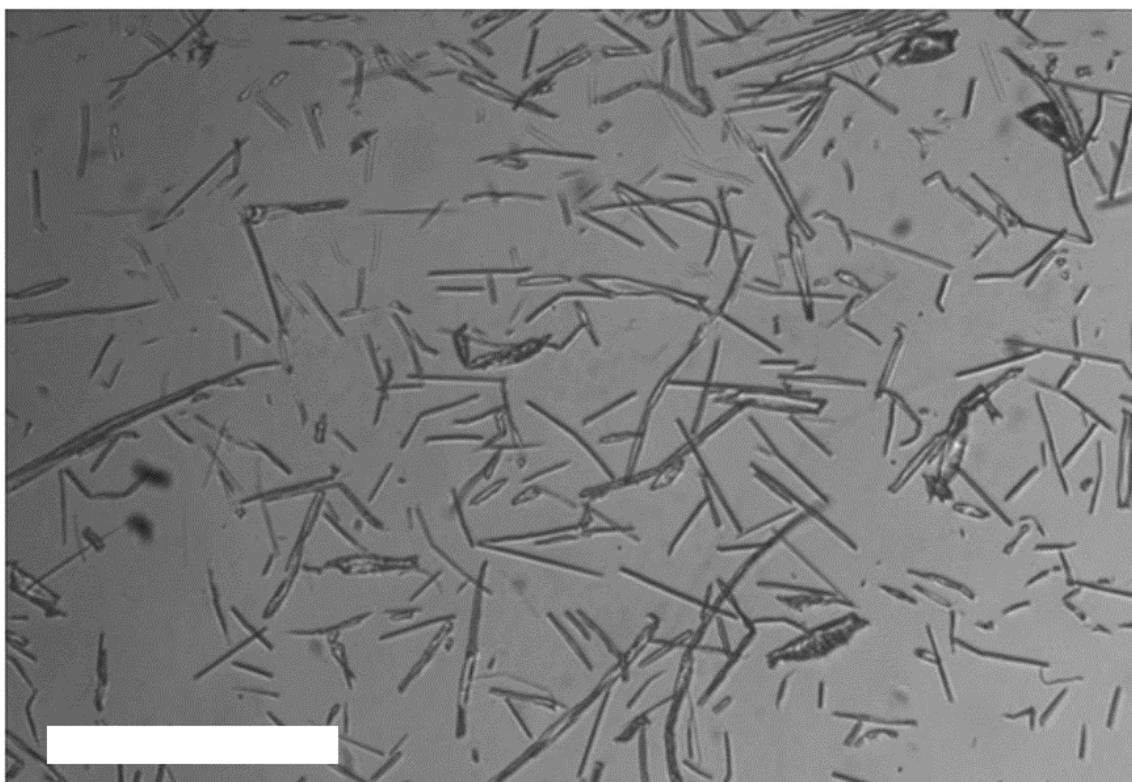


Figure 3.10. CU forms cylindrical bubbles when a solution is agitated in a VitroCom glass cell (scale bar 100 μm).

The depth of field was estimated to be 18 μm from the width of the widest bubble and all bubbles were assumed to be perfect cylinders even though the image contradicts this. By tracing over all the bubbles in the image and assuming them to be cylinders it is possible to calculate the surface area of each bubble as $A_{\text{surface}} = 2\pi r^2 + 2\pi r h$ where r is the radius of the cylinder and h is the height of the cylinder.

The calculation of the radius of a single CU protein was done through the mass volume relation $V_m = \frac{M}{\rho N_a}$ where the molecular weight M is 7.63 kDa, the protein density ρ is 1.5 $\text{g}\cdot\text{mL}^{-1}$, and N_a is Avogadro's number.¹³⁹ This assumes a spherical protein and yields a radius of 2.1 nm. By dividing the total surface area of the bubbles and cross-

sectional area of one CU protein assuming a square packing, we find that 2.52×10^{10} CU proteins are needed to cover the surface; however, according to the concentration and image volume there are only 3.54×10^9 proteins (Table 3.1). Even with no proteins existing in solution this means that the CU would not be able to cover the entire area of all the bubbles in a square packing formation.

Table 3.1. CU bubble thickness estimate from optical microscopy results

Measurement	Value	Units
ρ	1.5	$\text{g} \cdot \text{mL}^{-1}$
Height of field	407	μm
Width of field	305	μm
Depth of field	18	μm
Image volume	2.32×10^6	μm^3
A_{surface} all bubbles	1.11×10^5	μm^3
Cerato-ulmin radius	2.1	nm
M	7.63	kDa
Concentration of CU solution	0.02	mg/mL
Number of CU proteins in viewing volume	3.54×10^9	
Proteins needed for one layer of square packing CU proteins	2.52×10^{10}	

While this exercise concludes that the bubble film is only one protein thick, this should be viewed skeptically as the amount of assumptions needed to arrive at the answer are staggering. The surface area of the bubbles, concentration, shape of CU are all imprecise measurements. The surface area of the bubbles was calculated assuming all bubbles to be right cylinders, but a quick examination of the image shows this is clearly not the case. The concentration may be accurate by using good experimental procedures in solution preparation but there is no way to judge how those proteins are allocated in the

solution. It is possible there could be free proteins in solution or smaller bubbles or aggregates that are not visible at this magnification. This possibility was confirmed in future DLS and SAXS experiments. Finally, the shape of the protein when it assembles into the bubble film is unknown. When the CU forms the bubble film it is possible that the morphology changes and covers a larger surface area per protein.

With the assumptions and large uncertainties involved in arriving at an estimate, it is a fair question to ask why the calculation was performed and why such an uncertain calculation is being reported. The answer can be broken down into two parts — resources and future experimentation. There is a finite amount of resources available for research, whether those resources are money, equipment access, or time. Therefore, it is best to begin any search for answers with the most viable method and least opportunity cost. It is simply scientific malfeasance to use multiple trips to particle accelerators and complex modelling to solve a problem that could be done by a microscope and image processing.

Second, the calculation is valuable because it creates a benchmark for subsequent experiments. It contains many assumptions but none of the assumed values are unreasonable to the point that it is not roughly one order of magnitude. This would mean that the bubble layer could be one protein thick with large distances between proteins in their assembly or 10-20 proteins thick. Having this rough area starting point for an estimated thickness aids in fitting the experimental SAXS data.

3.8.2 Small-angle Neutron Scattering

Small-angle scattering of solutions is one of the more difficult experimental techniques for acquiring data and making meaningful conclusions. Scattering is a weak

effect and almost all incident radiation either passes through or is absorbed by the sample. When exposing a solution to the incident radiation the measured scattering is then the sum of the sample and solvent so a second measurement to subtract the sample is necessary. After this subtraction the remaining signal is miniscule compared with the incident flux, so it is important to minimize potential confounding variables such as differences in capillaries. After correctly reducing the data to the sample, solution scattering still poses some challenges. In many cases the particles in solution are isotropic. The scattering is averaged over all orientations so it can be difficult to distinguish various shapes. For determining shape the best methods are to fit a particle form factor to the data or use *ab-initio* modeling such as DAMMIF in the ATSAS suite of programs.¹⁰⁷

When agitated in an aqueous solution using the method described previously CU protein self-assembles into nonspherical microbubbles (Figure 3.10). Bubbles are traditionally spherical in shape as a sphere has the lowest surface area and distributes the surface tension equally across the entire surface. The stability of the cylindrical bubbles is a curiosity and justifies further exploration of the bubble structure.

To probe the structure of the protein, small-angle neutron scattering (SANS) was performed in the range $0.5 < q < 15 \text{ nm}^{-1}$ corresponding to the characteristic lengths $0.4 < d < 12.6 \text{ nm}$ according to the relation $q = \frac{2\pi}{d}$.

The scattering pattern (Figure 3.11) does not provide any information at first glance but there is still information that can be coaxed out of the pattern using ATSAS.

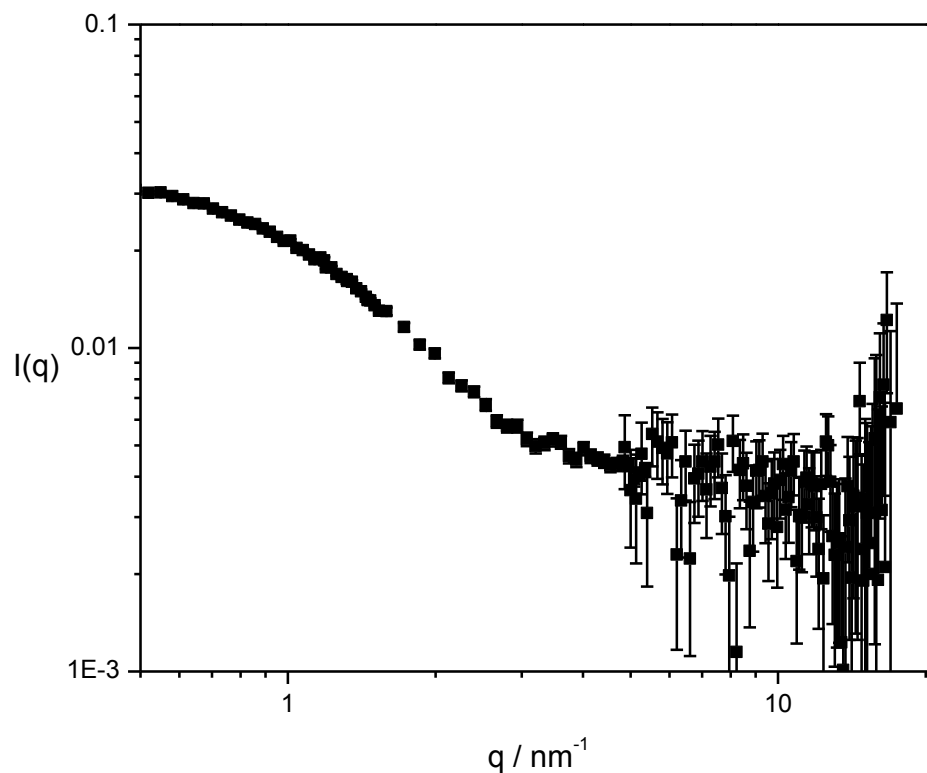


Figure 3.11. Small-angle neutron scattering envelope of cerato-ulmin bubble dispersion. Bubbles were created by agitating a 2 mg/mL solution.

The scattering pattern is entered into the program GNOM to calculate the pair distance distribution function (PDDF) (Figure 3.12).¹¹⁵ GNOM determines the PDDF through the regularization technique in conjunction with perceptual criteria of the best solution.

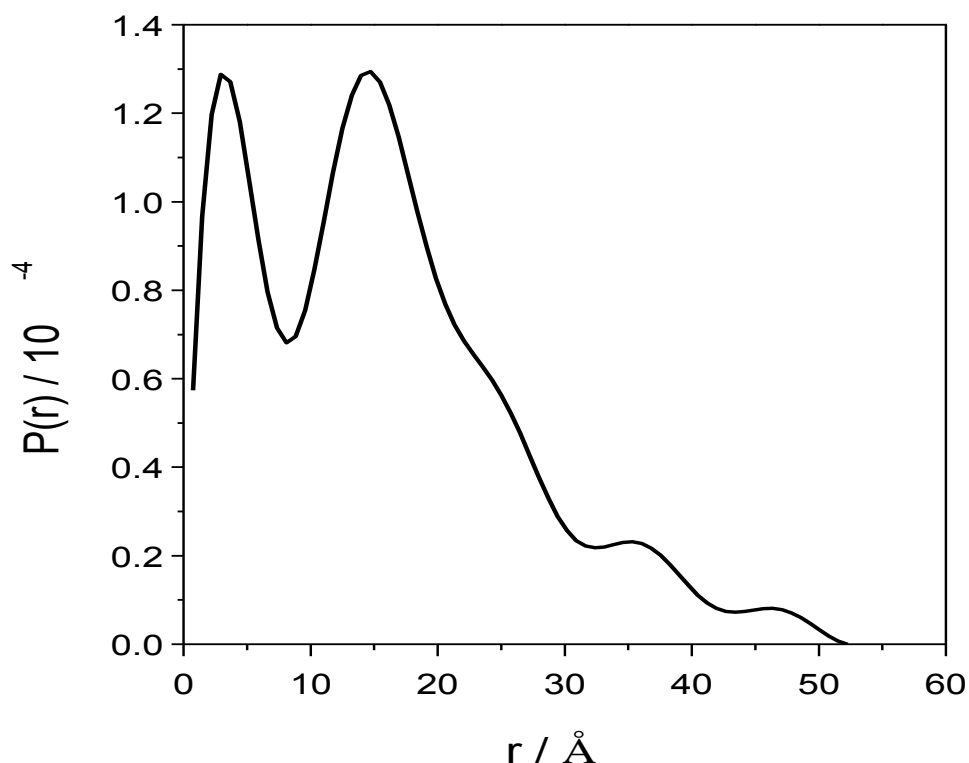


Figure 3.12. The pair distance distribution function of the CU protein measured at the EQ-SANS beamline.

Comparing the pattern with other known shapes, the CU likely elongates into a cylindrical structure when assembling into the bubble film. To get a better idea of the shape, DAMMIF¹⁰⁷ uses *ab-initio* modelling to create a three dimensional representation of the scatterer. The above-described program uses a dummy atom model system and Monte Carlo simulated annealing to calculate models. The ATSAS program DAMAVER averages 10 DAMMIF runs (Figure 3.13) to calculate a likely structure of the protein in the film (Figure 3.14).¹⁴⁰ The model suggests that the protein elongates in the film and forms a cylindrical structure rather than a globular protein. The protein is ~4 nm long with a ~1 nm diameter.

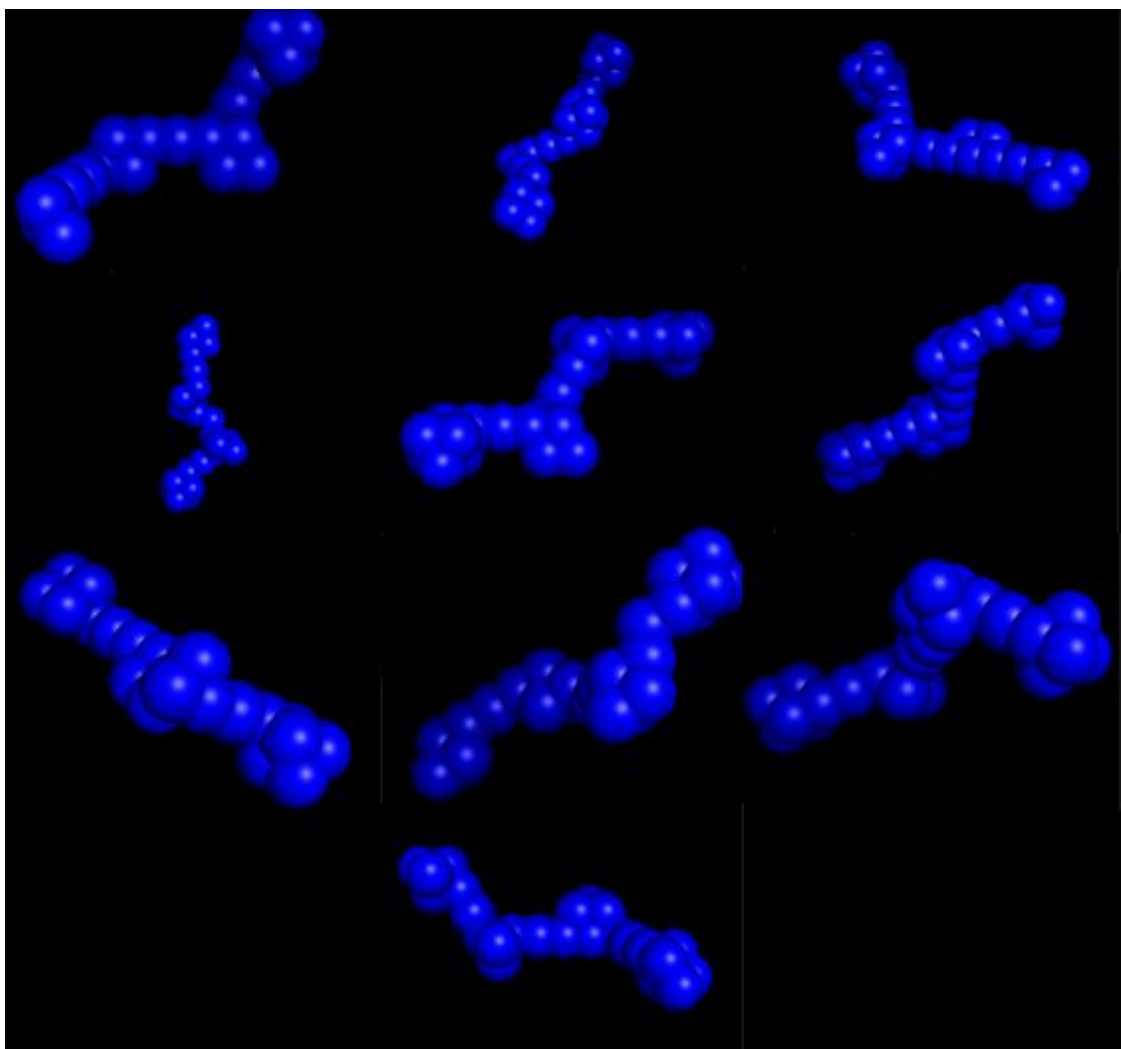


Figure 3.13. DAMMIF models calculated from the pair distance distribution function of SANS data. Sample was an agitated $c = 2$ mg/mL cerato-ulmin solution of bubbles exposed to the beam for 6 hours. The magnification is not equal on each individual image.

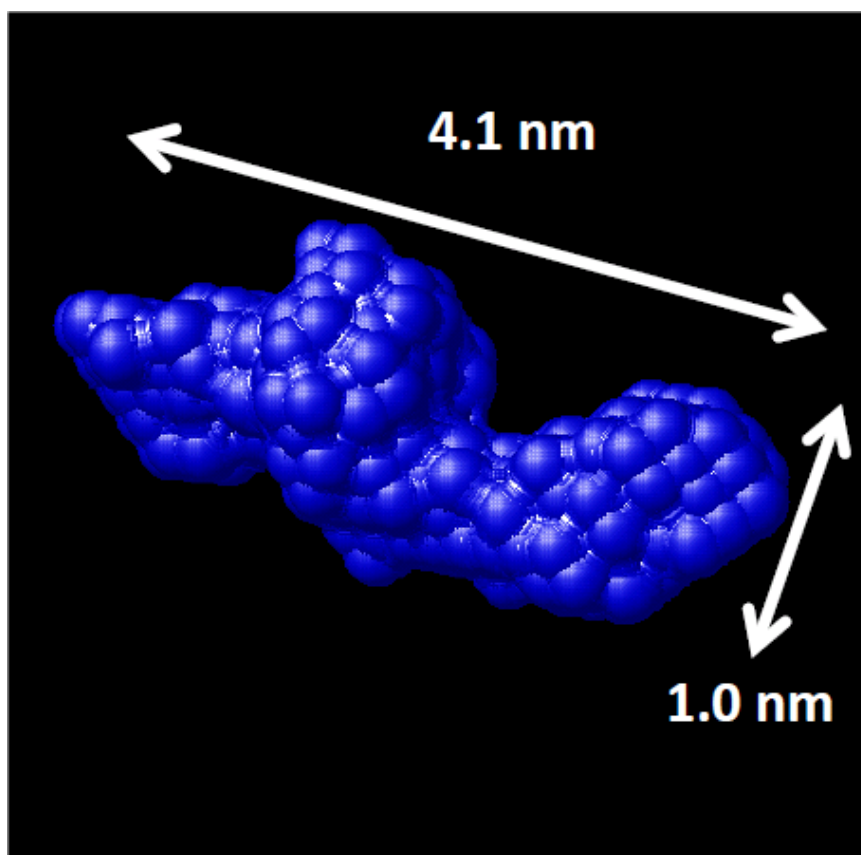


Figure 3.14. DAMAVER model of CU suggests the protein exists in an elongated structure in the bubble film

This model does require some assumptions. The first is that the scattering from the proteins in the bubbles is much more dominant than scattering from any free proteins that may be in the solution. It is unlikely that all proteins are in the bubbles but if the amount of proteins free in solution is small then the overall scattering may not influence the overall pattern and thus obscure the results. Also, the ATSAS programs are normally used for dilute proteins that have no interaction with other scatterers and are only surrounded by solvents. For the bubbles this is not the case as the CU is packed together. Not much that can be done to address this issue as the CU naturally assembles into structures. It is because

of these assumptions that the conclusions are only for the overall shape and size of the protein in the bubble film.

3.8.3 *Small-Angle X-ray Scattering*

3.8.3.1 Preliminary Simulations

SAXS experiments at national labs often require more time and expenses than other experiments. Beam time requires proposal submissions and time is allocated based off the quality and impact of the research topic. The amount of beam time available is limited, so it is important to make the best use of the time allocated and acquire the necessary information as quickly as possible. For these reasons it is important to know the q -range to probe and the approximate pattern that would result. This can be achieved through an examination of previous experiments in the literature or simulating the data. Since there is no prior X-ray scattering of CU bubbles the expected data was produced through modeling.

For the overall pattern, the best method to determine the size and shape is fitting a particle form factor for the scatterer. Since bubbles are typically spherical, the first attempt used a spherical core-shell model¹¹⁸ with scattering length densities (SLD) of air, protein, and water (Table 3.2).

Table 3.2. Scattering length densities of components in the CU solutions.

Material	SLD ^a / Å ⁻²
Air	1.07×10^{-8}
Cerato-ulmin	1.18×10^{-5}
Water	1.68×10^{-5}

^aSLD is the scattering length density

The spherical core-shell model is best described as the sum of the scattering from the core and shell

$$P(q) = \frac{scale}{V_s} \left[3V_c(\rho_c - \rho_s) \frac{[\sin(qr_c) - qr_c \cos(qr_c)]}{(qr_c)^3} + 3V_s(\rho_s - \rho_{solv}) \frac{[\sin(qr_s) - qr \cos(qr_s)]^2}{(qr_s)^3} \right] + bkg \quad (37)$$

with the variables listed in Table 3.3.

Table 3.3. Variables for the core-shell model form factor equation.

Variable	Name	Units
$Scale$	Scale factor	arb unit
bkg	Background	arb unit
V_s	Volume of the outer shell	\AA^3
V_c	Volume of the core	\AA^3
ρ_c	Scattering length density (SLD) of core	\AA^{-2}
ρ_s	Scattering length density (SLD) of shell	\AA^{-2}
ρ_{solv}	Scattering length density (SLD) of solvent	\AA^{-2}
r_c	Radius of core	\AA
r_s	Radius of shell	\AA

As the aim of these experiments is to measure the thickness of the bubble, a higher q -range is selected that focuses on length scales relating to bubble thickness and does not extend to lower q regions that would relate to the scattering of the entire bubble. Figure 3.15 shows 4 data simulations of a spherical core-shell fit for different bubbles with the same film thickness but different sizes. For all four bubble populations, the scattering patterns have the same general shape of a shoulder followed by three bumps. The differences come from the higher frequency secondary oscillations over the entire curve. As the bubbles increase in size the secondary oscillations decrease in amplitude because they become so large their scattering contribution in that q -range becomes negligible.

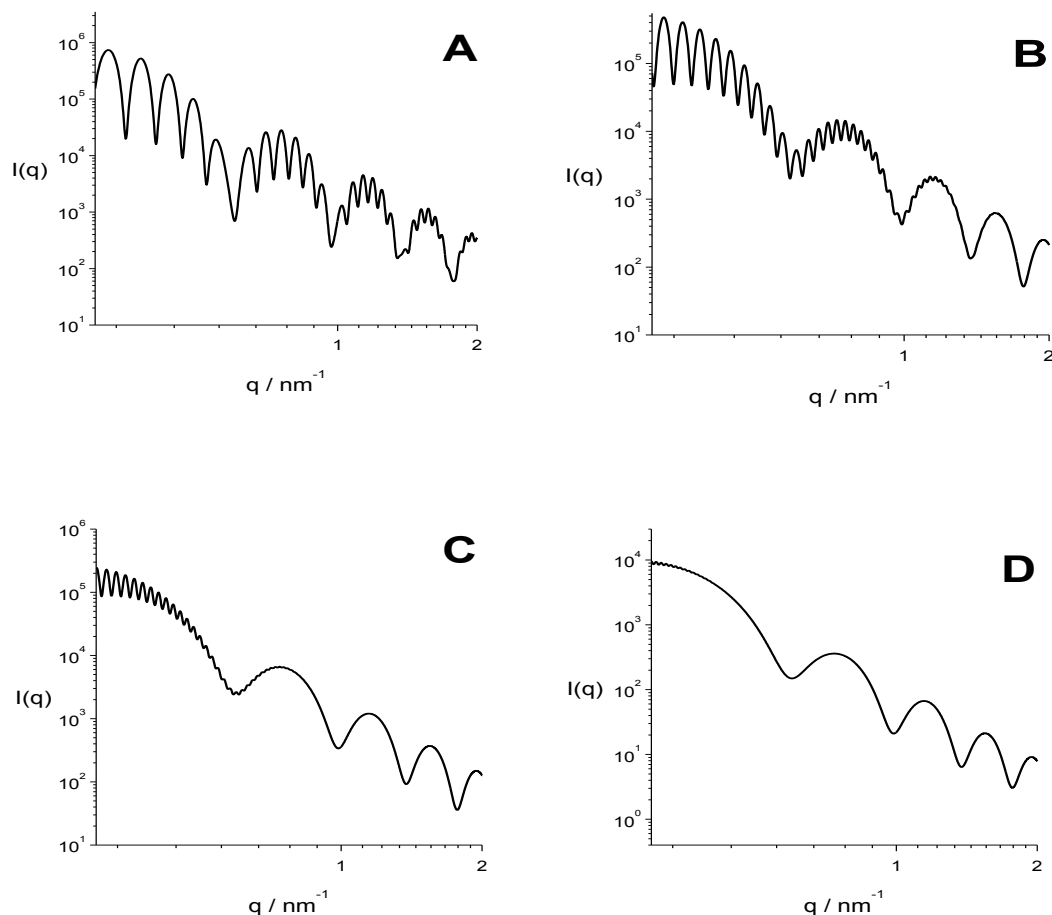


Figure 3.15. Spherical core-shell fits with 16 nm thickness and varying radii: (A) 50 nm; (B) 100 nm; (C) 200 nm; (D) 400 nm.

Though it appears possible to distinguish between the scatterers in Figure 3.15, experimentally it is frequently not so. These simulated graphs have a small amount of polydispersity in the patterns as a matter of practicality and visualization. Figure 3.16 demonstrates that as the size polydispersity increases the secondary oscillations disappear. Even using a sample with a standard deviation of 1% it would be difficult and at 5% differentiation between scatterers becomes fruitless. This is one reason selection of q -range is important. Using the wrong q -range means identifying features in the pattern will be “smoothed” out.

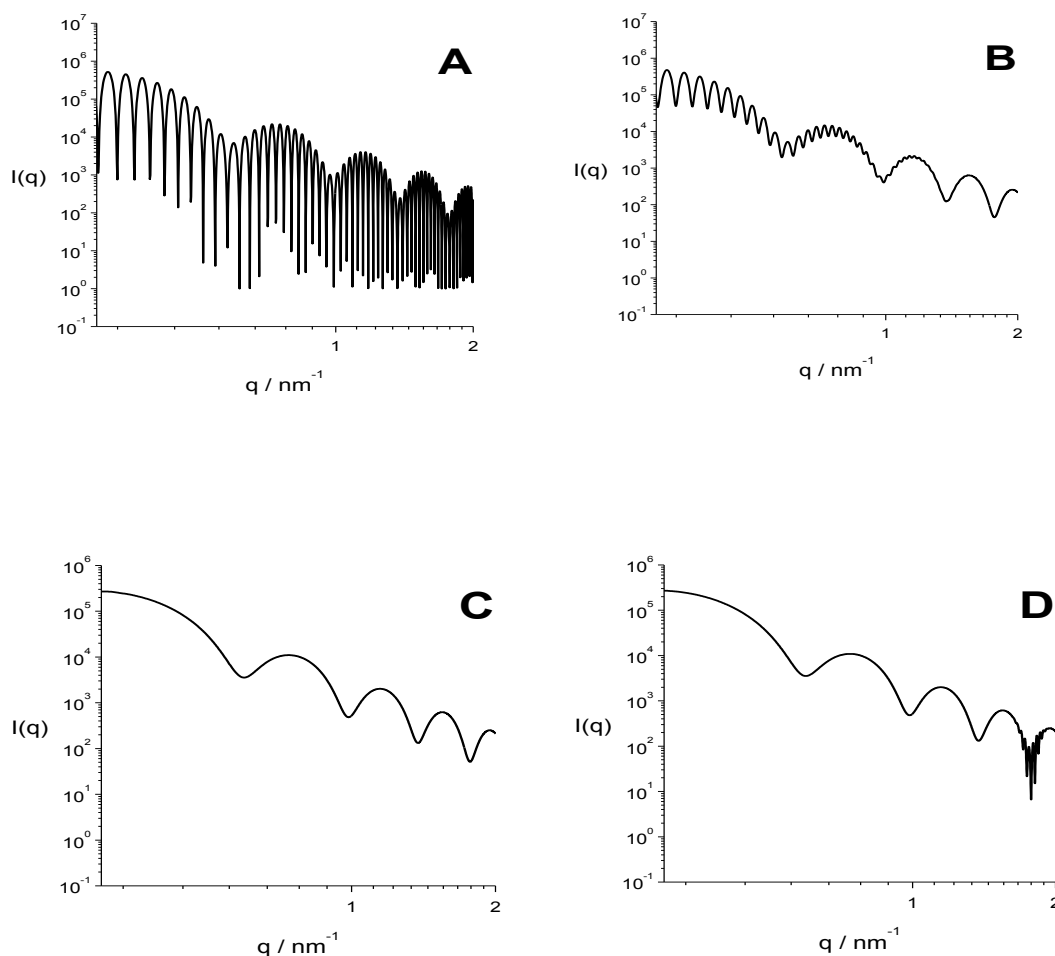


Figure 3.16. The effect of standard deviation of the radius in a 200 nm bubble with 16 nm thickness: (A) No standard deviation; (B) ± 2 nm; (C) ± 10 nm; (D) ± 20 nm.

Selecting the higher q -range means the smaller features make the most dominant contribution to the scattering. In this region, thickness of the bubble affects the overall pattern rather than just secondary oscillations. In Figure 3.17, the different thicknesses change the scattering pattern more noticeably than Figure 3.15 as shown by the different number of “bumps” and the position change of the shoulder in each graph. These differences will be easier to distinguish because the “smoothing out” by polydispersity will not be as damaging. When keeping the bubble size constant and altering the thickness of

the bubble film the patterns do shift because the thickness has more of an effect on the high- q behavior (Figure 3.17).

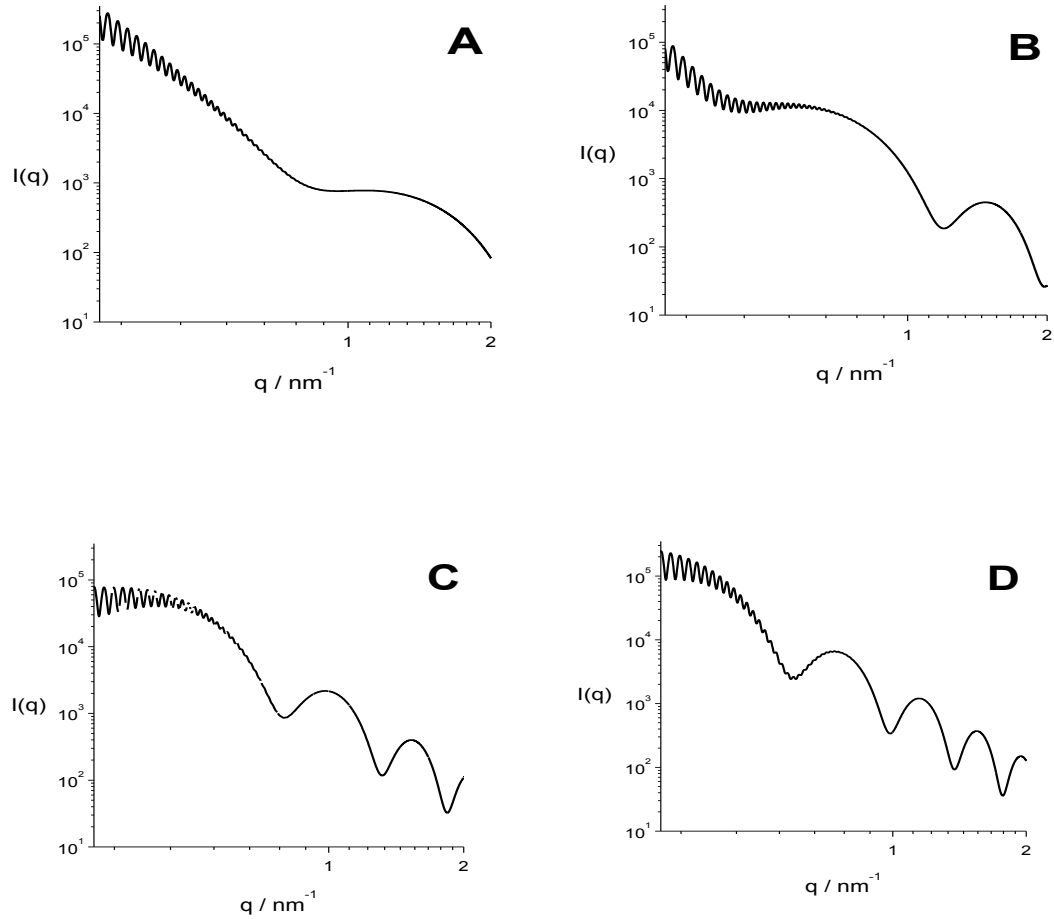


Figure 3.17. Spherical core-shell models with a 200 nm radius but different thicknesses: (A) 4 nm; (B) 8 nm; (C) 12 nm; (D) 16 nm.

The second possible form factor for the bubbles is a cylindrical core-shell model¹⁴¹ (Figure 3.18). If we assume the submicron bubbles seen in DLS and SAXS retain the same cylindrical shape as the microbubbles this would be a more accurate model.

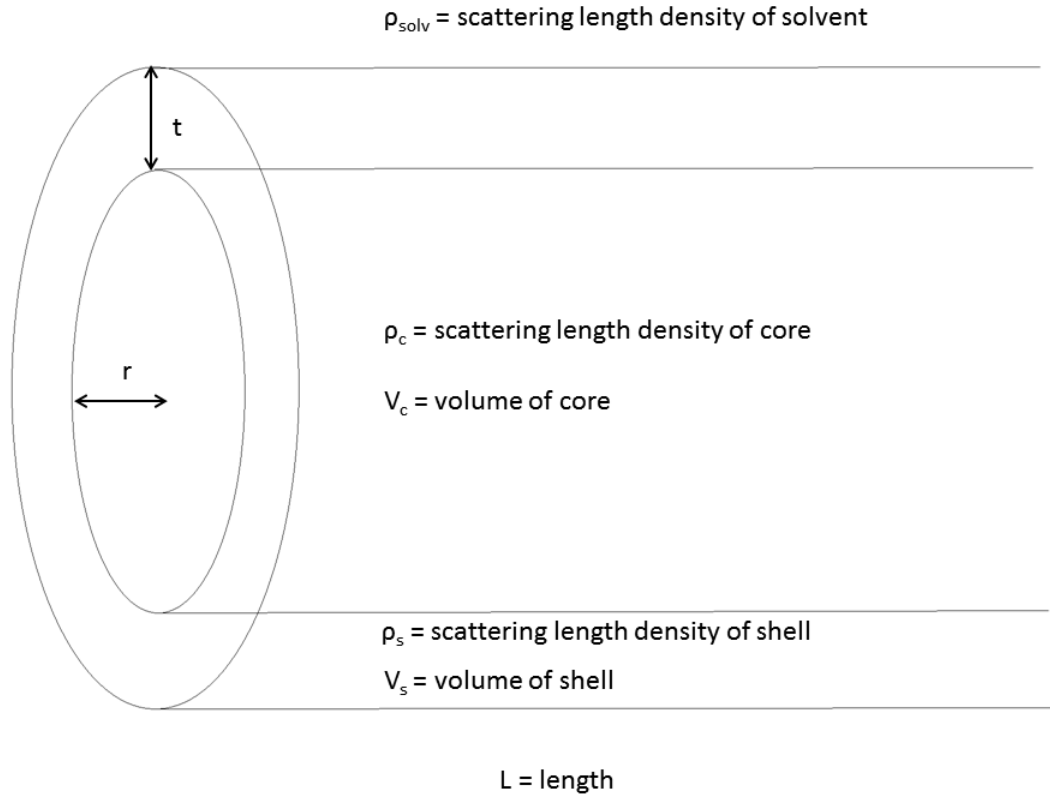


Figure 3.18. Schematic of a cylindrical core-shell model with accompanying variables.

The intensity of scattering is proportional to the form factor, $I(q) \propto P(q)$

$$P_{core-shell\ cylinder}(q, \alpha) = \frac{scale}{V_s} \int_0^{\frac{\pi}{2}} f^2(q) \sin \alpha \, d\alpha \quad (38)$$

where

$$f(q) = 2(\rho_c - \rho_s)V_c \sin \frac{[qL \cos \frac{\alpha}{2}]}{[qL \cos \frac{\alpha}{2}]} \frac{J_1[qr \sin \alpha]}{[qr \sin \alpha]} \quad (39)$$

$$+2(\rho_s - \rho_{solv})V_s \sin[q(L + 2t) \cos \alpha/2]/[q(L + 2t) \cos \alpha/2] \frac{J_1[q(r + t) \sin \alpha]}{[q(r + t) \sin \alpha]}$$

and

$$V_s = \pi(R + t)^2(L + 2t) \quad (40)$$

where p_1 and p_2 are the weights of the Guinier and core-shell cylinder functions, L and t are the length and thickness, r is the radius of the core, R_g is the radius of gyration, J_1 is the first order Bessel function, ρ is the scattering length density, α is the angle between the axis of the cylinder and the scattering vector q , and the subscripts c , s , and $solv$ represent the core, shell, and solvent, respectively. Because the bubbles are randomly oriented in solution the function is integrated over all angles.

In the cylindrical core-shell model, changing the length of the bubbles has almost no effect on the scattering pattern (Figure 3.19) in the measured q range. Even changing the length by a factor of eight has no discernible effect on the pattern.

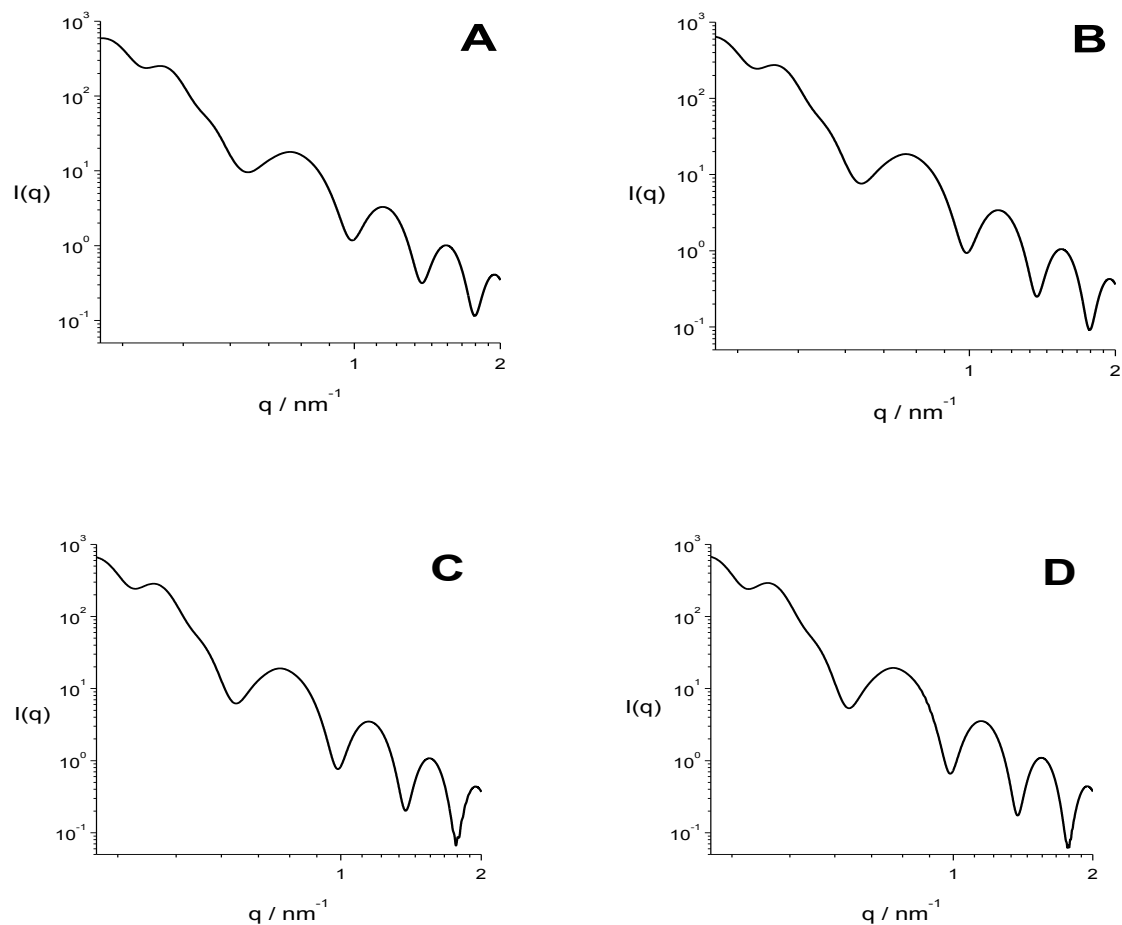


Figure 3.19. Cylindrical core-shell models with a 20 nm radius, 16 nm thickness, and various lengths: (A) 50 nm; (B) 100 nm; (C) 200 nm; (D) 400 nm.

As expected, the thickness of the bubble film in a cylindrical core-shell model has a large effect on the scattering pattern in the q -range (Figure 3.20). These differences should be protected from polydispersity smoothing and allow for an estimation of thickness.

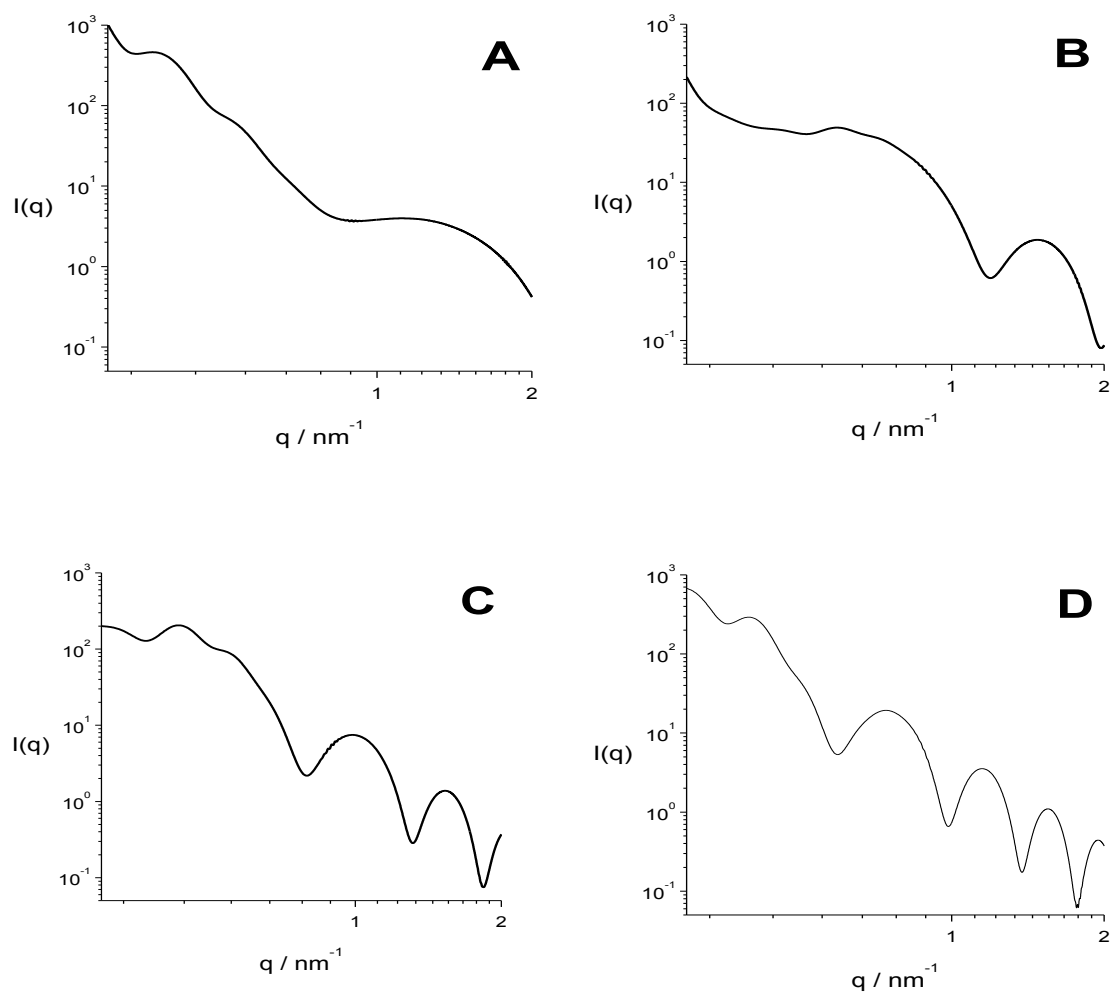


Figure 3.20. Cylindrical core-shell models with a 20 nm radius, 400 nm length, and various thicknesses: (A) 4 nm; (B) 8 nm; (C) 12 nm; (D) 16 nm.

The spherical and cylindrical core-shell models provide several insights to aid in the experiments. The available q -range for data collection will provide differentiated patterns for the bubbles as variables change. The pattern differentiation is most pronounced with thickness changes as its magnitude is closest to the characteristic length being probed so the scattering is most pronounced. For the larger features of spherical radius or cylinder length, the values will be difficult or impossible to measure. Changes in spherical radius only created secondary oscillations likely to be smoothed out by even small variations as

low as 5%. The cylinder length is even more unlikely to be meaningfully measured as changes up to a factor of 8 show no discernible change in the scattering pattern. Finally, there is a distinct difference between the patterns of a spherical and cylindrical core-shell model so it should be possible to judge whether the submicron bubbles are elongated like their larger brethren or are in a more conventional spherical shape.

3.8.3.2 Fitting of Experimental Data

The SAXS experiment probed a slightly lower q -range than that used with neutron scattering, capturing more of the overall shape of the bubbles and measuring the thickness of the film (Figure 3.21). The selected q -range — $0.17 < q < 8 \text{ nm}^{-1}$ —corresponds to a characteristic length of $0.8 < d < 37 \text{ nm}$.

Before executing any fitting procedures, some insights were uncovered. The scattering envelope can be divided into three regimes where different features dominate the scattering contribution. The low- q regime ($q < 0.7 \text{ nm}^{-1}$) relates to the overall shape of the bubble and is most affected by the thickness of the bubble film. This regime has a distinct peak at $q = 0.4 \text{ nm}^{-1}$ relating to a characteristic length of $d = 15 \text{ nm}$. The second is a Guinier regime extending to $\sim 2 \text{ nm}^{-1}$. The Guinier plot from this region (inset) gives a $R_g = 1.1 \text{ nm}$. This is close to the size of a protein with the mass of cerato-ulmin, assuming a spherical shape, which is given by $D = 2^3 \sqrt{\frac{3M}{4\pi\rho_p N_a}} = 2.6 \text{ nm}$ assuming $\rho = 1.3 \text{ g/cm}^3$ and mass $M = 7618 \text{ g/mol}$.^{77, 139} Finally, there is the high q -regime, where two peaks appear at $q = 4$ and 5.5 nm^{-1} , corresponding to $d = 1.57$ and 1.14 nm , respectively. These last two peaks lie in a regime where baseline subtraction may affect the results. Though intriguing

because they may reveal internal details of the CU protein or a possible packing distance, they are not considered in the fitting calculation. The features are briefly discussed later.

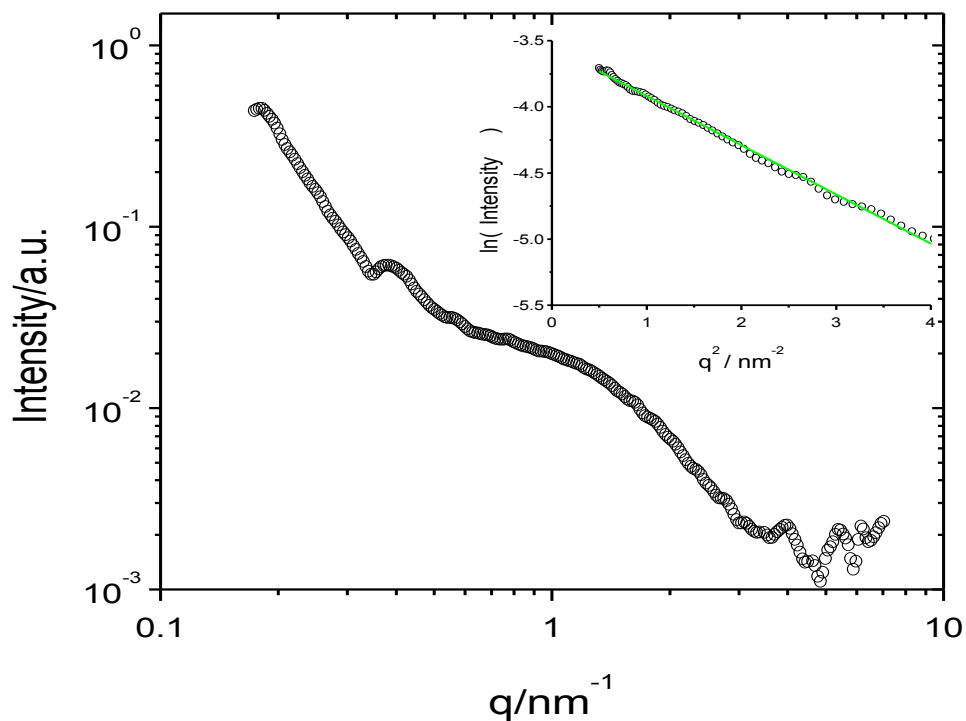


Figure 3.21. SAXS pattern of $c = 2$ mg/mL cerato ulmin bubble dispersion. Uncertainties are comparable in size to data points. Inset: Guinier plot.

Unsurprisingly, the experimental data is smoother than the simulated fits of the spherical and cylindrical core-shell models, suggesting the bubbles have a large size polydispersity similar to the microbubbles in Figure 3.10. This size polydispersity of the submicron bubbles is confirmed in the dynamic light scattering results discussed in Chapter 3.

Comparison of the experimental data with the simulated fits shown in previous figures indicates that the cylindrical core-shell model is probably correct. These models have a shoulder “bump” in the $q = 0.4 \text{ nm}^{-1}$ that is not seen in the spherical core-shell models regardless of size dimensions. The shoulder bump is also isolated with no surrounding features. The spherical core-shell model has equidistant bumps across all q in this region; changing parameters in this model only affects the frequency, position, and amplitude of the bumps. The cylindrical core-shell model though has an isolated shoulder in some iterations, as seen in Figure 3.22.

Though the cylindrical core-shell model is the most promising model at first glance, both models were used to try to fit the data. In Figure 3.22, the data was fit using the spherical and cylindrical core-shell models. In both cases the models fail to account for the intensity of scattering in the region of $0.6 < q < 2 \text{ nm}^{-1}$.

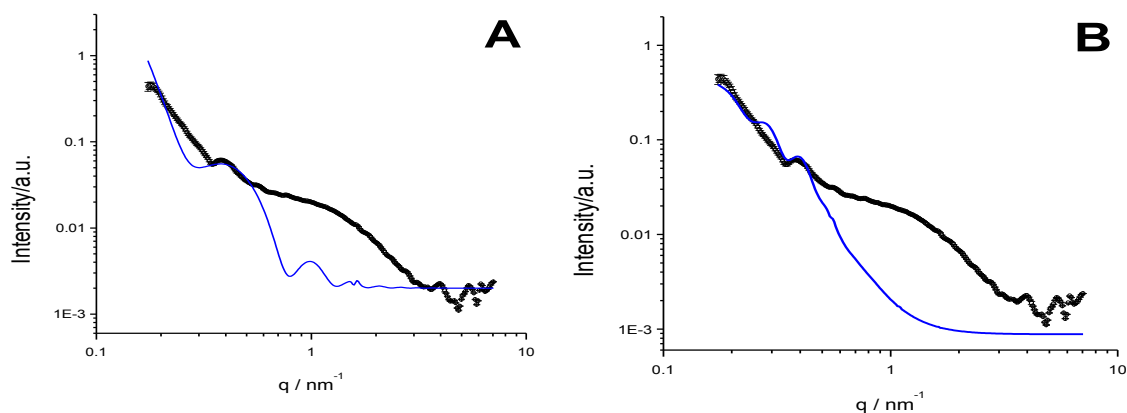


Figure 3.22. SAXS pattern of $c = 2 \text{ mg/mL}$ cerato-ulmin bubble dispersion with fit using different form factors: (A) Spherical core-shell model; (B) Cylindrical core-shell model.

The q -range where the model fails severely is the Guinier region that relates to the size of the individual protein. This suggests that there are free CU proteins in solution contribute to the scattering intensity, so a single component model is insufficient to explain the scattering intensity. To account for this, custom models were created that would account for the scattering of the proteins in the Guinier regime. These models in Figure 3.23 improved the fitting accuracy considerably.

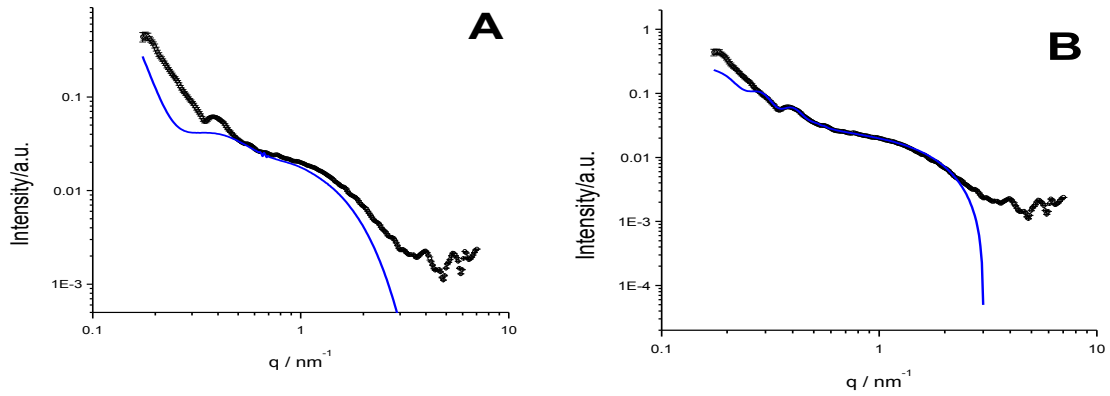


Figure 3.23. SAXS pattern of $c = 2$ mg/mL cerato-ulmin bubble dispersion with fit two custom models: (A) Spherical bubbles with free CU proteins in solution; (B) Cylindrical bubbles with free CU proteins in solution.

Between the two models, the cylindrical bubble model shown in Figure 3.23B fits the data most accurately. By combining the Guinier equation

$$P(q) \propto I(q) = I_0 e^{\frac{-R_g^2 q^2}{3}} \quad (41)$$

with the cylindrical core-shell model, the custom model becomes

$$I(q) = p_1 P(q)_{core-shell\ cylinder} + p_2 P(q)_{Guinier} \quad (42)$$

where p_1 and p_2 are the weights of the Guinier and core-shell cylinder functions. This custom model created a good fit for the experimental data (Figure 3.24).

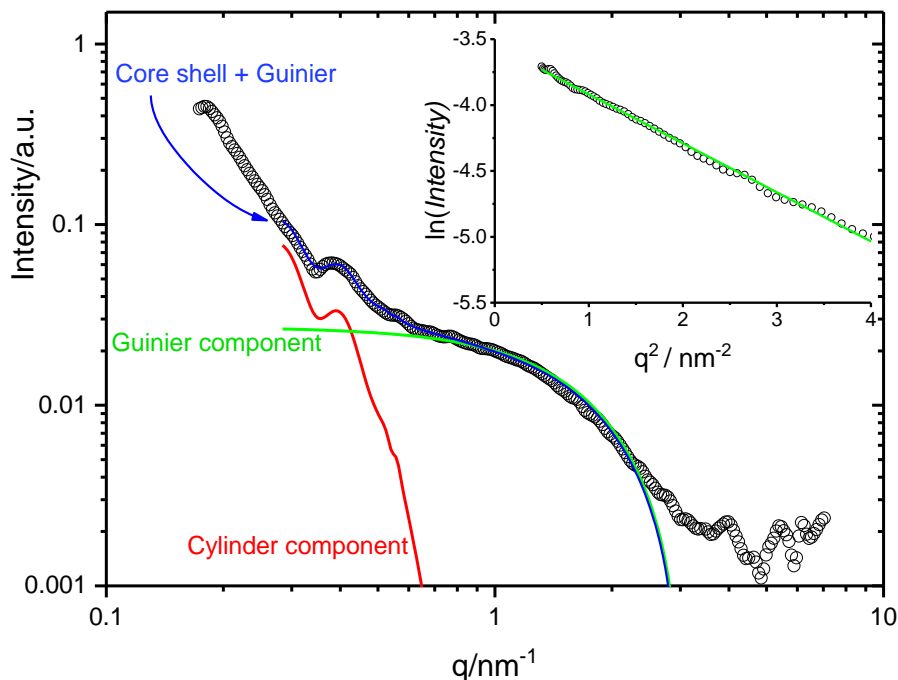


Figure 3.24. SAXS pattern of $c = 2$ mg/mL cerato-ulmin bubble dispersion and fit with a combination of a core-shell cylinder model representing the assembled structure and Guinier regime mostly representing free protein in solution. Uncertainties are comparable in size to data points. Inset: Guinier plot.

The improvement in the fit by adding the Guinier term suggests that not all CU proteins assemble into the bubble structures, with some existing as free proteins in solution. The results of the fit gives an external diameter $2(r + t)$ of 69 ± 5 nm with a thickness of $t = 13.6 \pm 3.2$ nm. Thus, the inner cavity has a diameter of ~ 40 nm. The thickness parameter is the most influential on the overall scattering pattern in this q -range and is the most reliable value as it falls directly within the characteristic distances of the measured q -range. The contribution from the length is minimal within the measured q -range, so

changes in L have only minor effects on the simulated scattering. For the Guinier component, the results suggest a $R_g = 1.1$ nm. This value is consistent with the theoretical size of CU-based off mass-density calculations.

Unlike Figure 3.22 and Figure 3.23, the final fit spans a limited q -range, between 0.3 to 3 nm⁻¹, and does not account for the bookends because the fits begin to deviate. Though it was not possible to fully confirm the reason, there are some hypotheses that reasonably explain this behavior and why the fitting results are still sound.

In the low- q region, a larger characteristic length d is measured which means that the contributions of the length and radius to the intensity become more important. In the fitting region, length changes up to a factor of eight yield no discernible change in scattering pattern but at the lower q the model will be highly sensitive to length changes while changes in the thickness will have a minimal impact on scattering intensity. If the length has a high polydispersity the features will cause a deviation from the model as features are smoothed out. A second possible reason for the deviation could be if certain behaviors of the microbubbles extend to the submicron bubbles in the same way the shape morphology translates.

In the optical microscopy images the cylindrical bubbles are not completely rigid as they can bend and sometimes have kinks (Figure 3.10). This behavior would not influence the fit as the q -range is mainly probing the cross-section of the cylinder, but at the low q section these “bends” and “kinks” would become more influential to scattering intensity. For the high q data, the characteristic lengths are related to $0.9 < d < 2.1$, which are smaller than the size of an individual protein, so the behavior of the two peaks would not be

addressed by the current fitting models. Adding a third model was considered but discarded. As mentioned, these length scales are smaller than the protein so they may be related to the internal structure of CU; however, this is not the only possibility.

For modelling of this sample, the solution was considered a dilute solution so the structure factor $S(q) = 1$. This assumption is valid only by treating the solution as a two-population system; (1) free CU proteins in solution and (2) solid cylindrical bubbles. If the approximation of solid cylindrical bubbles is replaced by the more accurate representation of assembled proteins creating a bubble film the structure factor $S(q) \neq 1$ for the cylindrical core-shell model. The new equation for the scattering intensity model would become

$$I(q) = p_1 S(q)_{CU \text{ interactions}} P(q)_{core-shell \text{ cylinder}} + p_2 P(q)_{Guinier} \quad (43)$$

where $S(q)$ is the structure factor from the interaction between proteins in the bubble film.

Currently there is no information in the literature about the packing orientation of CU proteins in bubble films so choosing a model would be difficult. Also, the scattering intensity in this region may not be fully from either the internal structure of the CU protein or the packing of the CU in the film but a mix of both. Finally, modelling this high q intensity would have no impact on the calculation of the bubble film thickness, the goal of the experiment. At this time, there is simply no reason to attempt modelling of this phenomena though it could be considered for future work.

3.8.4 Atomic Force Microscopy

Modelling SAXS solutions is a difficult process requiring multiple assumptions and complex modelling, especially for a two-population system. While the conclusions are

reasonable and defensible, the best scientific practice is to use multiple characterization techniques to increase certainty. AFM is another possible characterization technique to measure bubble thickness.

As with all characterization methods, AFM has strengths and drawbacks but it complements SAXS by creating inverse mirrors of one another. For AFM measurements, bubbles are measured individually, and there is always the possibility for outliers to skew results. In SAXS modelling, the result is an average of all particles in the scattering volume, which measure several orders of magnitude more bubbles. The advantage of using AFM is less complexity, a more direct method of measurement, and a non-reliance on modelling that requires multiple assumptions. The premise of the AFM work is built on the hypothesis that by drop-casting an agitated cerato-solution onto a silica substrate, the water would evaporate and over time the bubbles would collapse upon itself as the air escaped. The resulting collapsed bubble would have a height twice the film thickness so a height profile measurement would give the bubble thickness. From the images, this hypothesis is correct—surprisingly, however, not all bubbles deflated after evaporation. This does not prevent the measurement of film thickness but does provide a further example of CU's excellent strength properties.

It is important to note one assumption. The measured bubbles in AFM are on the microscopic scale in Figure 3.25, not the submicron bubbles measured during SAXS. This requires an assumption that bubble film thickness is not dependent on the overall bubble size for any declaration of bubble film thickness. No current evidence conflicts with this assumption but there is also no clear evidence in support. An indirect case could be made that because the bubble morphology of a cylindrical bubble is conserved across length

scales, the bubble thickness would be conserved as well. Along with the experimental technique constraints, it is a reasonable assumption to adopt without any existence of conflicting evidence.

The key results from the AFM work are in Figure 3.25. Graphs A and B are single height profiles across bubbles in images C and D, respectively. Height profiles were created with line cuts using the NanoScope® analysis software. The inflated bubbles were 204 ± 28 nm in height using the average of five line cuts. The collapsed bubbles measured 27 ± 2 nm using the average of 19 linecuts; assuming that this height represents two bubble membrane layers (top and bottom) a single membrane would have a thickness of 14 ± 1 nm, which is 5 times larger than the 2.8 nm diameter of the protein from SAXS measurements. An odd number of proteins results in a hydrophilic exterior and hydrophobic interior.

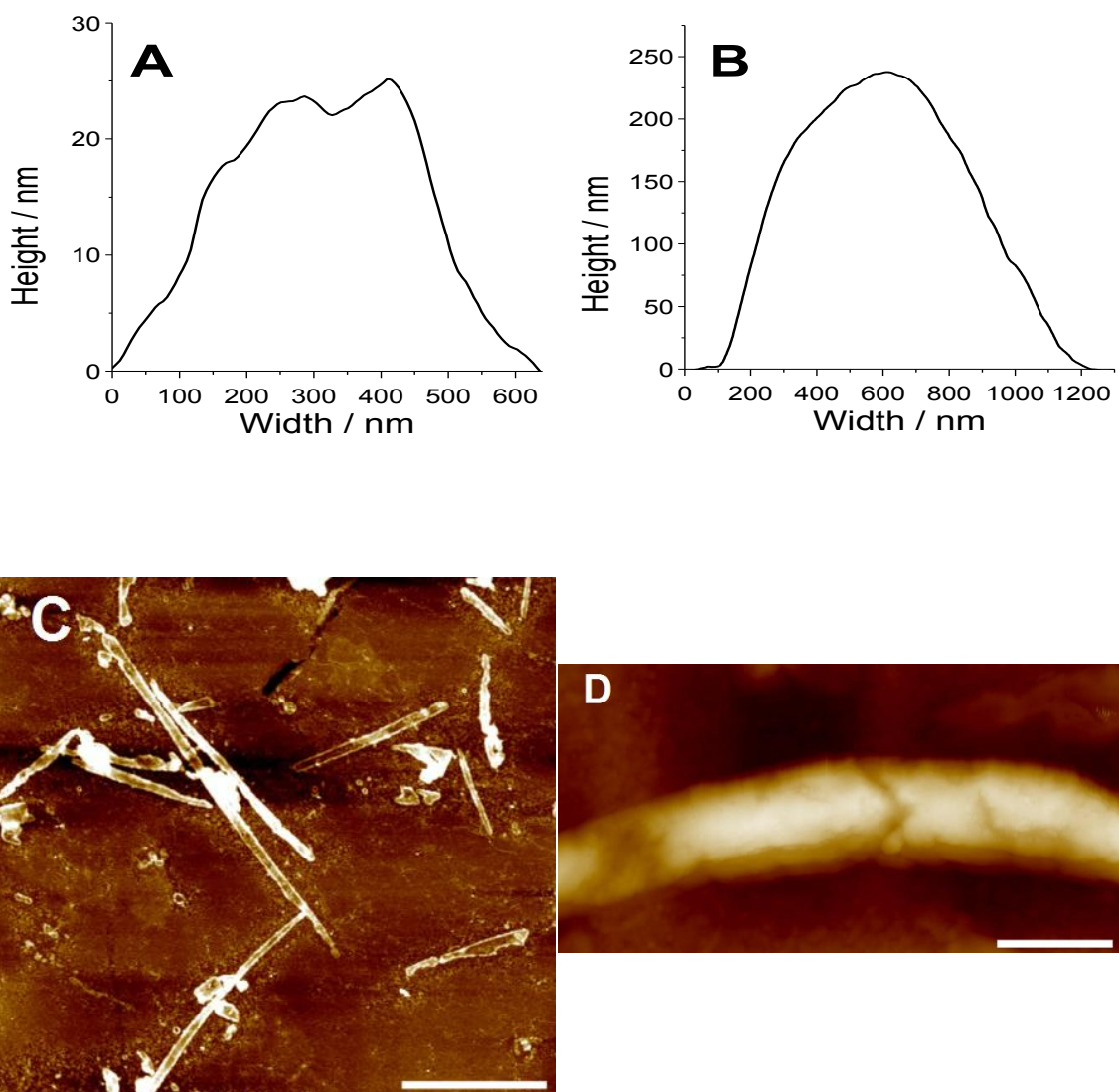


Figure 3.25. Cerato-ulmin $c = 2$ mg/mL AFM images and height profiles for inflated and deflated bubbles: (A) single height profile across a collapsed bubble; (B) single height profile across an inflated bubble; (C) AFM image of collapsed bubbles (scale bar = 5 μm); (D) AFM of zoomed in on one bubble (scale bar = 1 μm).

3.9 Conclusions

The thickness of CU bubbles across the size spectrum was measured. Optical microscopy calculations provided a rough estimate of film thickness that aided in SAXS modelling. Experiments completed at ORNL provided a possible structure of the protein using the ATSAS suite of programs. Finally, use of SAXS and AFM permitted construction of a model of the cylindrical submicron bubbles. The SAXS pattern was fit with a two-population custom model that features free CU proteins in solution and cylindrical bubbles with a thickness of 13.6 ± 3.2 nm and outside diameter of 69 ± 3.2 nm. For the larger bubbles, AFM measured the thickness of the film at 14 ± 1 nm. Using the protein size derived from the SAXS scattering of the free proteins in solution from the Guinier contribution, the bubble film is five proteins thick. Figure 3.26 shows the proposed cross-sectional morphology of the persistent, submicron bubbles.

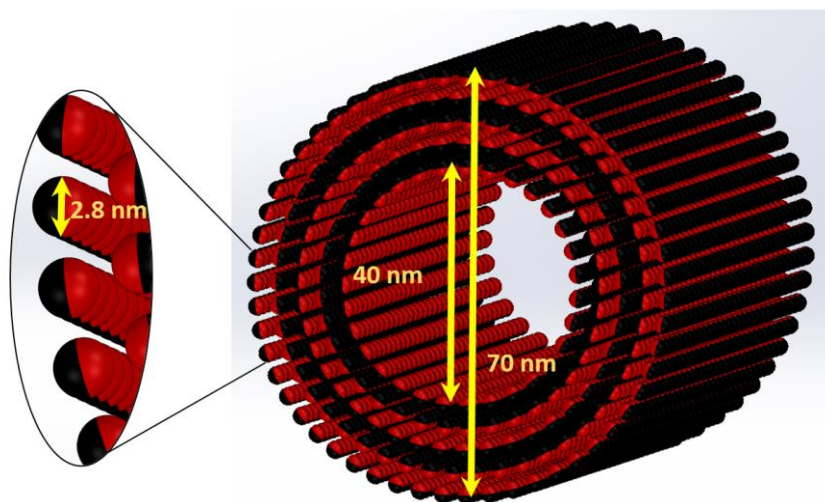


Figure 3.26. Suggested shape of cerato-ulmin cylindrical bubbles. The bubble has an inner diameter of 40 nm and outer diameter of 70 nm with a five-protein thick film with alternating hydrophobic and hydrophilic patches from the CU proteins. Take with permission from reference 97.

While Figure 3.26 shows the individual CU proteins as spheres, the SANS results in Figure 3.11 show the CU in an elongated structure. The discrepancy is due to the unknown orientation of the elongated structure in the bubble film. It is not known whether the hydrophobic patch is on the side or end of the cylinder, so it is unclear how it orients. Because the hydrophobic patch orientation is unknown and to avoid unsubstantiated claims, the suggested shape uses a simple spherical approximation of the CU in the film. The packing structure of the CU in the film along with the CU conformation could be addressed in future work.

CHAPTER 4. BUBBLE CREATION THROUGH STANDARDIZED AGITATION

4.1 Introduction

As described in the previous chapters and all published literature, CU bubble dispersions assemble from agitating a solution by hand. Agitation creates a spectrum of sizes—large bubbles are visible by eye and smaller ones are observable under a microscope or measurable using DLS. The method of agitation also influences the ratio of spherical to nonspherical bubbles and number density of the size distribution. The optimal method for creating the long cylindrical bubbles seen in Figure 2.6 is gently agitating a glass vial in a figure-eight motion with a small amount of CU solution. As expected, there are large disparities in bubble dispersions as some researchers excel at the precise motion and its repeatability. Even the most skilled researcher will never be able to fully duplicate their exact motions of agitation. This hinders studies on the formation of the CU bubbles and the effect of agitation conditions.

This chapter addresses the lack of reproducibility in agitation and examines the effect of agitation on microscopic CU bubble formation. By designing and constructing a wave tank apparatus with mechanical agitation the microbubbles are created by a customizable, reproducible method. After agitation at various conditions the microbubbles are examined with optical microscopy. Because the experimental variable is agitation, optical microscopy must be completed at the wave tank apparatus, which requires the addition of a custom-built horizontal microscope for imaging.

The final design uses a scotch yoke mechanism to drive a platform holding the miniature wave tank, horizontal microscope, and camera. The engine drives a periodic motion of the platform to create controlled waves depending on the frequency and amplitude of the motion. In addition to examining the effect of motion on bubble formation, a pressure control on the wave tank permits examination of the effect of pressure on bubble formation.

Results show that the hypothesis of reproducible and consistent agitation creating uniform bubbles is false because the sloshing tank creates a distribution of bubble sizes. The number density of bubbles with respect to size is steady until a sharp decrease at the maximum bubble size. The maximum bubble size is frequency dependent, with higher frequencies creating larger bubbles. The estimated work done by the bubble at the kink is 14 pJ.

4.2 Bubble Formation

The three main mechanisms for the formation of microbubbles are: microfluidic devices,¹⁴²⁻¹⁴⁴ sonication,¹⁴⁵⁻¹⁴⁶ and mechanical agitation¹⁴⁶⁻¹⁴⁸. In a microfluidic device gas is injected in a flowing solution to create bubbles. These devices create bubbles with the least polydispersity among the three methods and bubble size is controlled by gas injection rate and duration, liquid flow velocity, channel widths, and capillary dimensions. Historically, the drawback to microfluidic systems has been bubble production because bubbles are created individually, unlike sonication or mechanical agitation where a bulk solution is acted upon and bubbles form throughout the solution. Recent improvements in

manufacturing have led to large-scale production with systems able to produce roughly 10^{11} bubbles per hour with diameter $<100\text{ }\mu\text{m}$ and $<5\%$ coefficient of variation.¹⁴³

The second common method for microbubble generation is sonication. In this process, ultrasound waves with frequencies $>20\text{ kHz}$ create cycles of high and low pressure in a solution. If pressures are low enough during these cycles, cavitation inception will occur. This is when the pressure is low enough that the liquid ruptures to create a cavity. The pressure in the gas cavity is low so the bubble quickly collapses. During this collapse the bubble shrinks in size creating a massive jump in pressure and temperature to greater than 10,000 bar and 3,000 K, respectively.¹⁴⁹ The energy output of cavitation during sonication provides a way to agitate solutions and speed dissolution of solids, mix different solutions, remove contaminants from a surface, create emulsions, and degas liquids. Unfortunately, it can also break macromolecules.

For microbubble generation, cavity inception occurs but many solutions have surfactants or proteins that prevent bubble collapse. When the bubble begins to shrink the resulting energy induces cross-linking between the surfactant molecules or proteins and solidifies the bubble. For most protein microbubbles, the reaction is interprotein disulfide cross-linking between cysteine residues.¹⁵⁰⁻¹⁵¹ This explains why CU does not form microbubbles when sonicated while other proteins do. The CU molecule only contains eight cysteine residues already linked by four disulfide bonds. These disulfide bonds are in the center of the protein, maintaining its stability, and would not be exposed to other proteins.¹³

CU bubbles will form through less violent methods of mechanical agitation or microfluidic devices. The final method for microbubble generation is mechanical agitation. This does not have the same energy output as sonication but produces hydrodynamic cavitation because fluid flow creates local areas of low pressure.

4.3 Wave Dynamics

The study of water waves is an immense field drawing researchers from disciplines such as physics, biology, mathematics, and engineering. The applications and interests range from understanding the underlying mathematics to designing structures to prevent coastal erosion that creates billions of dollars of economic loss. With so much interest and financial incentive it is no surprise that there are multiple experimental instruments to create different types of waves and fluid flows. Most instruments consider large phenomenon such as ocean waves, so tanks may range from table-top size to those larger than a football field holding millions of gallons of water.

There are three categories of wave tanks: ripple tank, wave basin, wave flume. Ripple tanks are very shallow with large surface area. The agitations are small and create capillary waves whose behavior is governed mainly by the surface tension of the fluid. These are commonly used for demonstration of fundamental wave physics. Because capillary waves are small and not the main contributor to the overall fluid flow of a CU solution agitated by hand in the current cells, the ripple tank is not an ideal choice.

The wave basin tanks have similar length and width. They are ideal for simulating waves in deep water. They are commonly used to test a ship's resistance to capsizing or an oil rig's response to storms. More recent wave basins are circular and produce waves in all

directions to mimic stormy seas.¹⁵² This design is also not ideal for the current experimental goals because the 3D flow and multi-directional wave production create unnecessary complexities and variables.

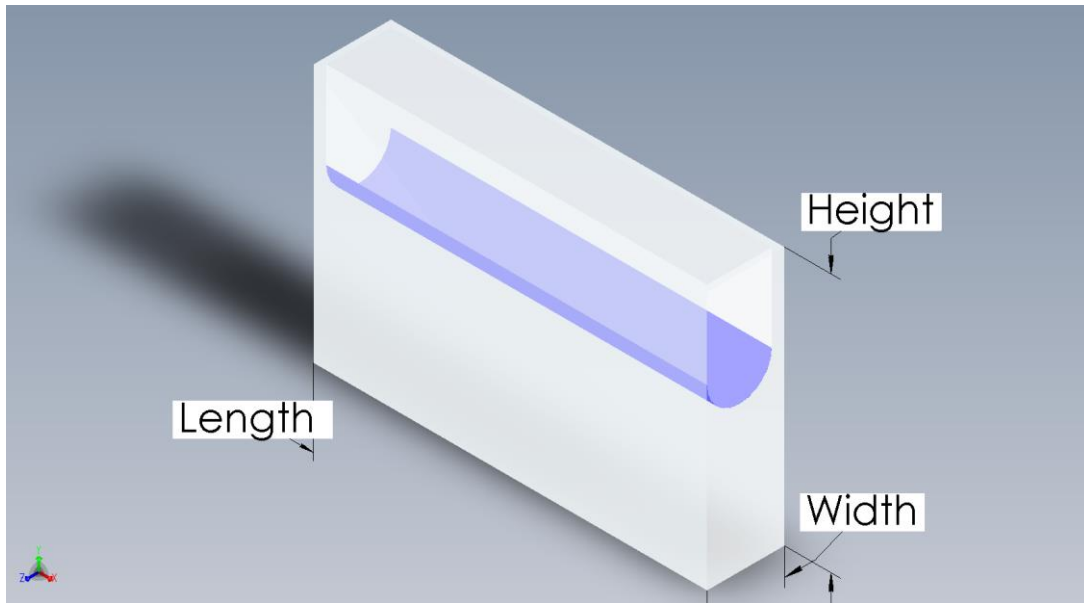


Figure 4.1. A wave flume has a small width and large length which allows for fluid flow to be considered two-dimensional

The wave flume has a longer length than width (Figure 4.1). This allows for waves to be considered as a two-dimensional system because cross-directional flow is negligible. By confining the flow to two dimensions, it is possible to create different categories such as periodic, standing, traveling, solitary, and tsunami-like waves. The wave flume is the optimal choice of wave tank for these experiments due to its flexibility of different wave types and reduction from a three-dimensional to a two-dimensional system. Creating regular, well-behaving surface waves is also easiest in a wave flume.

Surface waves propagate at the interface of two interfaces with a 90° angle between the amplitude and propagation vectors. Common examples are radio ground waves,

electromagnetic radiation along an index of refraction gradient, and ocean waves. Because CU forms a bubble dispersion in water, this work only focuses on water waves.

There are multiple analytical expressions for the flow velocity of water waves, all requiring some measure of assumptions. The most suitable method to describe basic behavioural flow is the Airy wave theory. It is a linear expression for the flow field of a homogeneous, inviscid, incompressible fluid in a container with a uniform mean depth. Figure 4.2 shows a diagram of regular surface waves in a wave tank seen from the side. The rectangular shape and small width are optimal for creating regular surface waves.

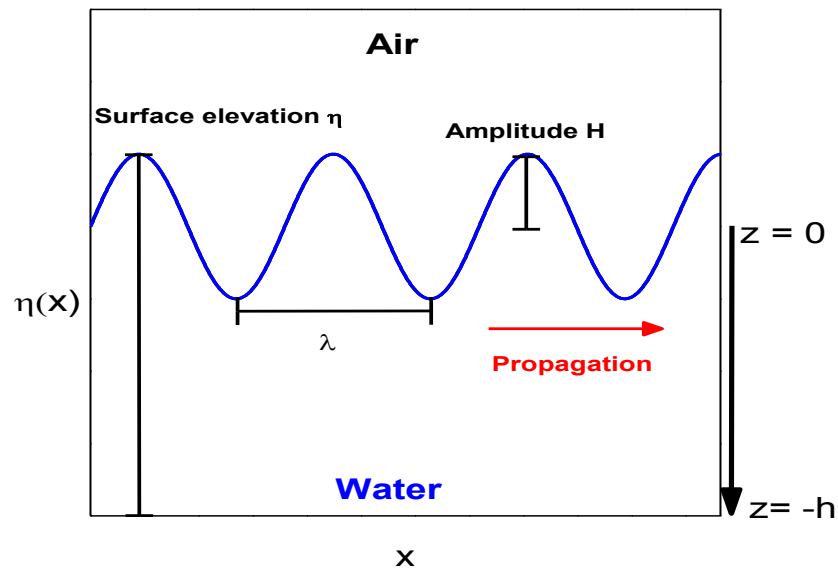


Figure 4.2. Diagram of regular surface waves at the air-water interface with key variables. For a tank with a flat bottom and small width, fluid flow can be modeled with Airy wave theory.

By applying these assumptions and factoring in the correct boundary conditions it is possible, in certain cases, to solve for the flow field in a wave tank. In a closed wave tank

with the air and water being treated as incompressible and inviscid fluids, the continuity equation simplifies and the divergence of the fluid velocity field becomes zero.

$$\frac{\partial \rho}{\partial t} + \nabla \cdot (\mathbf{u}) = 0 \quad (44)$$

$$\nabla \cdot \mathbf{u}(x, z) = 0 \quad (45)$$

where t is time, ρ is density, u is the velocity of water in the x direction, x is the horizontal direction, and z is the vertical direction. Assuming an irrotational flow and introducing the scalar potential ϕ where $\mathbf{u} = \nabla \phi$, the continuity equation becomes

$$\frac{\delta^2 \phi}{\delta x^2} + \frac{\delta^2 \phi}{\delta z^2} = 0 \quad (46)$$

which is the Laplacian equation.

Assuming a long wave tank, solving for the flow field still requires boundary conditions for the surface of the water and bottom of the tank. The first boundary condition is at the bottom of the tank where the fluid velocity is zero

$$u(x, z = -h, t) = \frac{\partial \phi}{\partial z}(x, z = -h, t) = 0 \quad (47)$$

where h is the mean water depth. The second boundary condition assumes that the water molecules at the surface stay at the surface elevation of the water η

$$\frac{\partial \eta}{\partial t} = \frac{\delta \phi}{\delta z} \text{ at } z = \eta(x, t) \quad (48)$$

This equation is the kinematic boundary conditions. Using these boundary conditions, the velocity potential solves for

$$\phi(x, z, t) = \frac{ag}{\omega} \frac{\cosh(k(z + h))}{\cosh(kh)} \cos(\omega t - kx) \quad (49)$$

$$a = \frac{\omega}{g} C_1 \cosh(kh) \quad (50)$$

where g is the acceleration of gravity, ω is the frequency, k is the wavenumber, and C_1 is a constant.

Because the velocity is the derivative of the velocity potential it may be integrated with respect to x or z to arrive at

$$v_x = A \sin(\omega t) \quad (51)$$

$$v_z = B \cos(\omega t) \quad (52)$$

where v_x and v_z are the fluid velocities and A and B are

$$A = \omega a \frac{\cosh(k(z + h))}{\sinh(kh)} \quad (53)$$

$$B = \omega a \frac{\sinh(k(z + h))}{\sinh(kh)} \quad (54)$$

By integrating these with respect to time, the fluid trajectory in the water wave is

$$x_p = -\frac{1}{\omega} A \cos(\omega t) \quad (55)$$

$$z_p = \frac{1}{\omega} B \sin(\omega t) \quad (56)$$

where (x_p, z_p) is the position of the particle. This finally simplifies to

$$\frac{x_p^2}{(A/\omega)^2} + \frac{z_p^2}{(B/\omega)^2} = 1 \quad (57)$$

which is the equation for an ellipse. Therefore, a particle's trajectory in the water will follow an elliptical orbit. In the case of deep water, $A=B$ so particles travel in a circular orbit with radius ae^{kz} .

Insights arising out of these results include the connection between ω and k and dispersion relation. If the Bernoulli equation for an unsteady flow with the current assumptions

$$\frac{\partial \phi}{\partial t} + g\eta = 0 \quad (58)$$

is combined with the kinematic boundary condition, the result is

$$\frac{\partial^2 \phi}{\partial t^2} + g \frac{\partial \phi}{\partial y} = 0 \quad (59)$$

By inserting the velocity potential and simplifying, the equation yields the dispersion relationship

$$-\omega^2 \cos(kh) + gk \sin(kh) = 0 \quad (60)$$

$$\omega^2 = gk \tanh(kh) \quad (61)$$

The consequence of this relationship is the link between the frequency ω and wavenumber k . For each wavelength λ the only possible frequencies are ω and $-\omega$ where the negative sign references the direction the wave travels. Given the relationship between other wave characteristics, this causes wave frequency, wavelength, wavenumber, period, and phase velocity to be interconnected.

Another insight comes from taking the specific case of deep water or short wavelengths where $h \geq \frac{\lambda}{2}$. At large h , the dispersion relationship simplifies to $\omega = \pm\sqrt{gk}$ because $\tanh(kh) \rightarrow 1$. Additionally, the cosh term in the velocity potential is reduced to

$$\frac{\cosh(k(z+h))}{\cosh(kh)} = \frac{e^{kz}e^{kh} + e^{-kz}e^{-kh}}{e^{kh} + e^{-kh}} = e^{kz} \frac{1 + e^{-2(z+h)k}}{1 + e^{-2hk}} \quad (62)$$

Near the surface of the water, this term simplifies to e^{kz} so the velocity potential reduces to

$$\phi(x, z, t) = \frac{ag}{\omega} e^{kz} \cos(\omega t - kx) \quad (63)$$

and the velocities in the x and z directions are

$$\frac{\partial \phi}{\partial x} = v_x = a\omega e^{kz} \sin(\omega t - kx) \quad (64)$$

$$\frac{\partial \phi}{\partial z} = v_z = a\omega e^{kz} \cos(\omega t - kx) \quad (65)$$

Consequently, the velocity decreases exponentially as depth increases due to the e^{kz} term. At $z = \frac{\lambda}{2}$ the velocity decreases by a factor $e^{-\pi} \sim 0.043$ and is only 4.3% of the velocity at the surface. By $z = \lambda$, the velocity is less than 1% of the magnitude at the surface. To summarize, in deep water particles travel in a circular orbit with radius ae^{kz} at a constant speed ωa at the surface and a speed decreasing exponentially by e^{kz} .

The behavior for the case of shallow water where $\frac{h}{\lambda} < \frac{1}{20}$ also can be further explored. In shallow water, $kh \ll 1$ and $\tan(kh)$ reduces to $\sim kh$ because of the small-angle approximation; then the dispersion relation reduces to $\omega = \pm k\sqrt{gh}$. The trajectory of particles is an ellipse with

$$a = \frac{H}{kh} \quad (66)$$

$$b = H\left(1 + \frac{z}{h}\right) \quad (67)$$

where H is the amplitude of the wave. As particles increase in depth the semi-major axis a is constant while the semi-minor axis b decreases linearly until reaching zero. A summary of the orbital trajectories for shallow, intermediate and deep water is shown in Figure 4.3.

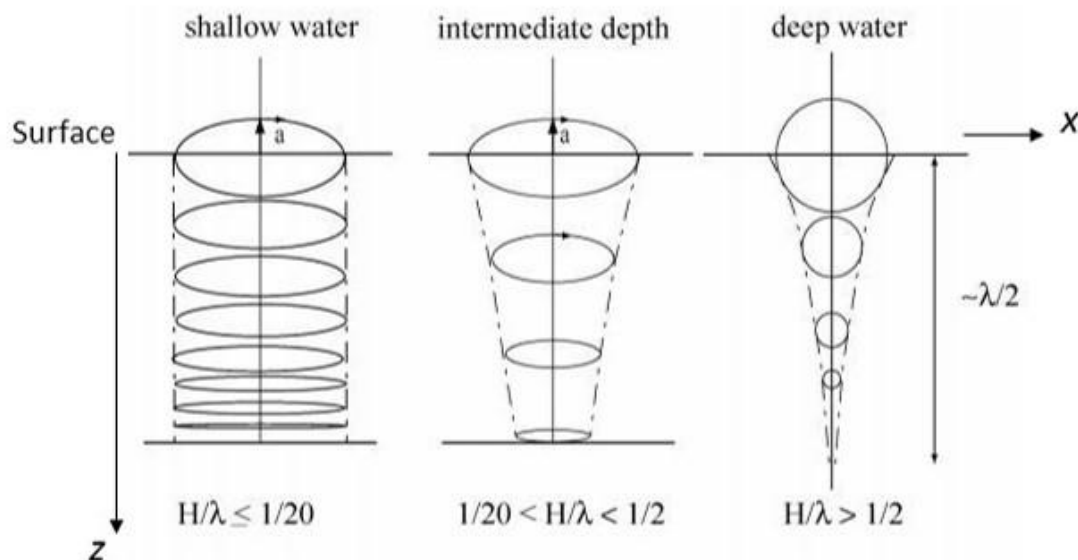


Figure 4.3. Orbital motion of particles in a wave with shallow, intermediate, and deep depths. Adapted from reference 153.

Transitioning to the application of the theory, bubble dispersions currently are created by agitating a CU solution by hand in a glass vial that is held vertically and gently rocked in a figure-eight motion. This method creates the best number and uniformity of cylindrical bubbles compared to a more vigorous or vertical agitation. As the agitation deviates further from the figure-eight motion, the cylindrical bubbles that form decrease in number and length. Eventually the bubbles will be a mix of spherical and aspherical shapes with a very small amount similar to the bubbles seen in Figure 2.6. This suggests that the method of agitation and fluid flow affects the number, shape, and size of the cylindrical bubbles.

It is currently unproven that the figure-eight motion is the optimal method for generating cylindrical bubbles, but it is certainly effective. One hypothesis is that this method creates surface waves that are most conducive to forming the cylindrical bubbles due to their circular or elliptical flow field. Considering the orbital motions of particles in an Airy water wave it is possible that the circulatory motion for waves with $h \geq \frac{\lambda}{2}$ may be the best conditions for creating the cylindrical bubbles as the CU particles are constantly “rolling over”. This effect has also been seen with other films at the air-water interface.¹⁵⁴

4.4 Experimental Apparatus

Wave tanks use a variety of methods to generate waves including flap paddles,¹⁵⁵ horizontal pistons, vertical plungers,¹⁵⁶⁻¹⁵⁷ acoustic impulses,¹⁵⁸ and horizontal excitations¹⁵⁹. Each method has corresponding numerical calculations to predict the resulting flow fields.^{156, 160-163}

While the theoretical models continue to hold, constructing a system for CU increases difficulty because of the small size requirements. Typical wave tanks may range from containing gallons to millions of gallons of water. Because of the scarcity of CU, the needed experimental apparatus requires the volume to be < 50 mL, less than 2% of the smallest conventional wave tank.

Other than the reduced size, two other key challenges the experimental apparatus must address are reproducibility and measurements. While reproducibility is not a problem when using microfluidic devices, the CU bubble dispersions used in experiments are created through mechanical agitation and require a separate solution to address the problem

of reproducibility. Since the bubble formation from mechanical agitation is due to the fluid flow, the system needs controlled variables with discrete measurements able to reproduce the same flow profile in the sample every time it is used. This immediately discounts agitation by hand as discrete measurements of motion would be impractical and make reliably reproducing movement near impossible. The optimal solution is building a mechanical agitator with strict controls. The second challenge is creating a method of measurement to evaluate the microbubbles that does not disturb the sample after agitation. If the sample is transferred to a new container or moved to a different instrument an additional source of uncertainty is added as any jostling could create new bubbles.

In succession, a vertical plunger, acoustic impulse, and horizontal excitation wave tanks were designed and built. The first two proved to be insufficient to meet the experimental needs. The horizontal excitation wave tank met all requirements for use. For all agitation iterations, parts were designed using a 3D CAD software (SolidWorks) before construction in the Georgia Tech Montgomery Machining Mall or the Glass Shop. Parts requiring machining were fabricated by the researcher, while glass material designs used professional glass blowers. In the machine shop, most parts only required a lathe and CNC mill.

4.4.1 Plunger-type Wave Tank

The first design was the plunger wave tank. This method used a wedge-shaped paddle moving vertically to create water motion. Different wave properties were created through the variation of wedge shape, frequency, and amplitude of movement. The first tank iteration was constructed with poly(methyl methacrylate) (PMMA) with internal

dimensions of $152 \times 6 \times 76$ mm with a volume of 35 mL when 50% filled with solution (Figure 4.4).

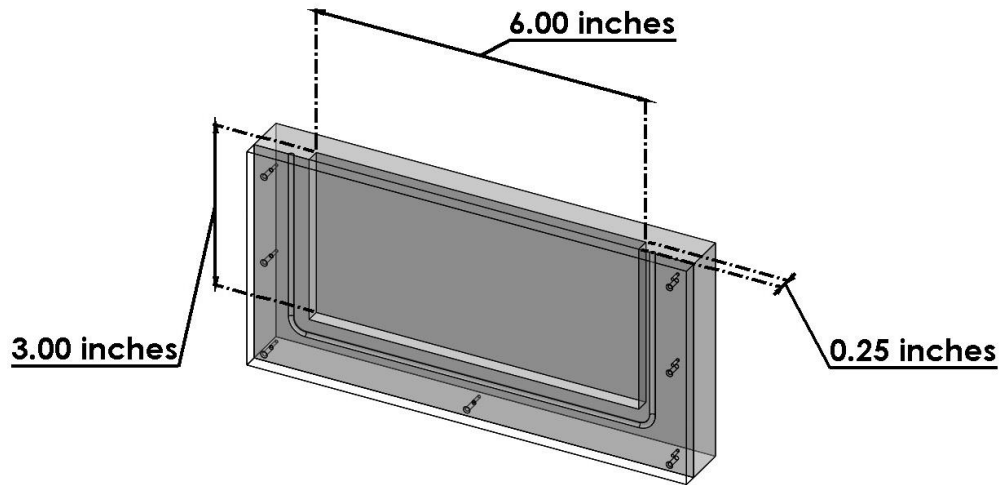


Figure 4.4. Wave Tank 1.1 was constructed of clear acrylic with internal dimensions of $152 \times 6 \times 76$ mm. When filled halfway, the tank holds 37 mL of CU solution.

A second and third tank (Table 4.1) were also constructed to use different amounts of solution.

Table 4.1. Three versions of wave tank for paddle type wave tank.

Wave tank	Width ^a (mm)	Volume at 50% capacity (mL)
1.1	6	35
1.2	13	75
1.3	3	17

^aThe length and height of tanks are all 152 and 76 mm, respectively.

All three tanks were assembled by screwing two plates together with a rubber gasket inserted to prevent leakage. For the solution to be considered as deep water according to the Airy theory, the wavelength must be $\lambda < 75$ mm due to the constraint $h > \frac{\lambda}{2}$. To satisfy the Airy conditions for shallow water the wavelength must be greater than 76 cm, which would be hard to satisfy in the current setup.

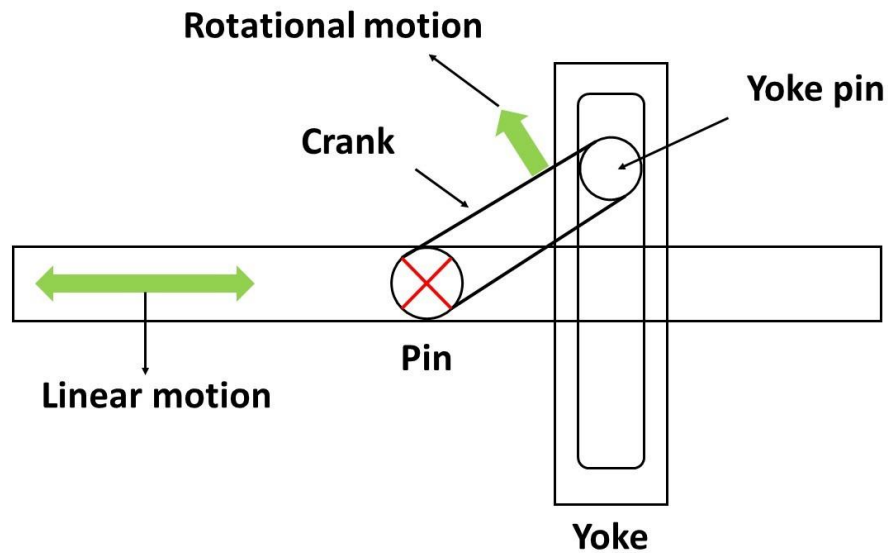


Figure 4.5. Scotch yoke engine mechanism. The crank's rotational motion creates a linear motion in the horizontal bar.

For this setup, the waves are created through a paddle being vertically driven in an oscillating motion. The mechanism chosen to drive the paddle is a scotch yoke engine (Figure 4.5), a mechanism that converts rotational motion to linear motion or vice versa. For a constant rotational speed, the linear motion is described as a sine wave with constant amplitude and frequency. In the figure, the amplitude is twice the length of the crank and the frequency will be sixty times the revolutions per minute (RPM).

The full assembly for wave tank apparatus 1.0 is in Figure 4.6. The mechanism looks different than the scotch yoke schematic in Figure 4.5, but the underlying principles are the same. A paddle is connected to a rod fixed with respect to the horizontal plane and only having range of motion in the z -direction. This rod is connected to the rotating disk through a crank connected to a pin. As the wheel rotates the pin moves the crank and creates the vertical motion. For this setup, the amplitude will be two times the radius of the pin.

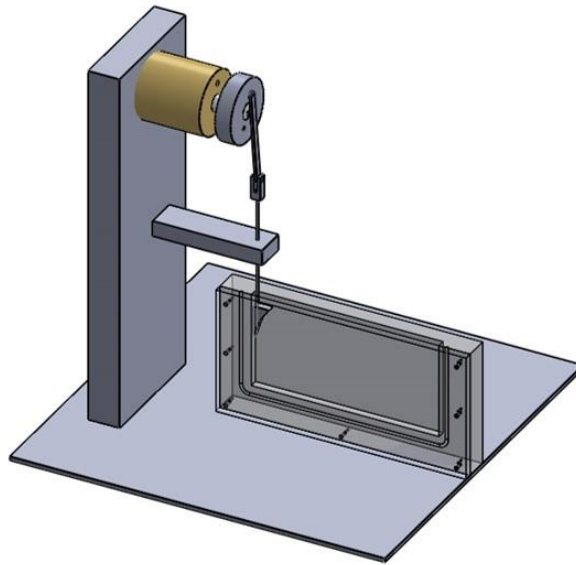


Figure 4.6. Wave tank assembly 1.0 uses a scotch yoke engine driving a paddle vertically to create water waves.

While the design is sound, the execution turned out to be impractical because there are other, easier methods to create this phenomenon with fewer complications. In conventional wave tanks, the ratio of the gap between the plunger and wall to the total plunger width can be $< 1\%$, which allows for flow to be considered solely two dimensional. For Wave Tank 1.1, a 1% ratio would have a $64\text{ }\mu\text{m}$ gap. The paddle, connecting rods, and

motor would only have 0.63° of free rotation with respect to the xy-plane before being constrained by the side walls. With respect to deflections with the vertical plane, there would only be 0.14° of freedom before striking the side walls. The central axis of the motor must be precisely aligned with the vertical with less than $250\text{ }\mu\text{m}$ of tolerance. It is possible to construct an apparatus with the necessary precision but it becomes impractical when much simpler options are available.

4.4.2 Acoustic Impulse Tank

The second design is an acoustic impulse wave tank. This design uses a modified surface transducer with one of the sides of the wave tank replaced with a latex membrane. The surface transducer has an amplitude of 1 mm with frequency ranges from 100 Hz to 15 kHz. This concept worked but did not produce any visible waves or bubbles. It is likely this method is too similar to sonication because no bubbles were formed.

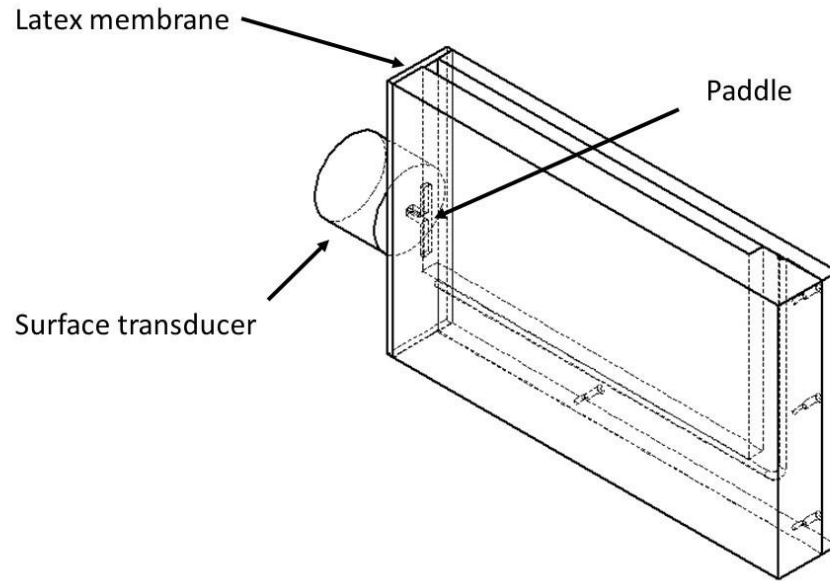


Figure 4.7. The acoustic impulse wave tank uses a surface transducer to drive a paddle against the latex membrane.

4.4.3 *Sloshing tank*

The final design used horizontal oscillation of the entire wave tank to create surface waves. Unlike the previous two versions, this setup required the entire tank to be in motion instead of a single component, which makes it the most complex system of the three. The motion was driven through a scotch yoke mechanism to create the necessary sinusoidal motion (Figure 4.8). A direct current (DC) permanent magnet motor was connected to a gear and pulley system to drive the rotation of a disk with an inserted pin. As the pin rotates it creates a sinusoidal linear motion in the x -direction with an amplitude of r for the connecting rod. By machining the disk with multiple insert locations for the pin with distances between radius $r = 1.3 - 31.8$ mm multiple amplitudes are possible to determine

optimum conditions. The frequency was measured with an Extech tachometer and converting the revolutions per minute (RPM) of the disk to the linear motion frequency by the relation $f = \frac{RPM}{60}$.

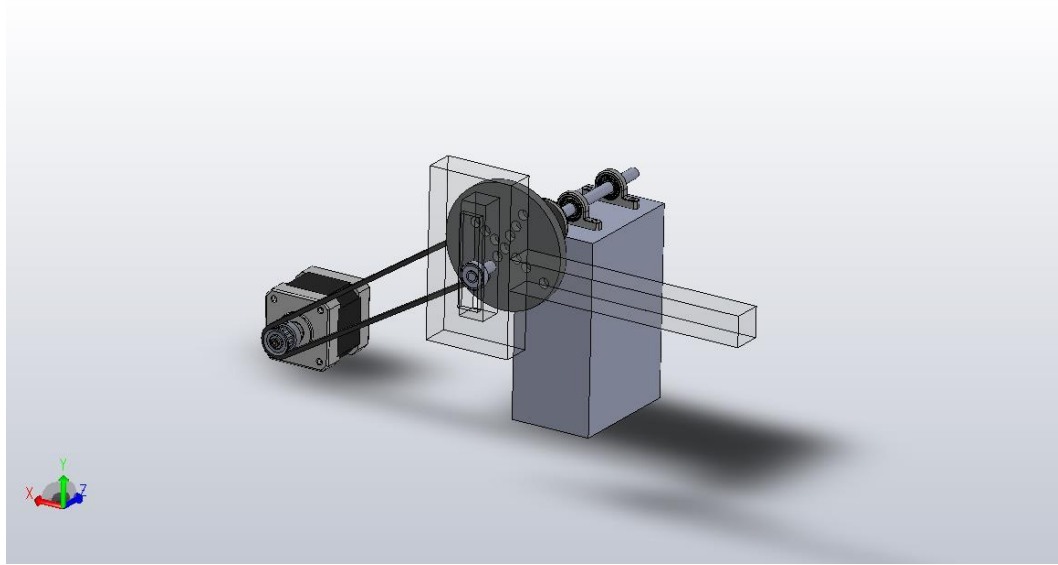


Figure 4.8. The scotch yoke mechanism for the sloshing tank used a gear and pulley system to drive rotation of the pin.

The scotch yoke engine was connected to a carriage plate mounted on eight horizontal v-shaped wheels that translate along two MakerSlide rail systems (Figure 4.9).

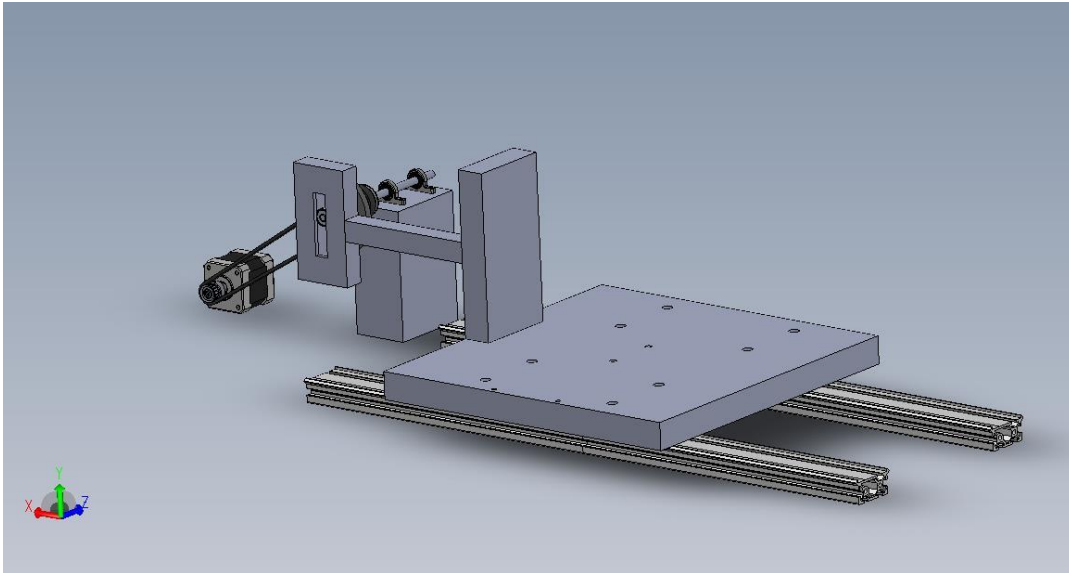


Figure 4.9. Scotch yoke engine connected to carriage plate connected to MakerSlides for slosh tank apparatus.

With the locomotive aspect complete, the next challenge was imaging the sample. With the requirement of not disturbing the sample, a horizontal optical microscope was built onto the carriage plate. The wave tank was then mounted on a three-dimensional translation stage bolted onto the carriage plate between the two microscope sections (Figure 4.10).

A 3MP CMOS camera is used and the resulting videos and pictures are analysed with AmScope software. Bubble motion calculations were completed with Tracker, a video analysis and modeling tool.¹⁶⁴

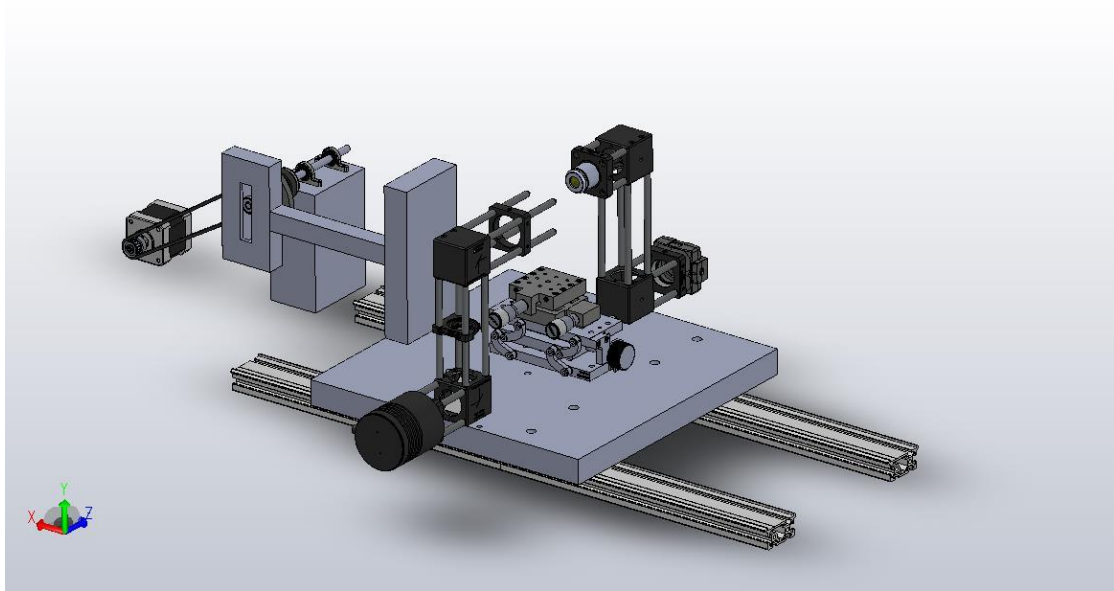


Figure 4.10. The full sloshing tank apparatus setup uses a scotch yoke engine connected to a carriage plate with a three-dimensional translation stage between a custom-built horizontal microscope.

In previous experiments, imaging of CU bubbles used small glass cells where the bubbles were vertically constrained by the glass wall. With this setup the horizontal microscope allows for tracking the bubbles' rise that was not previously possible. Figure 4.11 shows the shape of the meniscus in the wave tank; the focal point of the microscope was set to the midpoint of the wave tank walls.

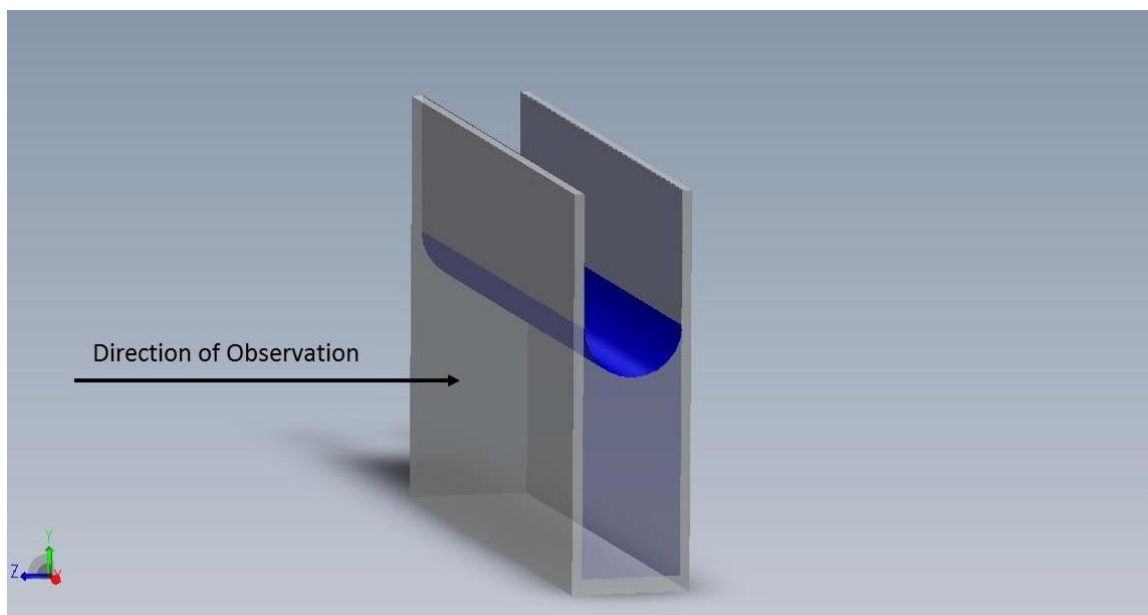


Figure 4.11. Attractive forces between the CU solution and the glass walls create a meniscus with the vertex at the midpoint of the glass walls.

Setting the focal point to the bottom of the meniscus was done by moving the sample to where there is a clear black line at the air/water interface (Figure 4.12). By setting the real image plane at the vertex of the meniscus the interaction between the CU bubbles and meniscus is visible.

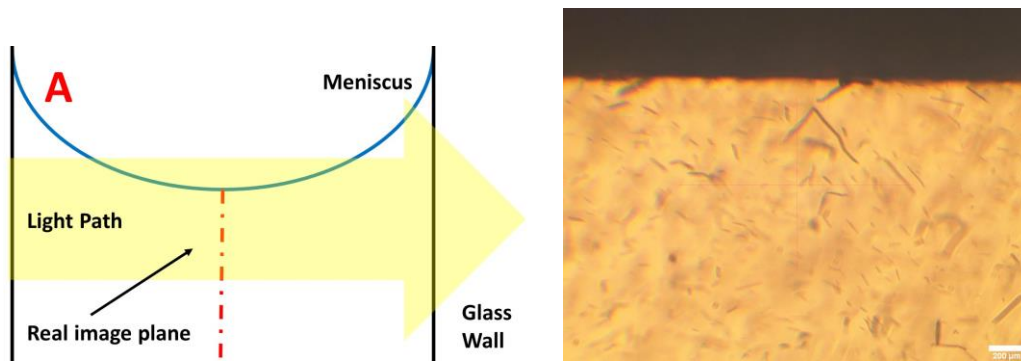


Figure 4.12. Microscope imaging of wave tank: (A) Schematic of wave tank setup with real image plane located at the vertex of meniscus (B) Resulting image from this schematic (scale bar = 200 μm).

By moving the focus off the vertex of the meniscus (Figure 4.13), the real image plane shifts to a higher point on the meniscus. The interaction between the CU bubbles and meniscus is obscured because of interference from light passing through the meniscus and air.

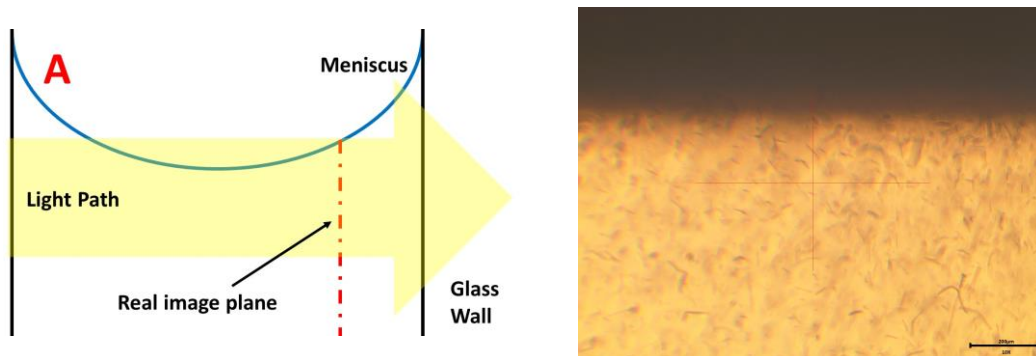


Figure 4.13. Microscope imaging of wave tank: (A) Schematic of wave tank setup with real image plane offset from the vertex of meniscus (B) Resulting image from this schematic (scale bar = 200 μm).

When the CU bubbles are created in the slosh tank and the tank position is at Figure 4.12 the out of focus bubbles will rise straight through the black line in the image as they

have not encountered the meniscus yet. Bubbles that appear focused are located on the real image plane and the interaction between the bubble and meniscus is observable.

4.5 Bubble Uniformity

As previously mentioned, bubbles created by hand agitation are not monodisperse in size or shape. This is expected because it is impossible to move the sample at constant speeds, velocities, and amplitudes. The beginning hypothesis of this chapter was that by using a reproducible, constant agitation the resulting bubbles would be uniform. Conditions were set to three different frequencies $f = 0.8, 1.5,$ and 3.5 Hz with an amplitude of 17 mm and a run time of $t = 30$ sec. After sloshing, images were captured every 5 minutes for 2 hours.

At the lowest frequency of 0.8 Hz no bubbles are formed and there is no difference between the unagitated and agitated sample (Figure 4.14A and Figure 4.14B). As the agitation frequency increases to 1.5 and 3.5 Hz bubbles are formed. Since the frequency is related to the velocity of the fluid in the tank this suggests there is a threshold frequency for creating bubbles.

Figure 4.15 shows the bubble number density for different agitation frequencies. As the agitation frequency increases, the time for the bubbles to rise out of the solution increases. The increased frequency creates bubbles at greater depths below the surface which take longer to rise out of the solution. This is confirmed after moving the viewing volume to greater depths through vertically adjusting the sample stage.

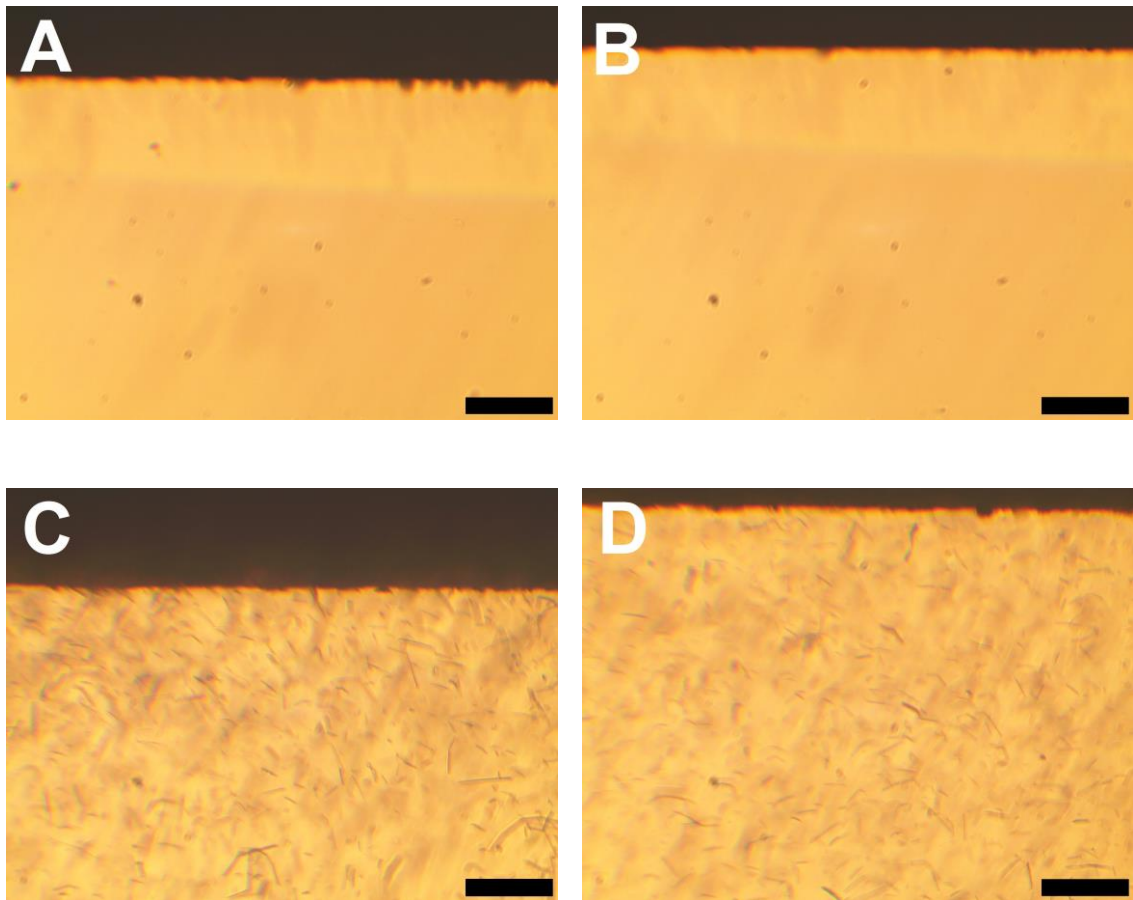


Figure 4.14. CU bubbles form in the wave tank with different agitation frequencies (scale bar = 200 μm): (A) No agitation; (B) 0.8 Hz; (C) 1.5 Hz; (D) 3.5 Hz.

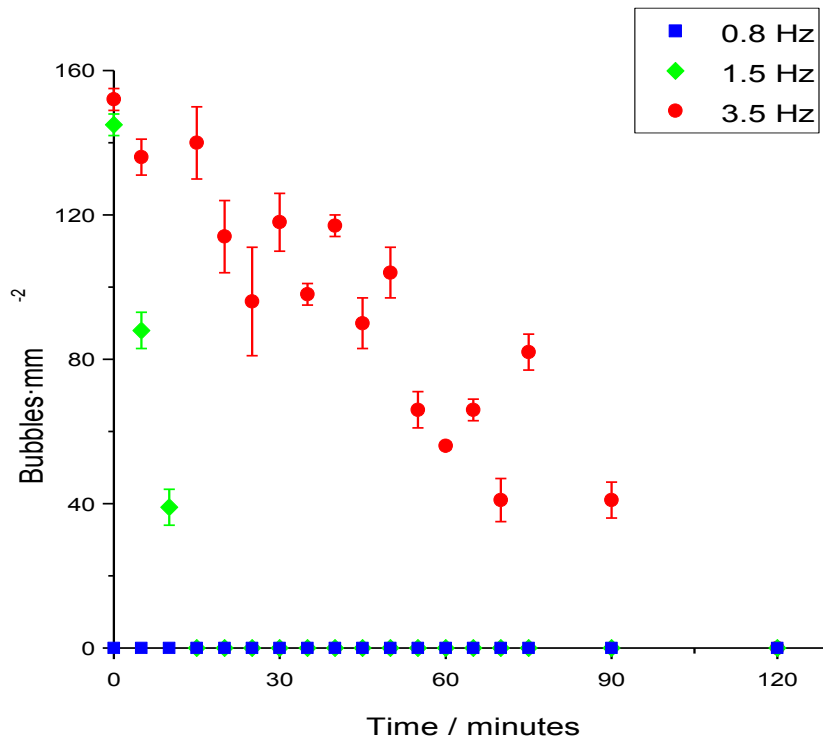


Figure 4.15. Bubble number density with different agitation frequencies.

Once the frequency is high enough to create bubbles there still exists a bubble size distribution like solutions agitated by hand in Figure 2.6. The size distribution was tracked over time for the 1.5 and 3.5 Hz agitations in Figure 4.16 and Figure 4.17. For the 1.5 Hz agitation, there are roughly an equal amount of bubbles $<75\ \mu\text{m}$ with a drop off at 75-100 μm after 5 minutes. The larger bubbles rise out of the solution after 10 minutes with only lengths $< 50\ \mu\text{m}$ remaining. After 15 minutes, all visible bubbles have risen out of solution leaving only the submicron bubbles.

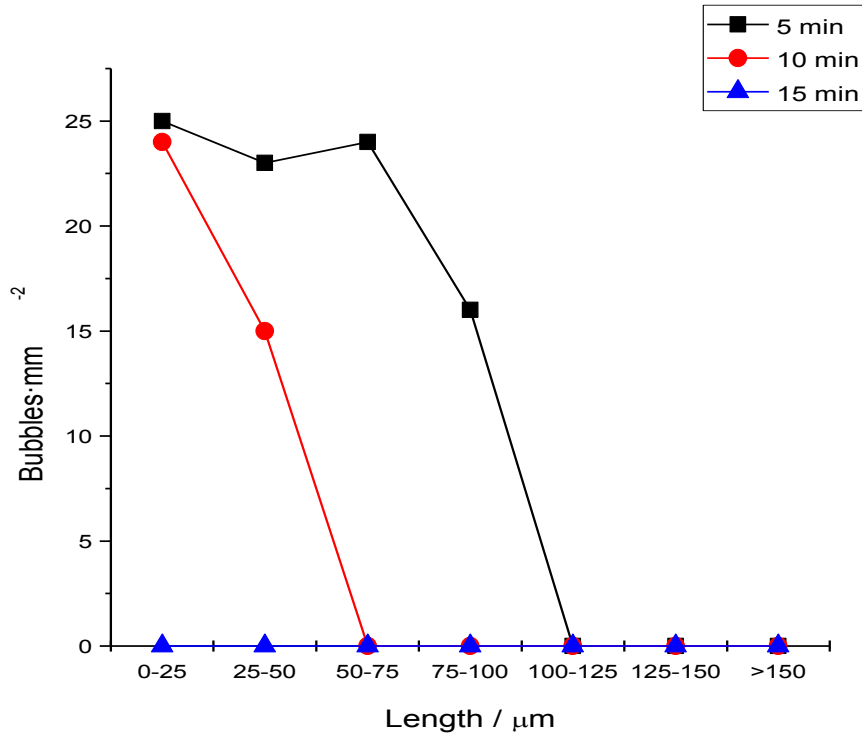


Figure 4.16. Bubble length distribution over time for $f = 1.5$ Hz agitation.

The bubble size distribution for the 3.5 Hz agitation in Figure 4.17 has a similar shape profile with the 1.5 Hz agitation run. The agitations created bubble distributions with similar number density with respect to size until a cut-off size where number density sharply falls off. In both instances the largest bubbles rise out of the solution first and over time the distribution shifts to smaller sizes until there are no visible bubbles left. The distributions over time between the two frequencies do differ in some ways. The higher agitation frequency created both larger bubbles and it took longer for all visible bubbles to rise out of solution as seen in Figure 4.15.

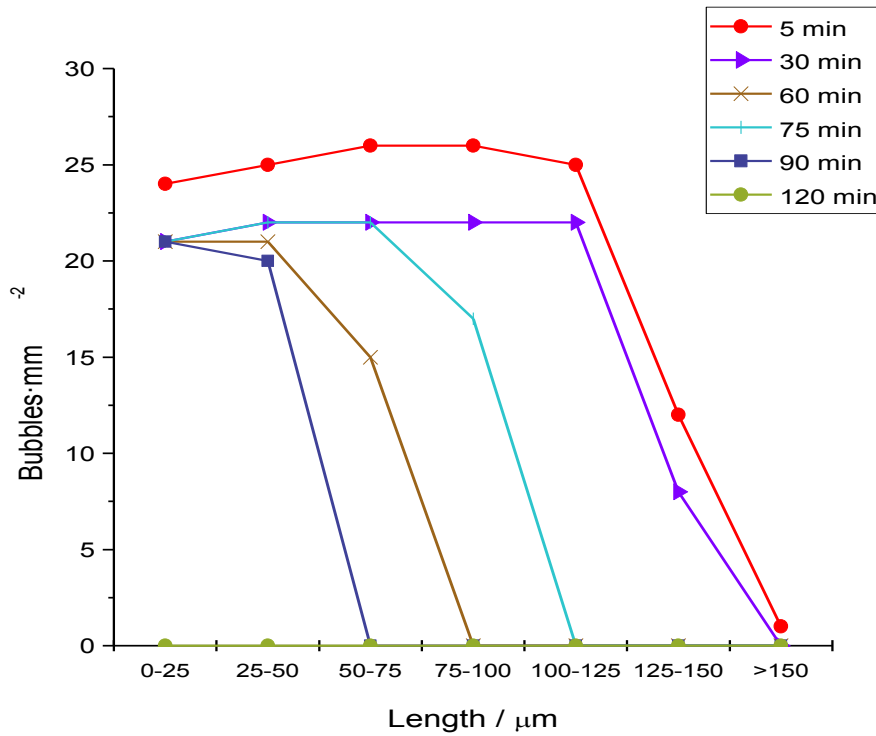


Figure 4.17. Bubble length distribution for $f = 3.5$ Hz agitation.

Examining the previous figures provides insights on the CU bubble formation. First, there is a critical fluid velocity to create bubbles since the 0.8 Hz agitation created no visible bubbles and frequency is related to the fluid velocity. Once a sufficient velocity is reached, bubbles form with larger bubbles forming at greater velocities. The velocity does not significantly influence the distribution of sizes as the bubble number density is 20-25 bubbles·mm⁻² for all bubble sizes and times before the cut-off as the distribution falls off. Because the bubbles are rising over time and the viewing depth is held constant, measurements over time are related to the bubble distribution at greater depths at initial conditions. The values in Figure 4.17 for the 0-25 μm lengths mean that those bubbles had similar number density through all depths during bubble formation. This number density is not fully constant though as video analysis does show the presence of bubble clusters

where the number density is increased by a factor of 2 but they are localized and infrequent. These results suggest that there is a minimum velocity to create bubbles. Above that threshold bubbles begin to form with velocity being the limiting factor on maximum size.

4.6 Bubble Mechanics

The hypothesized interaction between the CU bubbles and meniscus was the bursting of the CU bubble at the meniscus with the bubble film subsequently being incorporated into the CU film at the air-water interface. The strength of the film resulted in the CU bubble film acting like a solid. Figure 4.18 shows the reorientation of the cylindrical bubble as it contacts the meniscus. From particle tracking, the bubble contacts the meniscus at $200 \pm 11 \mu\text{m}\cdot\text{s}^{-1}$ and begins orienting parallel with the meniscus in $< 125 \text{ ms}$ and reaches alignment at $t = 3.6 \text{ s}$.

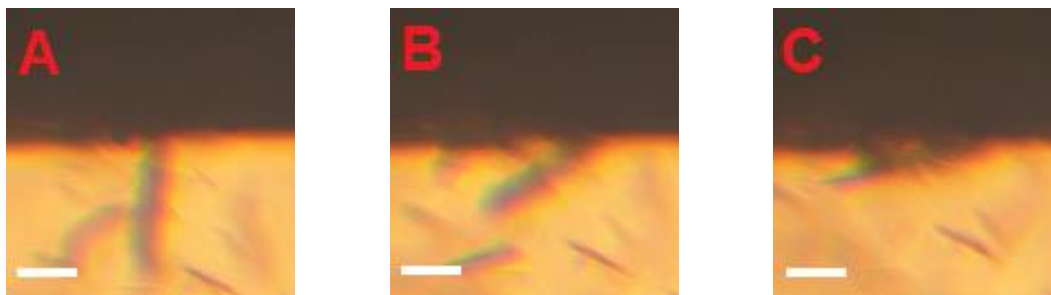


Figure 4.18. Cylindrical CU bubble reorienting parallel to the meniscus over time (scale bar 100 μm): (A) $t = 0 \text{ sec}$; (B) $t = 1.81 \text{ sec}$; (C) $t = 3.17 \text{ sec}$.

The strength of both the bubble and the film meniscus is further demonstrated in Figure 4.19 and Figure 4.20. In these figures, the vertex of a kinked or v-shaped bubble is stopped by the meniscus and the bubble bends and straightens over time as the ends continue to rise.

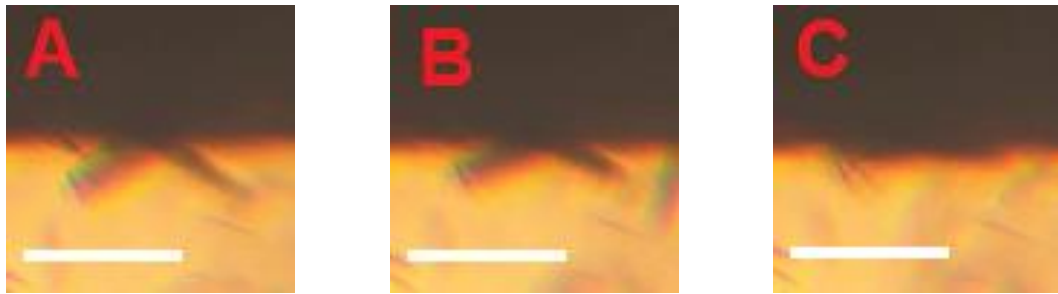


Figure 4.19. Bent CU bubble straightening over time (scale bar 200 μm): (A) $t = 0$ sec; (B) $t = 1.02$ sec; (C) $t = 1.47$ sec.

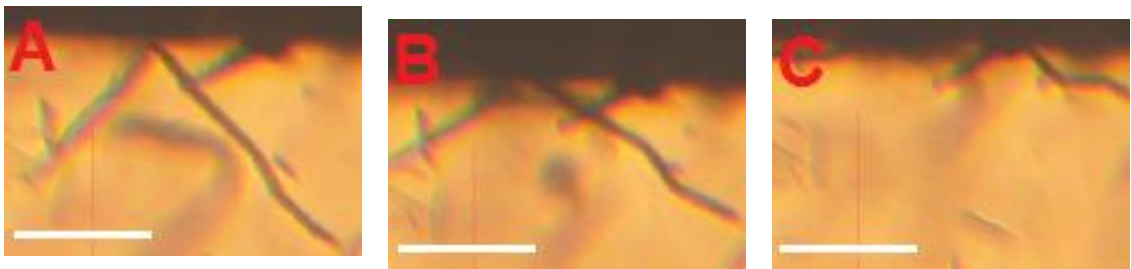


Figure 4.20. The kinked CU bubble straightens as it encounters the meniscus (scale bar = 200 μm): (A) $t = 0$ sec; (B) $t = 0.890$ sec; (C) $t = 2.247$ sec.

The straightening of the bubble in Figure 4.20 is further explored using video tracking. Figure 4.21 shows a diagram of the bubble.

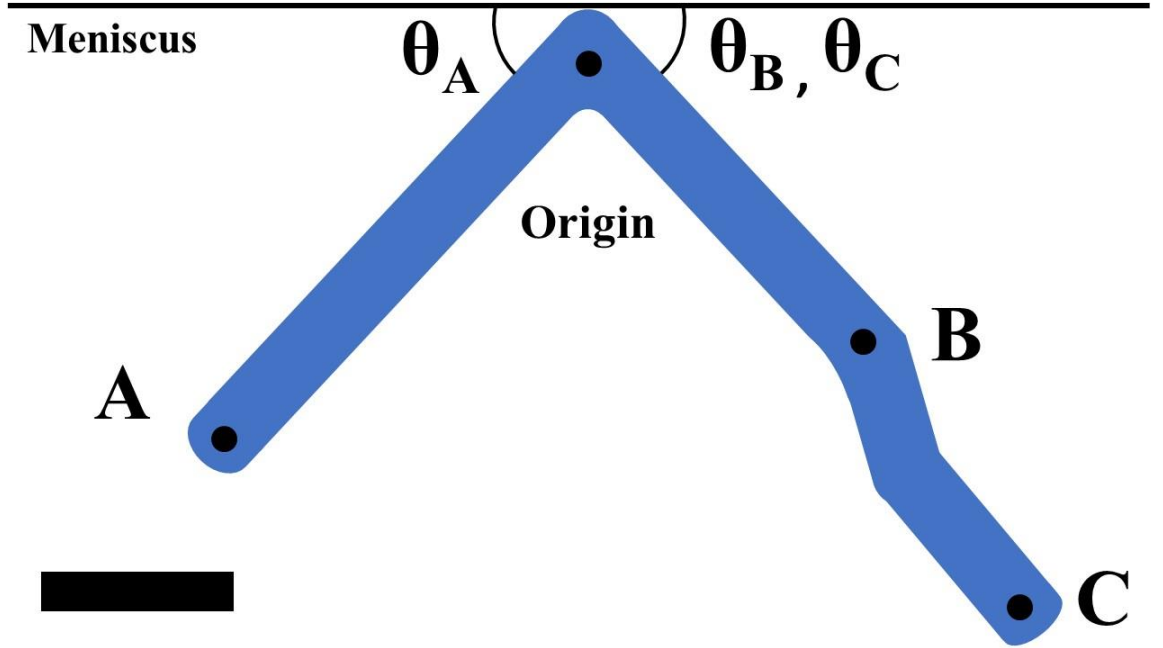


Figure 4.21. Diagram of CU bubble for video tracking (scale bar = 100 μm).

The buoyancy force creates a torque τ on the bubble

$$\vec{\tau} = \vec{r} \times \vec{F} \quad (68)$$

where r is the radius and F is the buoyancy force. The expression for the mechanical work of the bubble at r through the unbending is

$$W = \int_{\theta_1}^{\theta_2} \tau d\theta \quad (69)$$

where θ is the angle between the meniscus and bubble. Therefore

$$W = \int_{\theta_1}^{\theta_2} (r \times F) d\theta \quad (70)$$

$$W = \int_{\theta_1}^{\theta_2} \|r\| \|F\| \sin \phi d\theta \quad (71)$$

where ϕ is the angle between r and F . Since ϕ and θ are complementary (Figure 4.22) the variables can be switched by $\sin \phi = \cos \theta$.

$$W = \int_{\theta_1}^{\theta_2} \|r\| \|F\| \cos \theta d\theta \quad (72)$$

$$W = rF(\sin \theta_2 - \sin \theta_1) \quad (73)$$

since $\sin \phi = \cos \theta$.

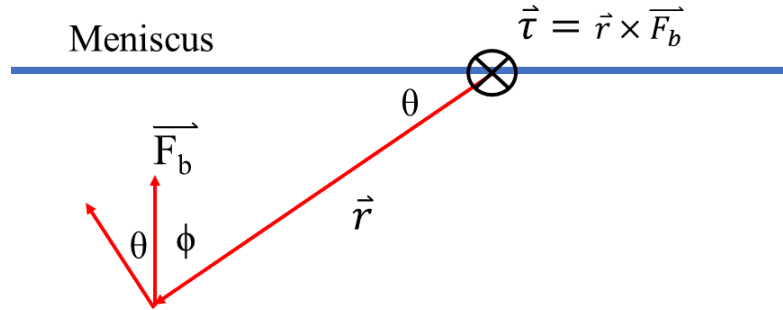


Figure 4.22. Vector diagram of bubble schematic showing ϕ and θ are complementary angles.

Using the buoyancy force previously mentioned $F_b = \rho g V_{displaced}$ and using image analysis to estimate the volume, the total work done by both arms of the bubbles is 14 pJ.

This is roughly 100 times the work done by a bacterial flagellar motor (BFM) that propels micron-sized filaments.¹⁶⁵

4.7 Conclusions

A reproducible agitation method for creating CU bubbles was created. This apparatus included a horizontal microscope for image analysis of the CU bubble ascension after agitation. The apparatus did not create uniform bubble sizes, but image analysis does show a correlation between agitation frequency and bubble size as maximum bubble size increases with frequency. The number density of bubbles with respect to size is mostly uniform before the maximum bubble size, which is governed by frequency. The bubble mechanics were examined using optical microscopy and showed kinked bubbles interacting with the meniscus. The estimated work done by the bubble at the kink is 14 pJ.

CHAPTER 5. CONCLUSIONS AND FUTURE WORK

5.1 Conclusions

This dissertation examined the cerato-ulmin hydrophobin-coated air bubbles resulting from agitating an aqueous solution even at low concentrations. CU is a small (7-9 kDa) fungal protein classified as a class II hydrophobin. Unlike many proteins that fold into a structure with the hydrophobic residues located internally, the eight cysteine residues in hydrophobins create four disulfide bonds. These bonds create a stiff internal structure resulting in hydrophobic residues on the surface establishing a natural, amphipathic, Janus-like particle. In solution, hydrophobins aggregate into larger structures that are more energetically favorable. These structures may be rodlets, surface films, or bubbles. In the case of CU, the structures below the surface are bubbles. The bubble film is a CU film of assembled proteins with a strength that could be regarded more as a solid than a film.

When an aqueous solution of CU is gently agitated, it creates a spectrum of bubbles ranging from 10^{-7} – 10^{-3} m. The existence of larger bubbles was previously known through optical microscopy, but the submicron bubbles were only suspected. The existence of submicron bubbles was explored in a thorough manner. Pressure experiment, both static and dynamic, show the structures to behave consistent with bubble response to pressure changes and inconsistent with other possible structures such as a solid or aggregate. Agitating a CU solution at different pressures created larger or smaller bubbles when a negative or positive pressure is applied. When the CU solution underwent a pressure cycle, the bubbles also changed in size, demonstrating their response behavior. As these results

are incongruous with solid structures or aggregates, the conclusion is that the CU forms submicron bubbles as well as microbubbles.

The thickness of CU bubbles across the size spectrum was measured. Optical microscopy calculations provided a rough estimate of film thickness that aided in SAXS modelling. Experiments completed at ORNL provided a possible structure of the protein using the ATSAS suite of programs. Finally, use of SAXS and AFM permitted construction of a model of the cylindrical submicron bubbles (Figure 3.26). The SAXS pattern was fit with a two-population custom model that features free CU proteins in solution and cylindrical bubbles with a thickness of 13.6 ± 3.2 nm and outside diameter of 69 ± 3.2 nm. For the larger bubbles, AFM measured the thickness of the film at 14 ± 1 nm. Using the protein size derived from the SAXS scattering of the free proteins in solution from the Guinier contribution, the bubble film is five proteins thick.

The reproducibility and standardization of bubble formation was also addressed. A sloshing wave tank apparatus with a horizontal microscope was designed and constructed to agitate a CU solution and observe bubble ascension. The apparatus did not create uniform bubble sizes, but a correlation between agitation frequency and bubble size was discovered, indicating maximum bubble size increases with frequency. The number density of bubbles with respect to size is mostly uniform before the maximum bubble size, which is governed by frequency. Bubble mechanics were also examined using optical microscopy, which showed kinked bubbles interacting with the meniscus. The estimated work done by the bubble at the kink is 14 pJ.

5.2 Future Work

5.2.1 *Effect of Time on CU Bubble Size*

Section 2.3 briefly describes the evolution of R_h in CU bubbles after agitation as the larger bubbles rise out of the solution. Results show the larger bubbles leaving the solution after 1 hour with the submicron bubbles remaining (Figure 2.5). These small bubbles are stable up to one month and do not rise to the surface as the buoyancy force of the bubbles is counteracted by the Brownian motion (Figure 2.3).⁸⁹ While the results are accurate and used to determine equilibration times after agitation for the pressure experiments, there are additional possible experiments such as agitating CU samples with different volumes of solution and measuring R_h with respect to time.

The CU samples for DLS experiments in this work were measured in glass test tube vials with a mL of solution to create a meniscus ~25 mm above the bottom. The laser path traveled through the sample ~12 mm from the bottom of vial. As covered in Section 4.3, the flow field varies with depth, so it is best practice to measure at the same depth even if hand agitation is not reproducible. For a CU solution with an $h = 75$ mm meniscus height from the cell bottom, gentle agitation would create small or even negligible motion for fluid near the bottom. If the CU bubbles are created through surface waves as hypothesized, the gentle agitation may not create any bubbles in the laser path at $h = 13$ mm. As different volumes of CU solutions are agitated the R_h versus time graph would change if the laser path is kept at constant height.

5.2.2 *Submicron Bubble Size Gradient with Depth*

For surface waves the fluid flow field is circular or elliptical orbits with decreasing size at greater depths. If the submicron CU bubbles are created through the surface waves, it is possible that bubble size decreases with depth. While the larger bubbles will rise out of the solution after one hour, the submicron bubbles do not rise because of the Brownian motion thus any size gradient would be static. If the DLS apparatus is modified to measure at different sample heights, the presence of a size gradient could be detected if it exists.

5.2.3 *Wave Tank Apparatus*

The construction of the wave tank apparatus creates multiple possibilities for experiments with CU as well as in other fields. The agitation system was built with the capability to change five variables: pressure, amplitude, frequency, magnification, sample cell. The final wave tanks have a connection for pressure variation with the tank still mounted on the apparatus to allow for imaging during pressure changes. Amplitude variability was accomplished through a variable yoke pin on the engine with 13 different amplitudes between 1.3–31.8 mm. Agitation frequency is controlled by the power output to the DC motor changing the speed of rotation. Magnification and sample cell changes are possible through adapters used in the design. This leads to a great number of combinations for starting conditions; discrete pressures with steps of 50 mbar between $P = 500$ –1300 mbar and ten different frequencies leads to 6240 possible starting conditions.

The horizontal microscope on the apparatus has additional potential for experiments with separate particles. Fluorescence photo-bleaching recovery (FPR) is an experimental technique for determining the diffusion of particles, proteins, and cell

membranes. Requiring samples that contain fluorophores, a light source illuminates a pattern on the sample to cause different area of photobleaching. Over time, the pattern fades as the particles diffuse across the entire sample due to the Brownian motion. Tracking the intensity changes then allows for calculating the diffusion constant for the sample.

Setup for this experiment is generally performed with a vertical microscope and laser beam path and a thin sample layer. While this generally works for many samples, larger samples experience sedimentation that interferes with the diffusion measurement. Increasing the sample height slows the sedimentation but transforms the diffusion from a 2D to a 3D calculation. By switching to a horizontal microscope, these issues are avoided and use of larger samples is possible. This is particularly interesting for measuring the jamming transition of polypeptide composite particles.

5.2.4 Bubble Reptation through Optical Tweezing

Optical tweezers are a scientific tool used to trap objects ranging from length scales between 10^{-10} to 10^{-5} m. Arthur Ashkin discovered the technique in 1970 by observing transparent micro latex spheres being drawn into the beam focus, an observation that led to the Nobel Prize in Physics in 2018.¹⁶⁶ The optical trap can be explained through a ray optics diagram or the electric forces arising from dipole interactions. For the ray optics explanation, Figure 5.1 shows a simple ray diagram of a transparent particle in a Gaussian beam with rays (a) and (b) traveling through the particle. Ray (a) refracts through the particle away from the beam center while ray (b) refracts towards the beam center. Due to Newton's third law the light refraction causes forces F_a and F_b upon the particle from the change of momentum in the light. Because of the beam intensity profile, the forces are

unequal and the particle experiences a gradient force towards the maximum intensity at the focal point of the laser.

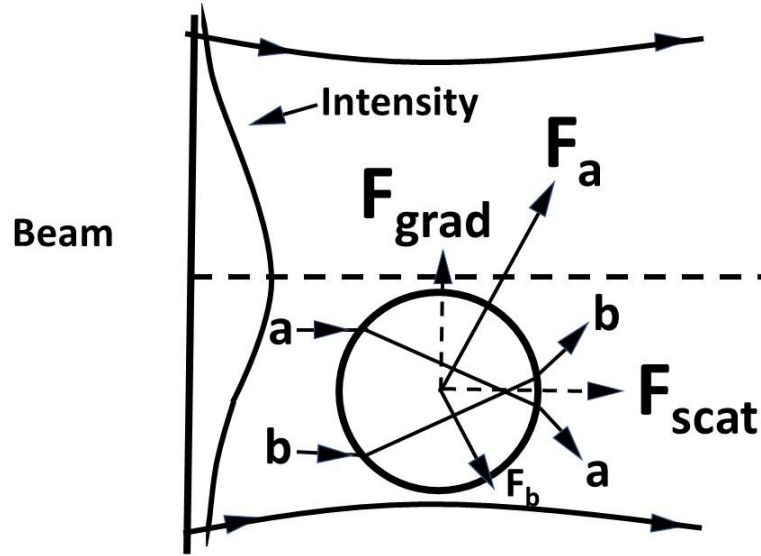


Figure 5.1. Ray diagram for a particle in an optical trap. Adapted from reference 167.

Another way to interpret the effect is through the consideration of induced electric dipole interactions. All light consists of transverse oscillating electric and magnetic fields according to the Maxwell classical theory. When light interacts with an atom it induces a dipole from the interactions with the positively charged nucleus and negatively charged electron cloud. For any charged particle in an electric field there is a Lorentzian force

$$F_{dipole} = (\vec{p} \cdot \nabla) \vec{E} + \frac{d\vec{p}}{dt} \times \vec{B} \quad (74)$$

where \vec{p} is the polarization, \vec{E} is the electric field, and \vec{B} is the magnetic field. Using equations for the definition of polarization α , a vector calculus identity and one of the Maxwell equations

$$\vec{p} = \alpha \vec{E} \quad (75)$$

$$(E \cdot \nabla)E = \nabla \left(\frac{1}{2} E^2 \right) - E \times (\nabla \times E) \quad (76)$$

$$\nabla \times E = -\frac{\delta B}{\delta t} \quad (77)$$

the force can be rewritten as

$$F_{dipole} = (\vec{p} \cdot \nabla) \vec{E} + \frac{d\vec{p}}{dt} \times \vec{B} \quad (78)$$

The second term is the time derivative of the Poynting vector which is a measurement of the energy flux. For a laser with constant intensity, the time derivative of the Poynting vector is zero and the force on the atom is

$$F_{dipole} = \frac{1}{2} \alpha E^2 \quad (79)$$

By inserting the induced dipole of a spherical dielectric particle the polarization α

$$\alpha = \frac{4\pi n_0^2 a^3}{c} \left(\frac{m^2 - 1}{m^2 + 1} \right) \quad (80)$$

and the relationship between the electric field \vec{E} and intensity of light

$$|E|^2 = \nabla I(r) \quad (81)$$

the force from the optical tweezers is

$$F = \frac{2\pi n_0 a^3}{c} \left(\frac{m^2 - 1}{m^2 + 2} \right) \nabla I(r) \quad (82)$$

where n_0 is the index of the medium, a is the particle radius, m is the ratio between the index of refraction for the particle n_a and medium n_b , and $I(r)$ is the intensity of the light. This results in a gradient force that pulls particles to the maximum light intensity when $n_a > n_b$ and pushes particles away from the maximum light intensity when $n_a < n_b$. In many cases the particles have a greater index of refraction and will be pulled toward the focal point of the laser beam. In the case of CU bubbles, where $n_{air} < n_{water}$, the bubbles are pushed away from the focal point of the laser.

Early optical tweezer setups used a single laser beam and moved the sample stage or changed the beam path to move the focal point of the beam with mirrors. Because this will not work for the CU sample, a multi-trap system is needed to confine the bubbles. One of the methods to create multiple traps is to use holographic optical tweezers. The chosen setup will use a spatial light modulator (SLM) to create multiple beams through constructive and destructive interference. The $\lambda = 1064$ nm laser travels through a beam expander before interacting with the SLM. The SLM contains a liquid crystal that alters the phase of the light from $0-2\pi$ at each pixel before reflection by a mirror. After exiting the SLM, the beam is focused, and the phase-shifted light constructively and destructively

interferes to form the desired pattern on the image plane. This setup has successfully trapped seven colloidal silica bullets in a 3x3 holographic optical trap (Figure 5.2).

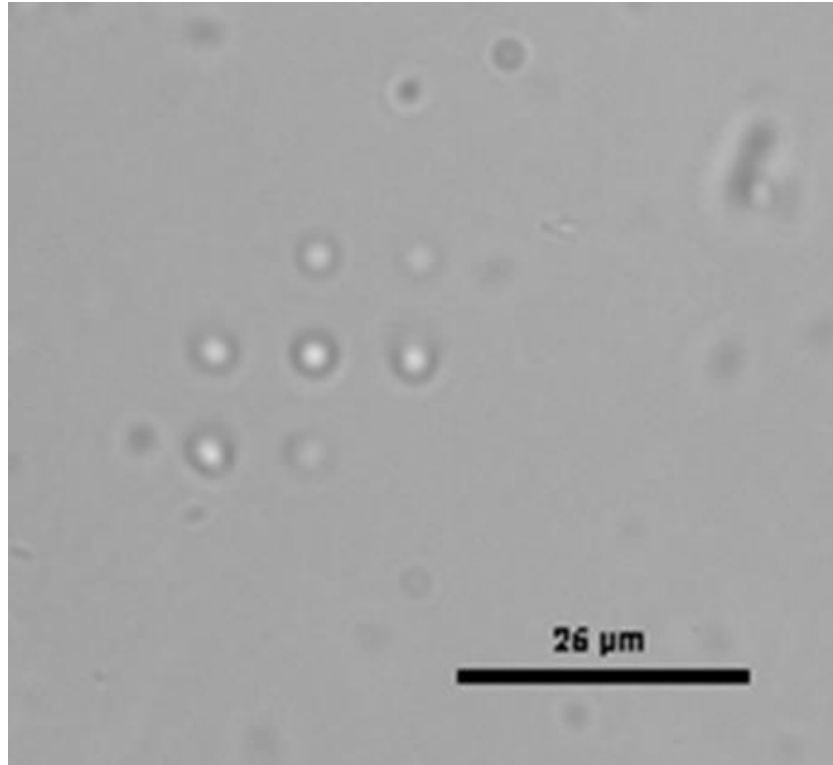


Figure 5.2. Seven silica bullets in a 3x3 optical tweezer trap using a 1064 nm laser.

The proposed experiment is measuring the reptation of the bubble through the optical traps. The concept of reptation was introduced by de Gennes in 1971 to explain the motion of polymers in an entangled state.¹⁶⁸ In a non-dilute solution, polymers propagate in the direction of the chain as other polymers create physical barriers that prevent lateral motion. In the case of the CU bubble the optical traps provide the physical barriers limiting motion to only reptation. To combat the natural rise of the bubble additional optical traps will keep the bubble motion confined to two dimensions. Combining the equations for the mean square displacement of one-dimension diffusion and the Einstein relation

$$\overline{x^2} = 2Dt \quad (83)$$

$$D = \mu kT \quad (84)$$

we arrive at

$$t = \frac{\overline{x^2}}{2\mu kT} \quad (85)$$

where x is displacement, D is the diffusion, t is time, μ is the mobility, k is the Boltzmann constant, and T is the temperature.

The significance of this experiment is an improvement over the method by which reptation experiments are currently done. Currently reptation measurements occur in concentrated solutions where adjacent polymer chains act as physical barriers. Hydrodynamic interactions between the probe chain and constraining chain confound the analysis of the results in terms of the simple model proposed by de Gennes. By using optical traps, physical barriers are replaced by optical ones: there are no hydrodynamic interactions between the probe chain and interacting chains.

5.2.5 *Response Kinetics of Bubbles*

Section 2.5 shows the CU submicron bubble size responds to changing pressures as it contracts and expands during a pressure cycle. In the experiments, the CU bubbles were measured one hour after the pressure change to allow for equilibration (Figure 2.15); the kinematics during the pressure changes were ignored. The kinetics of the CU bubble film during expansion and contraction was examined¹⁰⁶ but there is no current work on the

kinetics of bubbles in solution. One method to examine this would be tracking the change in the DLS auto-correlation function as pressure changes.

REFERENCES

1. Kisko, K.; Szilvay, G. R.; Vuorimaa, E.; Lemmetyinen, H.; Linder, M. B.; Torkkeli, M.; Serimaa, R., Self-assembled films of hydrophobin protein HFBIII from *Trichoderma reesei*. *Journal of Applied Crystallography* **2007**, *40*, S355-S360.
2. de Vocht, M. L.; Reviakine, I.; Ulrich, W. P.; Bergsma-Schutter, W.; Wosten, H. A.; Vogel, H.; Brisson, A.; Wessels, J. G.; Robillard, G. T., Self-assembly of the hydrophobin SC3 proceeds via two structural intermediates. *Protein Sci* **2002**, *11* (5), 1199-205.
3. Wosten, H. A. B.; Devries, O. M. H.; Wessels, J. G. H., Interfacial Self-Assembly of a Fungal Hydrophobin into a Hydrophobic Rodlet Layer. *Plant Cell* **1993**, *5* (11), 1567-1574.
4. Wessels, J. G. H.; Devries, O. M. H.; Asgeirsdottir, S. A.; Schuren, F. H. J., Hydrophobin Genes Involved in Formation of Aerial Hyphae and Fruit Bodies in *Schizophyllum*. *Plant Cell* **1991**, *3* (8), 793-799.
5. Askolin, S.; Linder, M.; Scholtmeijer, K.; Tenkanen, M.; Penttilä, M.; de Vocht, M. L.; Wosten, H. A. B., Interaction and comparison of a class I hydrophobin from *Schizophyllum commune* and class II hydrophobins from *Trichoderma reesei*. *Biomacromolecules* **2006**, *7* (4), 1295-1301.
6. Lumsdon, S. O.; Green, J.; Stieglitz, B., Adsorption of hydrophobin proteins at hydrophobic and hydrophilic interfaces. *Colloid Surface B* **2005**, *44* (4), 172-178.
7. vanderVegt, W.; vanderMei, H. C.; Wosten, H. A. B.; Wessels, J. G. H.; Busscher, H. J., A comparison of the surface activity of the fungal hydrophobin SC3p with those of other proteins. *Biophys Chem* **1996**, *57* (2-3), 253-260.
8. Wosten, H. A. B.; Devries, O. M. H.; Vandermei, H. C.; Busscher, H. J.; Wessels, J. G. H., Atomic Composition of the Hydrophobic and Hydrophilic Membrane Sides of Self-Assembled Sc3p Hydrophobin. *J Bacteriol* **1994**, *176* (22), 7085-7086.
9. de Vocht, M. L.; Scholtmeijer, K.; van der Vegte, E. W.; de Vries, O. M. H.; Sonveaux, N.; Wosten, H. A. B.; Ruyschaert, J. M.; Hadziioannou, G.; Wessels, J. G. H.; Robillard, G. T., Structural characterization of the hydrophobin SC3, as a monomer and after self-assembly at hydrophobic/hydrophilic interfaces. *Biophys J* **1998**, *74* (4), 2059-2068.
10. Hakanpää, J.; Szilvay, G. R.; Kaljunen, H.; Maksimainen, M.; Linder, M.; Rouvinen, J., Two crystal structures of *Trichoderma reesei* hydrophobin HFBI - The

structure of a protein amphiphile with and without detergent interaction. *Protein Science* **2006**, *15* (9), 2129-2140.

11. Devries, O. M. H.; Fekkes, M. P.; Wosten, H. A. B.; Wessels, J. G. H., Insoluble Hydrophobin Complexes in the Walls of Schizophyllum-Commune and Other Filamentous Fungi. *Arch Microbiol* **1993**, *159* (4), 330-335.

12. Hakanpaa, J.; Paananen, A.; Askolin, S.; Nakari-Setälä, T.; Parkkinen, T.; Penttilä, M.; Linder, M. B.; Rouvinen, J., Atomic resolution structure of the HFBII hydrophobin, a self-assembling amphiphile. *J Biol Chem* **2004**, *279* (1), 534-539.

13. de Vocht, M. L.; Reviakine, I.; Wosten, H. A. B.; Brisson, A.; Wessels, J. G. H.; Robillard, G. T., Structural and functional role of the disulfide bridges in the hydrophobin SC3. *J Biol Chem* **2000**, *275* (37), 28428-28432.

14. Kwan, A. H. Y.; Winefield, R. D.; Sunde, M.; Matthews, J. M.; Haverkamp, R. G.; Templeton, M. D.; Mackay, J. P., Structural basis for rodlet assembly in fungal hydrophobins. *P Natl Acad Sci USA* **2006**, *103* (10), 3621-3626.

15. Wosten, H. A. B.; Willey, J. M., Surface-active proteins enable microbial aerial hyphae to grow into the air. *Microbiol-Uk* **2000**, *146*, 767-773.

16. Wosten, H. A. B.; Schuren, F. H. J.; Wessels, J. G. H., Interfacial Self-Assembly of a Hydrophobin into an Amphipathic Protein Membrane Mediates Fungal Attachment to Hydrophobic Surfaces. *Embo J* **1994**, *13* (24), 5848-5854.

17. Lugones, L. G.; Wosten, H. A. B.; Birkenkamp, K. U.; Sjollem, K. A.; Zagers, J.; Wessels, J. G. H., Hydrophobins line air channels in fruiting bodies of Schizophyllum commune and Agaricus bisporus. *Mycol Res* **1999**, *103*, 635-640.

18. Tchuenbou-Magaia, F. L.; Norton, I. T.; Cox, P. W., Hydrophobins stabilised air-filled emulsions for the food industry. *Food Hydrocolloid* **2009**, *23* (7), 1877-1885.

19. Dickinson, E., Colloids in Food: Ingredients, Structure, and Stability. *Annual Review of Food Science and Technology*, Vol 6 **2015**, *6*, 211-233.

20. Green, A. J.; Littlejohn, K. A.; Hooley, P.; Cox, P. W., Formation and stability of food foams and aerated emulsions: Hydrophobins as novel functional ingredients. *Curr Opin Colloid In* **2013**, *18* (4), 292-301.

21. Scholtmeijer, K.; Janssen, M. I.; Gerssen, B.; de Vocht, M. L.; van Leeuwen, B. M.; van Kooten, T. G.; Wosten, H. A. B.; Wessels, J. G. H., Surface modifications created by using engineered hydrophobins. *Appl Environ Microb* **2002**, *68* (3), 1367-1373.

22. Akanbi, M. H. J.; Post, E.; Meter-Arkema, A.; Rink, R.; Robillard, G. T.; Wang, X. Q.; Wosten, H. A. B.; Scholtmeijer, K., Use of hydrophobins in formulation of water insoluble drugs for oral administration. *Colloid Surface B* **2010**, *75* (2), 526-531.

23. Rosu, C.; Kleinhenz, N.; Choi, D.; Tassone, C. J.; Zhang, X. J.; Park, J. O.; Srinivasarao, M.; Russo, P. S.; Reichmanis, E., Protein-Assisted Assembly of pi-Conjugated Polymers. *Chem Mater* **2016**, 28 (2), 573-582.
24. Wosten, H. A. B.; Scholtmeijer, K., Applications of hydrophobins: current state and perspectives. *Appl Microbiol Biot* **2015**, 99 (4), 1587-1597.
25. Wosten, H. A. B., Hydrophobins: Multipurpose proteins. *Annu Rev Microbiol* **2001**, 55, 625-646.
26. Wosten, H. A. B.; de Vocht, M. L., Hydrophobins, the fungal coat unravelled. *Bba-Rev Biomembranes* **2000**, 1469 (2), 79-86.
27. Wessels, J. G. H., Hydrophobins: Proteins that change the nature of the fungal surface. *Adv Microb Physiol* **1997**, 38, 1-45.
28. Drenth, J.; Low, B. W.; Richardson, J. S.; Wright, C. S., The Toxin-Agglutinin Fold - a New Group of Small Protein Structures Organized around a 4-Disulfide Core. *J Biol Chem* **1980**, 255 (7), 2652-2655.
29. Sterk, P.; Booiij, H.; Schellekens, G. A.; Vankammen, A.; Devries, S. C., Cell-Specific Expression of the Carrot Ep2 Lipid Transfer Protein Gene. *Plant Cell* **1991**, 3 (9), 907-921.
30. Carpenter, E. P.; Beis, K.; Cameron, A. D.; Iwata, S., Overcoming the challenges of membrane protein crystallography. *Curr Opin Struc Biol* **2008**, 18 (5), 581-586.
31. Hakanpaa, J.; Parkkinen, T. A. A.; Hakulinen, N.; Linder, M.; Rouvinen, J., Crystallization and preliminary X-ray characterization of *Trichoderma reesei* hydrophobin HFBII. *Acta Crystallogr D* **2004**, 60, 163-165.
32. Hakanpaa, J.; Linder, M.; Popov, A.; Schmidt, A.; Rouvinen, J., Hydrophobin HFBII in detail: ultrahigh-resolution structure at 0.75 angstrom. *Acta Crystallogr D* **2006**, 62, 356-367.
33. Schmidt, B., Proteins: Structure and Function. By David Whitford. *ChemBioChem* **2006**, 7 (4), 702-703.
34. Kwan, A. H.; Macindoe, I.; Vukasin, P. V.; Morris, V. K.; Kass, I.; Gupte, R.; Mark, A. E.; Templeton, M. D.; Mackay, J. P.; Sunde, M., The Cys3-Cys4 loop of the hydrophobin EAS is not required for rodlet formation and surface activity. *J Mol Biol* **2008**, 382 (3), 708-720.
35. Morris, V. K.; Kwan, A. H.; Sunde, M., Analysis of the Structure and Conformational States of DewA Gives Insight into the Assembly of the Fungal Hydrophobins. *J Mol Biol* **2013**, 425 (2), 244-256.

36. Morris, V. K.; Kwan, A. H.; Mackay, J. P.; Sunde, M., Backbone and sidechain H-1, C-13 and N-15 chemical shift assignments of the hydrophobin DewA from *Aspergillus nidulans*. *Biomol Nmr Assign* **2012**, 6 (1), 83-86.
37. Rey, A. A.; Hocher, A.; Kwan, A. H.; Sunde, M., Backbone and sidechain H-1, C-13 and N-15 chemical shift assignments of the hydrophobin MPG1 from the rice blast fungus *Magnaporthe oryzae*. *Biomol Nmr Assign* **2013**, 7 (1), 109-112.
38. Pille, A.; Kwan, A. H.; Cheung, I.; Hampsey, M.; Aimaniananda, V.; Delepierre, M.; Latge, J. P.; Sunde, M.; Guijarro, J. I., H-1, C-13 and N-15 resonance assignments of the RodA hydrophobin from the opportunistic pathogen *Aspergillus fumigatus*. *Biomol Nmr Assign* **2015**, 9 (1), 113-118.
39. Ren, Q.; Kwan, A. H.; Sunde, M., Solution structure and interface-driven self-assembly of NC2, a new member of the Class II hydrophobin proteins. *Proteins* **2014**, 82 (6), 990-1003.
40. De Vocht, M. L.; Reviakine, I.; Ulrich, W. P.; Bergsma-Schutter, W.; Wosten, H. A. B.; Vogel, H.; Brisson, A.; Wessels, J. G. H.; Robillard, G. T., Self-assembly of the hydrophobin SC3 proceeds via two structural intermediates. *Protein Sci* **2002**, 11 (5), 1199-1205.
41. Linder, M. B.; Szilvay, G. R.; Nakari-Setälä, T.; Penttilä, M. E., Hydrophobins: the protein-amphiphiles of filamentous fungi. *Fems Microbiol Rev* **2005**, 29 (5), 877-896.
42. Carpenter, C. E.; Mueller, R. J.; Kazmierczak, P.; Zhang, L.; Villalon, D. K.; Vanalfen, N. K., Effect of a Virus on Accumulation of a Tissue-Specific Cell-Surface Protein of the Fungus *Cryphonectria*-(*Endothia*)-*Parasitica*. *Mol Plant Microbe In* **1992**, 5 (1), 55-61.
43. Russo, P. S.; Blum, F. D.; Ipsen, J. D.; Abulhadj, Y. J.; Miller, W. G., The Solubility and Surface-Activity of the *Ceratocystis-Ulmi* Toxin Cerato-Ulmin. *Physiol Plant Pathol* **1981**, 19 (1), 113-126.
44. Janssen, M. I.; van Leeuwen, M. B. M.; Scholtmeijer, K.; van Kooten, T. G.; Dijkhuizen, L.; Wosten, H. A. B., Coating with genetic engineered hydrophobin promotes growth of fibroblasts on a hydrophobic solid. *Biomaterials* **2002**, 23 (24), 4847-4854.
45. Janssen, M. I.; van Leeuwen, M. B. M.; van Kooten, T. G.; de Vries, J.; Dijkhuizen, L.; Wosten, H. A. B., Promotion of fibroblast activity by coating with hydrophobins in the beta-sheet end state. *Biomaterials* **2004**, 25 (14), 2731-2739.
46. Paslay, L. C.; Falgout, L.; Savin, D. A.; Heinhorst, S.; Cannon, G. C.; Morgan, S. E., Kinetics and control of self-assembly of ABH1 hydrophobin from the edible white button mushroom. *Biomacromolecules* **2013**, 14 (7), 2283-93.

47. Yang, W. R.; Ren, Q.; Wu, Y. N.; Morris, V. K.; Rey, A. A.; Braet, F.; Kwan, A. H.; Sunde, M., Surface functionalization of carbon nanomaterials by self-assembling hydrophobin proteins. *Biopolymers* **2013**, 99 (1), 84-94.
48. Wang, Z. F.; Wang, Y. Y.; Huang, Y. J.; Li, S.; Feng, S. R.; Xu, H. J.; Qiao, M. Q., Characterization and application of hydrophobin-dispersed multi-walled carbon nanotubes. *Carbon* **2010**, 48 (10), 2890-2898.
49. Weickert, U.; Wiesend, F.; Subkowski, T.; Eickhoff, A.; Reiss, G., Optimizing biliary stent patency by coating with hydrophobin alone or hydrophobin and antibiotics or heparin: an in vitro proof of principle study. *Adv Med Sci-Poland* **2011**, 56 (2), 138-144.
50. Weickert, U.; Weddeling, S.; Subkowski, T.; Eickhoff, A.; Reiss, G., Improving biliary stent patency by the use of stent coating - a prospective randomized porcine study. *Z Gastroenterol* **2016**, 54 (7), 629-633.
51. Hektor, H. J.; Scholtmeijer, K., Hydrophobins: proteins with potential. *Curr Opin Biotech* **2005**, 16 (4), 434-439.
52. Wosten, H. A. B.; Asgeirsdottir, S. A.; Krook, J. H.; Drenth, J. H. H.; Wessels, J. G. H., The Fungal Hydrophobin Sc3p Self-Assembles at the Surface of Aerial Hyphae as a Protein Membrane Constituting the Hydrophobic Rodlet Layer. *Eur J Cell Biol* **1994**, 63 (1), 122-129.
53. Reger, M.; Hoffmann, H., Hydrophobin coated boehmite nanoparticles stabilizing oil in water emulsions. *J Colloid Interf Sci* **2012**, 368, 378-386.
54. Tchuente-Magaia, F. L.; Norton, I. T.; Cox, P. W., Microbubbles with Protein Coats for Healthy Food Air Filled Emulsions. *Gums and Stabilisers for the Food Industry 15* **2010**, 113-125.
55. Cox, A. R.; Cagnol, F.; Russell, A. B.; Izzard, M. J., Surface properties of class II hydrophobins from *Trichoderma reesei* and influence on bubble stability. *Langmuir* **2007**, 23 (15), 7995-8002.
56. Blijdenstein, T. B. J.; de Groot, P. W. N.; Stoyanov, S. D., On the link between foam coarsening and surface rheology: why hydrophobins are so different. *Soft Matter* **2010**, 6 (8), 1799-1808.
57. Cox, A. R.; Aldred, D. L.; Russell, A. B., Exceptional stability of food foams using class II hydrophobin HFBII. *Food Hydrocolloid* **2009**, 23 (2), 366-376.
58. Garbe, L. A.; Schwarz, P.; Ehmer, A., Beer gushing. *Beer: A Quality Perspective: A Volume of the Handbook of Alcoholic Beverages Series* **2009**, 185-212.
59. Hippeli, S.; Elstner, E. F., Are hydrophobins and/or non-specific lipid transfer proteins responsible for gushing in beer? New hypotheses on the chemical nature of gushing inducing factors. *Z Naturforsch C* **2002**, 57 (1-2), 1-8.

60. Postulkova, M.; Riveros-Galan, D.; Cordova-Agiular, K.; Zitkova, K.; Verachtert, H.; Derdelinckx, G.; Dostalek, P.; Ruzicka, M. C.; Branyik, T., Technological possibilities to prevent and suppress primary gushing of beer. *Trends Food Sci Tech* **2016**, *49*, 64-73.
61. Lusk, L. T., Controlling Beer Foam and Gushing. *Brewing Materials and Processes: A Practical Approach to Beer Excellence* **2016**, 175-198.
62. Deckers, S. M.; Lorgouilloux, Y.; Gebruers, K.; Baggerman, G.; Verachtert, H.; Neven, H.; Michiels, C.; Derdelinckx, G.; Delcour, J. A.; Martens, J., Dynamic Light Scattering (DLS) as a Tool to Detect CO₂-Hydrophobin Structures and Study the Primary Gushing Potential of Beer. *J Am Soc Brew Chem* **2011**, *69* (3), 144-149.
63. Marinova, G.; Batchvarov, V., Investigation on the Gushing Potential of Malts and Beers. *Proceedings of the 2008 Joint Central European Congress, Vol 2* **2008**, 335-342.
64. Khalesi, M.; Deckers, S.; Riveros-Galan, D.; Gebruers, K.; Derdelinckx, G., Upgraded Model of Primary Gushing: From Nanobubble Formation Until Liquid Expulsion. *J Am Soc Brew Chem* **2015**, *73* (4), 343-346.
65. Valo, H.; Kovalainen, M.; Laaksonen, P.; Hakkinen, M.; Auriola, S.; Peltonen, L.; Linder, M.; Jarvinen, K.; Hirvonen, J.; Laaksonen, T., Immobilization of protein-coated drug nanoparticles in nanofibrillar cellulose matrices-Enhanced stability and release. *J Control Release* **2011**, *156* (3), 390-397.
66. Vejnovic, I.; Simmler, L.; Betz, G., Investigation of different formulations for drug delivery through the nail plate. *Int J Pharmaceut* **2010**, *386* (1-2), 185-194.
67. Vejnovic, I.; Huonder, C.; Betz, G., Permeation studies of novel terbinafine formulations containing hydrophobins through human nails in vitro. *Int J Pharmaceut* **2010**, *397* (1-2), 67-76.
68. Fang, G. H.; Tang, B.; Liu, Z. T.; Gou, J. X.; Zhang, Y.; Xu, H.; Tang, X., Novel hydrophobin-coated docetaxel nanoparticles for intravenous delivery: In vitro characteristics and in vivo performance. *Eur J Pharm Sci* **2014**, *60*, 1-9.
69. Taniguchi, S.; Sandiford, L.; Cooper, M.; Rosca, E. V.; Khanbeigi, R. A.; Fairclough, S. M.; Thanou, M.; Dailey, L. A.; Wohlleben, W.; von Vacano, B.; de Rosales, R. T. M.; Dobson, P. J.; Owen, D. M.; Green, M., Hydrophobin-Encapsulated Quantum Dots. *Acs Appl Mater Inter* **2016**, *8* (7), 4887-4893.
70. Bimbo, L. M.; Makila, E.; Raula, J.; Laaksonen, T.; Laaksonen, P.; Strommer, K.; Kauppinen, E. I.; Salonen, J.; Linder, M. B.; Hirvonen, J.; Santos, H. A., Functional hydrophobin-coating of thermally hydrocarbonized porous silicon microparticles. *Biomaterials* **2011**, *32* (34), 9089-9099.
71. Valo, H.; Arola, S.; Laaksonen, P.; Torkkeli, M.; Peltonen, L.; Linder, M. B.; Serimaa, R.; Kuga, S.; Hirvonen, J.; Laaksonen, T., Drug release from nanoparticles

embedded in four different nanofibrillar cellulose aerogels. *Eur J Pharm Sci* **2013**, *50* (1), 69-77.

72. Matea, C. T.; Mocan, T.; Tabaran, F.; Pop, T.; Mosteanu, O.; Puia, C.; Iancu, C.; Mocan, L., Quantum dots in imaging, drug delivery and sensor applications. *Int J Nanomed* **2017**, *12*, 5421-5431.

73. Brasier, C. M., Intercontinental spread and continuing evolution of the Dutch elm disease pathogens In *The Elms: Breeding, Conservation, and Disease Management* Dunn, C. P., Ed. Kluwer Academic Publishers: 2000; pp 61-72.

74. Brasier, C. M.; Buck, K. W., Rapid Evolutionary Changes in a Globally Invading Fungal Pathogen (Dutch Elm Disease). *Biological Invasions* **2001**, *3* (3), 223-233.

75. Temple, B.; Horgen, P. A., Biological roles for cerato-ulmin, a hydrophobin secreted by the elm pathogens, *Ophiostoma ulmi* and *O-novo-ulmi*. *Mycologia* **2000**, *92* (1), 1-9.

76. Takai, S., Pathogenicity and Cerato-Ulmin Production in *Ceratocystis-Ulmi*. *Nature* **1974**, *252* (5479), 124-126.

77. Yaguchi, M.; Pusztai-carey, M.; Roy, C.; Surewicz, W. K.; Carey, P. R.; Stevenson, K. J.; Richards, W. C.; Takai, S., Amino-Acid-Sequence and Spectroscopic Studies of Dutch Elm Disease Toxin, Cerato-Ulmin. *Dutch Elm Disease Research* **1993**, 152-170.

78. Wosten, H. A. B.; van Wetter, M. A.; Lugones, L. G.; van der Mei, H. C.; Busscher, H. J.; Wessels, J. G. H., How a fungus escapes the water to grow into the air. *Curr Biol* **1999**, *9* (2), 85-88.

79. Hakala, T. J.; Metsajoki, J.; Granqvist, N.; Milani, R.; Szilvay, G. R.; Elomaa, O.; Deng, M. M.; Zhang, J. J.; Li, F., Adsorption and lubricating properties of HFBII hydrophobins and diblock copolymer poly(methyl methacrylate-b-sodium acrylate) additives in water-lubricated copper vs. a-C:H contacts. *Tribol Int* **2015**, *90*, 60-66.

80. Zhang, X. L.; Penfold, J.; Thomas, R. K.; Tucker, I. M.; Petkov, J. T.; Bent, J.; Cox, A.; Campbell, R. A., Adsorption Behavior of Hydrophobin and Hydrophobin/Surfactant Mixtures at the Air-Water Interface. *Langmuir* **2011**, *27* (18), 11316-11323.

81. Liu, Y. Z.; Wu, M.; Feng, X. Z.; Shao, X. G.; Cai, W. S., Adsorption Behavior of Hydrophobin Proteins on Polydimethylsiloxane Substrates. *J Phys Chem B* **2012**, *116* (40), 12227-12234.

82. Torkkeli, M.; Serimaa, R.; Ikkala, O.; Linder, M., Aggregation and self-assembly of hydrophobins from *Trichoderma reesei*: Low-resolution structural models. *Biophys J* **2002**, *83* (4), 2240-2247.

83. Kallio, J. M.; Rouvinen, J., Amphiphilic nanotubes in the crystal structure of a biosurfactant protein hydrophobin HFBII. *Chem Commun* **2011**, *47* (35), 9843-9845.

84. Asakawa, H.; Tahara, S.; Nakamichi, M.; Takehara, K.; Ikeno, S.; Linder, M. B.; Haruyama, T., The Amphiphilic Protein HFBII as a Genetically Taggable Molecular Carrier for the Formation of a Self-Organized Functional Protein Layer on a Solid Surface. *Langmuir* **2009**, *25* (16), 8841-8844.
85. Raffaini, G.; Milani, R.; Ganazzoli, F.; Resnati, G.; Metrangolo, P., Atomistic simulation of hydrophobin HFBII conformation in aqueous and fluoruous media and at the water/vacuum interface. *J Mol Graph Model* **2016**, *63*, 8-14.
86. Winterburn, J. B.; Russell, A. B.; Martin, P. J., Characterisation of HFBII biosurfactant production and foam fractionation with and without antifoaming agents. *Appl Microbiol Biot* **2011**, *90* (3), 911-920.
87. Gruner, M. S.; Paananen, A.; Szilvay, G. R.; Linder, M. B., The dynamics of multimer formation of the amphiphilic hydrophobin protein HFBII. *Colloid Surface B* **2017**, *155*, 111-117.
88. Russo, P. S.; Blum, F. D.; Ipsen, J. D.; Abulhadj, Y. J.; Miller, W. G., The Surface-Activity of the Phytotoxin Cerato-Ulmin. *Can J Bot* **1982**, *60* (8), 1414-1422.
89. Zhang, X. Cerato-ulmin Hydrophobin-Coated Air Bubbles and Oil Droplets: Stability, Shapes, and Interfacial Behavior. Georgia Institute of Technology, Atlanta, GA, 2018.
90. Gauss, C. F., *Principia generalia theoriae figurae fluidorum in statu aequilibrii*. Dieterichs: Gottingae, 1830; p ii, 53 p.
91. Karamanou, M.; Papaioannou, T. G.; Stefanadis, C.; Androutsos, G., Genesis of Ultrasonic Microbubbles: A Quick Historical Overview. *Curr Pharm Design* **2012**, *18* (15), 2115-2117.
92. Farook, U.; Edirisinghe, M. J.; Stride, E.; Colombo, P., Novel co-axial electrohydrodynamic in-situ preparation of liquid-filled polymer-shell microspheres for biomedical applications. *J Microencapsul* **2008**, *25* (4), 241-247.
93. Cavalieri, F.; El Hamassi, A.; Chiessi, E.; Paradossi, G., Stable polymeric microballoons as multifunctional device for biomedical uses: Synthesis and characterization. *Langmuir* **2005**, *21* (19), 8758-8764.
94. Ettelaie, R.; Murray, B. S., Evolution of bubble size distribution in particle stabilised bubble dispersions: Competition between particle adsorption and dissolution kinetics. *Colloid Surface A* **2015**, *475*, 27-36.
95. Dimitrova, L. M.; Petkov, P. V.; Kralchevsky, P. A.; Stoyanov, S. D.; Pelan, E. G., Production and characterization of stable foams with fine bubbles from solutions of hydrophobin HFBII and its mixtures with other proteins. *Colloid Surface A* **2017**, *521*, 92-104.

96. Tchuenbou-Magaia, F. L.; Al-Rifai, N.; Ishak, N. E. M.; Norton, I. T.; Cox, P. W., Suspensions of air cells with cysteine-rich protein coats: Air-filled emulsions. *J Cell Plast* **2011**, 47 (3), 217-232.
97. Gorman, A.; Zhang, X.; Risteen, B.; Tassone, C. J.; Russo, P. S., Characterization of Submicron Bubbles Formed by the Hydrophobin Cerato-ulmin. *The Journal of Physical Chemistry B* **2019**.
98. Koppel, D. E., Analysis of Macromolecular Polydispersity in Intensity Correlation Spectroscopy - Method of Cumulants. *J Chem Phys* **1972**, 57 (11), 4814-&.
99. Provencher, S. W., A Constrained Regularization Method for Inverting Data Represented by Linear Algebraic or Integral-Equations. *Comput Phys Commun* **1982**, 27 (3), 213-227.
100. Liu, L.; Yan, H.; Zhao, G.; Zhuang, J., Experimental studies on the terminal velocity of air bubbles in water and glycerol aqueous solution. *Experimental Thermal and Fluid Science* **2016**, 78, 254-265.
101. Levich, V. G., *Physicochemical hydrodynamics*. Prentice-Hall: Englewood Cliffs, N.J., 1962.
102. Li, T.; Kheifets, S.; Medellin, D.; Raizen, M. G., Measurement of the Instantaneous Velocity of a Brownian Particle. *Science* **2010**, 328 (5986), 1673.
103. Zwanzig, R.; Bixon, M., Compressibility effects in the hydrodynamic theory of Brownian motion. *J Fluid Mech* **2006**, 69 (1), 21-25.
104. Chaplin, M., Nanobubbles (ultrafine bubbles). In *Water Structure and Science* London 2007.
105. Berne, B. J.; Pecora, R., *Dynamic light scattering : with applications to chemistry, biology, and physics*. Wiley: New York, 1976; p vii, 376 p.
106. Zhang, X. J.; Kirby, S. M.; Chen, Y. W.; Anna, S. L.; Walker, L. M.; Hung, F. R.; Russo, P. S., Formation and elasticity of membranes of the class II hydrophobin Cerato-ulmin at oil-water interfaces. *Colloid Surface B* **2018**, 164, 98-106.
107. Franke, D.; Svergun, D. I., DAMMIF, a program for rapidab-initioshape determination in small-angle scattering. *J Appl Crystallogr* **2009**, 42 (2), 342-346.
108. Bernado, P.; Mylonas, E.; Petoukhov, M. V.; Blackledge, M.; Svergun, D. I., Structural characterization of flexible proteins using small-angle X-ray scattering. *Journal of the American Chemical Society* **2007**, 129 (17), 5656-5664.
109. Petoukhov, M. V.; Svergun, D. I., Global rigid body modeling of macromolecular complexes against small-angle scattering data. *Biophys J* **2005**, 89 (2), 1237-50.

110. Svergun, D. I.; Petoukhov, M. V.; Koch, M. H. J., Determination of domain structure of proteins from X-ray solution scattering. *Biophys J* **2001**, 80 (6), 2946-2953.
111. Svergun, D. I., Restoring low resolution structure of biological macromolecules from solution scattering using simulated annealing. *Biophys J* **1999**, 76 (6), 2879-2886.
112. Svergun, D. I., Restoring low resolution structure of biological macromolecules from solution scattering using simulated annealing (vol 76, pg 2879, 1999). *Biophysical Journal* **1999**, 77 (5), 2896-2896.
113. Svergun, D. I.; Richard, S.; Koch, M. H. J.; Sayers, Z.; Kuprin, S.; Zaccai, G., Protein hydration in solution: Experimental observation by x-ray and neutron scattering. *P Natl Acad Sci USA* **1998**, 95 (5), 2267-2272.
114. Svergun, D.; Barberato, C.; Koch, M. H. J., CRY SOL - A program to evaluate x-ray solution scattering of biological macromolecules from atomic coordinates. *J Appl Crystallogr* **1995**, 28, 768-773.
115. Svergun, D. I., Determination of the Regularization Parameter in Indirect-Transform Methods Using Perceptual Criteria. *J Appl Crystallogr* **1992**, 25, 495-503.
116. Svergun, D. I.; Semenyuk, A. V., Solution of Integral-Equations of the Convolution Type in the Processing of Data on Small-Angle Experiment. *Kristallografiya* **1987**, 32 (6), 1365-1372.
117. Svergun, D. I.; Semeniuk, A. V., A General-Method of the Processing of Small-Angle Scattering Data. *Dokl Akad Nauk Sssr+* **1987**, 297 (6), 1373-1377.
118. Guinier, A., Fournet, G., *Small-Angle Scattering of X-Rays*. John Wiley and Sons: New York, 1955.
119. Hollingsworth, J. V.; Richard, A. J.; Vicente, M. G. H.; Russo, P. S., Characterization of the Self-Assembly of meso-Tetra(4-sulfonatophenyl)porphyrin (H2TPPS4-) in Aqueous Solutions. *Biomacromolecules* **2012**, 13 (1), 60-72.
120. Mircea Anitas, E., Small-Angle Scattering from Weakly Correlated Nanoscale Mass Fractal Aggregates. *Nanomaterials-Basel* **2019**, 9 (4), 648.
121. Beaucage, G., Approximations leading to a unified exponential power-law approach to small-angle scattering. *J Appl Crystallogr* **1995**, 28, 717-728.
122. Hammouda, B. In *Probing Nanoscale Structures- the SANS Toolbox*, 2008.
123. Hendrickson, W., *Analysis of Protein Structure from Diffraction Measurement at Multiple Wavelengths*. 1985; Vol. 21.
124. Rossmann, M. G.; Blow, D. M., The detection of sub-units within the crystallographic asymmetric unit. *Acta Crystallographica* **1962**, 15 (1), 24-31.

125. Perutz, M., Isomorphous replacement and phase determination in non-centrosymmetric space groups. *Acta Crystallographica* **1956**, 9 (11), 867-873.
126. Hendrickson, W. A.; Teeter, M. M., Structure of the Hydrophobic Protein Crambin Determined Directly from the Anomalous Scattering of Sulfur. *Nature* **1981**, 290 (5802), 107-113.
127. Dodson, E., Is it jolly SAD? *Acta Crystallographica Section D* **2003**, 59 (11), 1958-1965.
128. Stribeck, N., *X-ray scattering of polymers*. Springer: Berlin ; New York, 2007; p xx, 238 p.
129. Svergun, D. I.; Koch, M. H. J., Small-angle scattering studies of biological macromolecules in solution. *Rep Prog Phys* **2003**, 66 (10), 1735-1782.
130. Franke, D.; Svergun, D. I., DAMMIF, a program for rapid ab-initio shape determination in small-angle scattering. *Journal of Applied Crystallography* **2009**, 42, 342-346.
131. Kirkpatrick, S.; Gelatt, C. D.; Vecchi, M. P., Optimization by Simulated Annealing. *Science* **1983**, 220 (4598), 671-680.
132. Cockcroft, J.; Jacques, S., *Advanced Certificate in Powder Diffraction*. Birkbeck College: London, 2000.
133. Zhao, J. K.; Gao, C. Y.; Liu, D., The extended Q-range small-angle neutron scattering diffractometer at the SNS. *J Appl Crystallogr* **2010**, 43, 1068-1077.
134. Zhang, F.; Ilavsky, J.; Long, G. G.; Quintana, J. P. G.; Allen, A. J.; Jemian, P. R., Glassy Carbon as an Absolute Intensity Calibration Standard for Small-Angle Scattering. *Metallurgical and Materials Transactions a-Physical Metallurgy and Materials Science* **2010**, 41a (5), 1151-1158.
135. Binnig, G.; Quate, C. F.; Gerber, C., Atomic Force Microscope. *Phys Rev Lett* **1986**, 56 (9), 930-933.
136. Binnig, G.; Rohrer, H., Scanning Tunneling Microscopy. *Helv Phys Acta* **1982**, 55 (6), 726-735.
137. Takai, S.; Richards, W. C., Cerato-ulmin, a Wilting Toxin of *Ceratocystis ulmi*: Isolation and some Properties of Cerato-ulmin from the Culture of *C. ulmi*. *Journal of Phytopathology* **1978**, 91 (2), 129-146.
138. Stevenson, K. J.; Slater, J. A.; Takai, S., Cerato-ulmin—a wilting toxin of Dutch elm disease fungus. *Phytochemistry* **1979**, 18 (2), 235-238.

139. Fischer, H.; Polikarpov, I.; Craievich, A. F., Average protein density is a molecular-weight-dependent function. *Protein Sci* **2004**, *13* (10), 2825-2828.
140. Volkov, V. V.; Svergun, D. I., Uniqueness of ab initio shape determination in small-angle scattering. *J Appl Crystallogr* **2003**, *36*, 860-864.
141. Livsey, I., Neutron-Scattering from Concentric Cylinders - Intraparticle Interference Function and Radius of Gyration. *Journal of the Chemical Society-Faraday Transactions II* **1987**, *83*, 1445-1452.
142. Xu, J. H.; Li, S. W.; Chen, G. G.; Luo, G. S., Formation of monodisperse microbubbles in a microfluidic device. *Aiche J* **2006**, *52* (6), 2254-2259.
143. Jeong, H. H.; Chen, Z.; Yadavali, S.; Xu, J. H.; Issadore, D.; Lee, D., Large-scale production of compound bubbles using parallelized microfluidics for efficient extraction of metal ions. *Lab Chip* **2019**, *19* (4), 665-673.
144. Kothandaraman, A.; Harker, A.; Ventikos, Y.; Edirisinghe, M., Novel Preparation of Monodisperse Microbubbles by Integrating Oscillating Electric Fields with Microfluidics. *Micromachines-Basel* **2018**, *9* (10).
145. Chen, H. S.; Li, J.; Zhou, W. Z.; Pelan, E. G.; Stoyanov, S. D.; Arnaudov, L. N.; Stone, H. A., Sonication-Microfluidics for Fabrication of Nanoparticle-Stabilized Microbubbles. *Langmuir* **2014**, *30* (15), 4262-4266.
146. Xu, Q. Y.; Nakajima, M.; Ichikawa, S.; Nakamura, N.; Shiina, T., A comparative study of microbubble generation by mechanical agitation and sonication. *Innovative Food Science & Emerging Technologies* **2008**, *9* (4), 489-494.
147. Wu, C. D.; Nasset, K.; Masliyah, J.; Xu, Z. H., Generation and characterization of submicron size bubbles. *Adv Colloid Interfac* **2012**, *179*, 123-132.
148. Loewen, M. R.; ODor, M. A.; Skafel, M. G., Bubbles entrained by mechanically generated breaking waves. *J Geophys Res-Oceans* **1996**, *101* (C9), 20759-20769.
149. Riesz, P.; Berdahl, D.; Christman, C. L., Free-Radical Generation by Ultrasound in Aqueous and Nonaqueous Solutions. *Environ Health Persp* **1985**, *64*, 233-252.
150. Cavalieri, F.; Ashokkumar, M.; Grieser, F.; Caruso, F., Ultrasonic synthesis of stable, functional lysozyme microbubbles. *Langmuir* **2008**, *24* (18), 10078-10083.
151. Grinstaff, M. W.; Suslick, K. S., Air-Filled Proteinaceous Microbubbles - Synthesis of an Echo-Contrast Agent. *P Natl Acad Sci USA* **1991**, *88* (17), 7708-7710.
152. Ingram, D.; Wallace, R.; Robinson, A.; Bryden, I. In *The design and commissioning of the first, circular, combined current and wave test basin*, OCEANS 2014 - TAIPEI, 7-10 April 2014; 2014; pp 1-7.

153. Yue, D. Marine Hydrodynamics (13.021). <https://ocw.mit.edu>.
154. Goldacre, R. J., Surface Films on Natural Bodies of Water. *J Anim Ecol* **1949**, *18* (1), 36-39.
155. Tegowski, J., A laboratory study of breaking waves. *Oceanologia* **2004**, *46* (3), 365-382.
156. Wu, Y. C., Plunger-Type Wavemaker Theory. *Journal of Hydraulic Research* **1988**, *26* (4), 483-491.
157. Wu, Y. C., Waves Generated by a Plunger-Type Wave-Maker. *Journal of Hydraulic Research* **1991**, *29* (6), 851-860.
158. Lee, K. M.; Wilson, P. S.; Wochner, M. S., Attenuation of standing waves in a large water tank using arrays of large tethered encapsulated bubbles. *J Acoust Soc Am* **2014**, *135* (4), 1700-1708.
159. Feng, Z. C., Transition to traveling waves from standing waves in a rectangular container subjected to horizontal excitations. *Phys Rev Lett* **1997**, *79* (3), 415-418.
160. Ciliberto, S.; Gollub, J. P., Chaotic Mode Competition in Parametrically Forced Surface-Waves. *J Fluid Mech* **1985**, *158* (Sep), 381-398.
161. Huang, C. J.; Zhang, E. C.; Lee, J. F., Numerical simulation of nonlinear viscous wavefields generated by piston-type wavemaker. *Journal of Engineering Mechanics-Asce* **1998**, *124* (10), 1110-1120.
162. Chwang, A. T.; Li, W., A piston-type porous wavemaker theory. *Journal of Engineering Mathematics* **1983**, *17* (4), 301-313.
163. Tian, M.; Kadri, U., Wavemaker theories for acoustic-gravity waves over a finite depth. *Journal of Engineering Mathematics* **2018**, *108* (1), 25-35.
164. Brown, D.; Cox, A. J., Innovative Uses of Video Analysis. *The Physics Teacher* **2009**, *47* (3), 145-150.
165. Nirody, J. A.; Sun, Y.-R.; Lo, C.-J., The biophysicist's guide to the bacterial flagellar motor. *Advances in Physics: X* **2017**, *2* (2), 324-343.
166. Ashkin, A., Acceleration and Trapping of Particles by Radiation Pressure. *Phys Rev Lett* **1970**, *24* (4), 156-&.
167. Ashkin, A., Optical trapping and manipulation of neutral particles using lasers. *P Natl Acad Sci USA* **1997**, *94* (10), 4853-4860.
168. Degennes, P. G., Reptation of a Polymer Chain in Presence of Fixed Obstacles. *J Chem Phys* **1971**, *55* (2), 572-+.

